令和 4 年度　博士論文

Self-assembled structure and magnetism of lanthanoid multinuclear complexes with lacunary polyoxometalate ligands

（欠損型ポリオキソメタレート配位子を有するランタノイド多核錯体の自己組織化構造と磁性）

北海道大学大学院環境科学院

WU DONGFANG

2022.8

Catalog

Chapter I

General Introduction

1-1. Crystal engineering

In recent years, the design of new structures for the purpose of crystal engineering has attracted a great deal of interest. Crystal engineering is the design and synthesis of molecular solid-state structures with desirable functional properties based on the understanding and exploitation of intermolecular interactions. The development of the field of crystal engineering can usually be traced back to Schmidt's work in the 1960s, work that was based on keen crystallographic insight. Thus, Schmidt noticed that chlorinated aromatic compounds were often observed to crystallize with molecular stacks at a separation of 4 Å. This observation was subsequently used in a number of early examples of what became known as crystal engineering.[1,2] Molecular crystals have interesting physical and chemical properties that are unrelated to other classes of crystalline substances. These properties are related to, and closely associated with, their internal periodic structures. These internal structures are called crystal structures, and they are of outstanding importance in crystal engineering. Therefore, it is necessary to be able to design specific crystal structures in which molecules are assembled in a particular way. In turn, a specific crystal structure has a specific property that is desired.

Chemical properties lead to changes in the chemical composition of the crystal, which may be reversible or irreversible. Molecular crystals with specific chemical properties (reactivity, isomerism, color change) can be used as sensors, devices, photosensitive materials and for catalytic applications.[3–9] Physical properties (gas inclusion, electrical, magnetic, optical, solubility) are more easily tailored, and most applications are in this category.[10,11] The nonlinear optical response of some organic solids lacking a crystal center of symmetry exceeds that found in currently used inorganic materials. These crystals are used as frequency doublers and waveguides.[12–14] Non-centrosymmetric crystals are also used as ferroelectrics, piezoelectrics, pyroelectrics, and triboluminescent materials.[15–18] Solid form control is important in industries related to dyes, pharmaceuticals and explosives. The importance of obtaining different solid forms (polycrystals, solvates, co-crystals) of a drug molecule can lead to significant commercial benefits. Today, a major application of molecular crystals is in the engineering of open metal-organic framework structures.[3,19] These compounds have been compared to zeolites because they have a framework structure with large internal spaces enclosed. However, in contrast to zeolites, the size of the voids in coordination polymers is very large and the internal surface area is consequently large. As a

result, these materials are able to absorb large amounts of gas.[20] They can also be designed to allow selective absorption of gases from gas mixtures. Such applications are of great use in separation and catalysis.[19,21]

The success of crystal engineering strategies depends on the availability of robust and transferable interactions to glue together the building materials. These intermolecular forces have been systematically reviewed and range in strength from strong ionic interactions (100-350 kJ mol^{-1}) through ion-dipole, dipole-dipole, hydrogen-bonding, anion- and cation... π-interactions, π···π-stacking, to weak van der Waals forces (< 5 kJ mol^{-1}).[22] The strength of the interactions is their most obvious and noteworthy property. Many of the interactions that may be important in crystal stacking have minimum energies between 0.5 and 5 kcal mol^{-1}. These energies are indeed very weak. Thus, the energetic factors that build up crystal stacking are subtle, and the crystal structure is the result of a compromise between the needs of many weak interactions. A second important property of intermolecular interactions is their directionality. This property is of obvious significance in crystal design because the directionality of interactions can be exploited to achieve specific and pre-desired intermolecular orientations. Hydrogen bonding is the most important orientation interaction in molecular crystals. It is the anisotropy of the interactions in the crystal structure that allows one to propose design strategies for crystals of related molecules. A third important general property of intermolecular interactions is their distance dependence. The distance dependence of interactions is related to the events that precede nucleation and crystallization. Strong or even weak hydrogen bonds have an orientation effect on the molecule prior to nucleation and crystallization. Their orientation preferences remain in the final crystal structure, even though the contribution of these electrostatic interactions to the total energy of the crystal is small. In order to organize the topology or connectivity of the molecules in the crystal structure, an interaction should preferably be both strong and directional.[23]

1-1-1. Hydrogen bonding interaction

Since the directional and strength properties of hydrogen bonds determine to varying degrees the structure of ions, molecules and even crystals, the study of hydrogen bonds has a broad perspective and important applications. Other heteroatom interactions such as S···S, halogen···halogen and halogen···O are also directional. Unlike other typical chemical bonds (ionic,

covalent and metallic bonds), the energy of hydrogen bonds spans two orders of magnitude, from several kcal/mol for weaker hydrogen bonds to tens of kcal/mol for stronger hydrogen bonds. The angular properties of hydrogen bonds are also an important feature of the interaction. The orientation of hydrogen bonds is generally in the lone pair region of the acceptor atom. The trend of all hydrogen bonds is toward linearity, which is because the positively charged H atom is most effective as a medium capable of shielding closely approached negative charges when it is located in a straight line connecting the X and Y atoms. Any crystal structure is the result of a compromise between many molecular interactions with different strengths, angular preferences and distance-dependent properties. Usually, the angle of hydrogen bonding is not 180°, and one reason for this bending is that hydrogen atoms are often approached by a second acceptor in an attractive manner. This type of interaction is called bifurcated hydrogen bonding, or three-center interaction.

Hydrogen bonds can be classified according to the following perspectives: (1) linear (two-center), bifurcated (three-center), trifurcated (four-center) or multifurcated (four-center) hydrogen bonds according to their geometric configuration; (2) homonuclear and heteronuclear hydrogen bonds or neutral and ionic hydrogen bonds according to the nature of the proton donor and acceptor; (3) symmetric and asymmetric hydrogen bonds according to the position of the hydrogen atom; (4) the way of existence, *i.e*., whether the proton donor and acceptor belong to the same molecule, is divided into intramolecular and intermolecular hydrogen bonds. Intermolecular hydrogen bonds affect the stacking of molecules in the lattice space, while intramolecular hydrogen bonds play a role in molecular folding and intramolecular ring formation; (5) according to the spectral properties, they are divided into red-shifted and blue-shifted hydrogen bonds; (6) according to the types of proton donors and acceptors, they are divided into conventional and unconventional hydrogen bonds (blue-shifted hydrogen bonds, hydrogen bonds with π-electrons as proton acceptors, charged hydrogen bonds, double hydrogen bonds, and transition metal acceptor hydrogen bonds, *etc*.); (7) Gilli *et al*. classified hydrogen bonds into five categories based on their strength: i) strong hydrogen bonds with negative charges, ii) strong hydrogen bonds with positive charges, iii) strong hydrogen bonds with resonance, iv) moderately strong polarized hydrogen bonds (polarized, induced polarization or σ-coordinated hydrogen bonds), and v) isolated weak hydrogen bonds (isolated or uncharged hydrogen bonds and non-resonant or non-coordinated hydrogen bonds),[24–26] (8) Grabowski studied the X-H···Y system with π and σ electrons as multicenter proton acceptors and classified hydrogen bonds into: i) hydrogen bonds with a single central proton acceptor

(Pauling-type hydrogen bonds, hydrogen bonds where the proton acceptor Y or/and the donor X are non-electronegative atoms, and double hydrogen bonds), 2) hydrogen bonds with a multi-center proton acceptor Y or/and a donor X.[27]

All in all, the energy distribution of hydrogen bonds is wide, and it has flexible and changeable structural types, with saturation and directionality. Hydrogen bonds are widely used design tools in the fields of supramolecular chemistry, molecular recognition and crystal engineering, having an important contribution to the macroscopic properties of crystals. In this thesis, the significant meaning of hydrogen-bond interaction between polyoxometalates and supramolecular cations in assembly structure is elaborated.

1-1-2. π···π interaction

The π-interactions have a long range of action and multiple contact points, and they are relatively non-directional compared to other intermolecular interactions.[28] Currently, π-interaction is considered as any close contact between any π- or delocalized-electron system and a donor atom or another π-system (Figure 1-1). The donor can be in the form of a strong donor atom (*e.g.*, O, N), a weaker donor such as C-H, an anion, or another π-system.[29] These π-systems can be aromatic rings or alkene or alkyne moieties. In general, aromatic systems tend to be planar molecules (also alkene and alkyne moieties) with a large surface-to-volume ratio. Due to their shape, supramolecular space tends to surround the edges of these molecules. Therefore, considering the concept of close stacking, the most reasonable stacking arrangement for these molecules is for the molecules to be stacked on top of each other.[30] Aromatic π···π interactions are known to associate with their nearest neighbors in one of four ways (Figure 1-2): face-to-face (also known sandwich) stacking, offset face-to-face (or parallel displaced) stacking, edge-to-face (or Y-shaped), and point-to-face (or T-shaped). Rare face-to-face stacking facilitates the assembly of graphitic layers.[31] The edge-to-face interaction contributes to the famous herringbone pattern.[32] Offset packing as well as edge-to-face interactions are observed in the sandwich-herringbone patterns, where molecules are packed in pairs.[33] The currently accepted plane separation for face-to-face and offset face-to-face interactions is 3.3-3.8 Å, while for edge-to-face interactions, the center-to-center distance can be up to 5 Å.

Most researchers tend to underestimate the influence of π-interactions in the construction of stacking patterns. Of course, it can be argued that π···π-interactions have little effect on the stacking of molecules in crystals but are simply the result of the forced alignment by stronger interactions. However, one should keep in mind that the crystal structure is often a compromise of many stable and unstable interactions that cannot be separated. In some examples, the extension of an aromatic molecule seems to affect the arrangement of the whole molecule because of increased π···π interactions.[34]

Figure 1-1. Examples of π- π, CH-π and π-cation interaction. Copy right from Wikimedia.

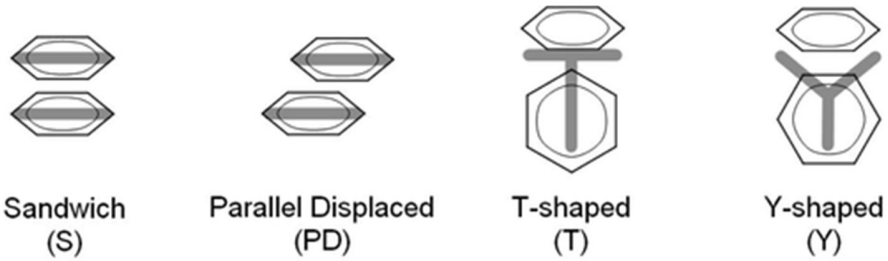

Figure 1-2. Aromatic π···π interactions modes: parallel face-to-face "sandwich" (S), parallel displaced (PD), perpendicular T shaped (T), and perpendicular Y shaped (Y). [35]

1-1-3. Symmetry

In addition, as one of the most important concepts in the crystal structure, symmetry plays a crucial role in constructing structure–property relationships.[36] It is simply defined as the physical or mathematical feature of a system that remains constant under a specific group of transformations. These transformations or symmetry operations, such as translation, inversion, reflection, and rotation, constitute various symmetry groups. In crystallography, there are 32 point groups and 230 space groups describing the macroscopic and microscopic symmetries of crystal structures, respectively. Among the 32 point groups, 11 centrosymmetric classes have spatial-inversion

symmetry, whereas the remaining 21 noncentrosymmetric ones do not. A lack of spatial-inversion symmetry is important for numerous physical systems, particularly for ferroelectrics.[37–40]

Finally, these design of structures in turn can be translated to physical or chemical properties in a solid. For example, molecular rotator, porous materials for use in chemical separations and as highly selective reaction microenvironments, polar materials for non-linear optical applications including second harmonic generation, materials with tailored magnetic or photophysical (*e.g.* luminescent) properties that may be useful in electronics applications or as molecular sensors, ferroelectric materials, *etc.*[15–18,41–45]

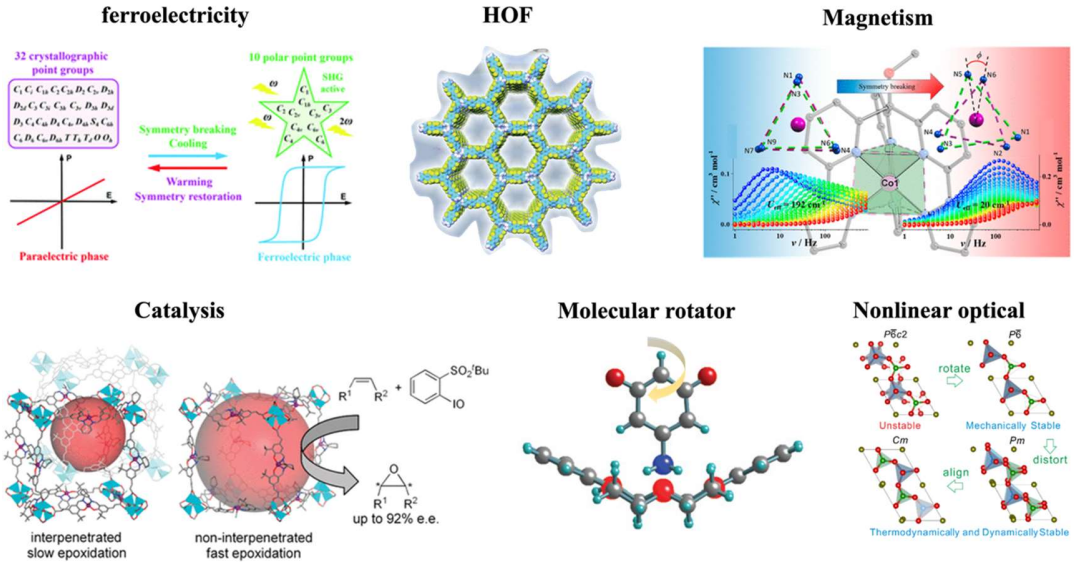

Figure 1-3. The application of crystal engineering.[17,18,40–43]

1-2. Polyoxometalates

Polyoxometalates (POMs) are inorganic metal oxide cluster compounds with general formula of $\{MO_x\}_n$, mainly consisting of early-transition metal atoms (vanadium, molybdenum, tungsten, niobium, *etc.*) that are connected by shared oxygen atoms to form 3-dimensional frameworks. They can be divided into two generic families: (1) the isopolyoxometalates (IPOMs), with the general formula of $[M_mO_o]^{-p}$ made of the d^0 metal cations and oxide anions or addenda metals and oxygen. Addenda atoms can alter their coordination number with oxygen from 4 to 6 by polymerization in acidic solution and have a high positive charge; (2) the heteropolyoxometalates (HPOMs), which contain at least one p- or d-block element as heteroatom (P, As, Si, etc.) And

their general formula is $[X_xM_mO_o]^{-q}$. M is the metal cation and X could be Si(V), P(IV), B(III), *etc*. Hetero-polyanions are built by condensation of MO_x (x = 4–7) polyhedral around central heteroatoms by acidification of solution.[46]

The first example of heteropolyoxometalates is ammonium phosphomolybdate (yellow), $(NH_4)_3PMo_{12}O_{40}{\cdot}nH_2O$, discovered in 1826 by J. Berzelius, which was synthesized from molybdate and phosphate.[47] And then, Marignac first synthesized heteropolytungstate and determined its composition in 1864.[48] Furthermore, C. Scheibler synthesized phosphotungstic acid in 1872, the composition of which is confirmed by W. Gibbs and M. Sprenger at 1909-1910. In 1929, Pauling reported his three-dimensional model on the structures of 12-POMs. His models were written as $H_4\{SiO_4W_{12}O_{18}(OH)_{36}\}$ and $H_3\{PO_4W_{12}O_{18}(OH)_{36}\}$.[49] Pauling proposed that the structure of 12-tungsto anions were based on a central PO_4 or SiO_4 tetrahedron surrounded by WO_6 octahedra, which is exactly same as the model proposed by Keggin in 1933, which is confirmed by the X-ray crystallography in 1974.[50] Today, POMs constitute an immense class of polynuclear metal-oxygen clusters usually formed by Mo, W or V and mixtures of these elements.[51,52] The classical structures include Keggin, Dawson, Anderson, Allman-Waugh, Dexter-Silverton, Lindqvist, as shown in the Figure 1-4. The most common is the Keggin structure.

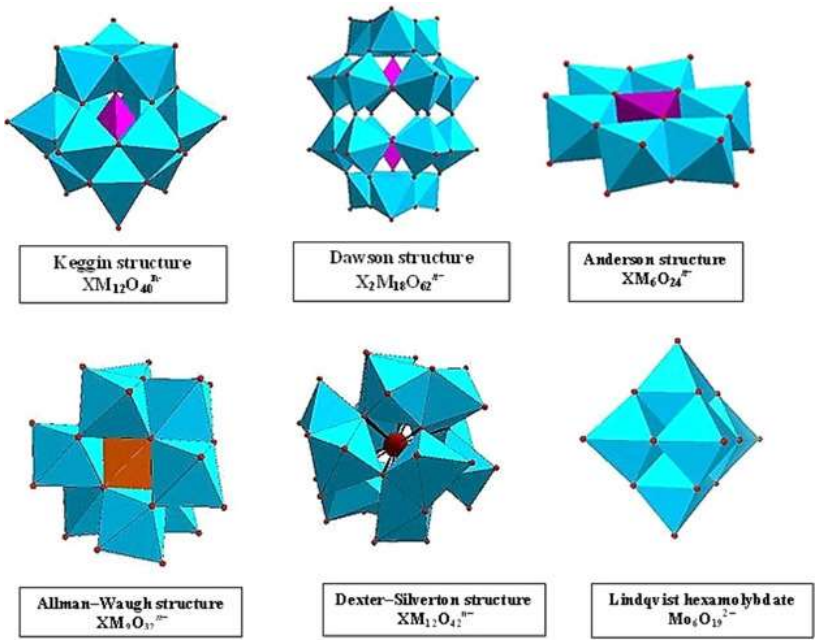

Figure 1-4. The structure of classical POMs.[53]

In the late 1960s, the fascinating structural chemistry and multiple potential applications of polyoxometallates attracted an increasing number of people to study them from different perspectives. Especially after the 1980s, basic research on polyoxometallates chemistry has shown unprecedented activity and applied research has been highly emphasized. With the development of analytical techniques and instruments, novel structures (multidimensional, porous, cavernous, sandwich, nanoclusters, *etc*.) have emerged. The synthetic chemistry of polyoxometallates has entered the stage of molecular tailoring and assembly; from the synthesis and study of stable oxidation state compounds to the study of sub-stable and variable valence compounds and supramolecular compounds; from the public study of isolated structures to the study of modification and expansion of structures with them as basic units. In terms of applications, in addition to traditional catalytic research, we have now entered the fields of pharmaceutical science, materials science, analytical chemistry, and biochemistry, and many of our research results have received much attention (Figure 1-3).[3,54–62] However, as mentioned above, all these applications depend on the structural characteristics of POMs-based crystalline architecture.

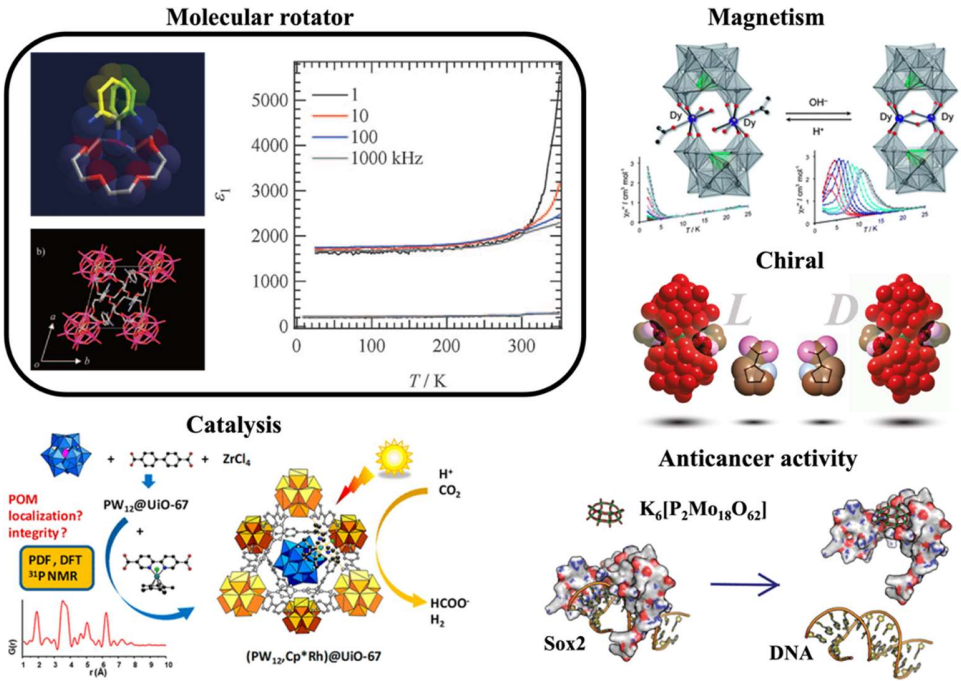

Figure 1-5. The application of POMs.[3,56,60–62]

1-2-1. Structural isomers of Keggin-type POMs

The original Keggin structure refers to $\{M_{12}O_{36}\}$ topology which upon encapsulation of a single tetrahedral guest unit collapses to the T_d symmetry point group, giving the Keggin-type heteropolyoxometalates $\{XM_{12}O_{40}\}$ (X = P, Si, Ge, As…, M = Mo, W).[63] The structure can virtually further isomerize by stepwise 60° rotation of each of the four triads, leading to *α*-, *β*-, *γ*-, *δ*-, *ε*-Keggin isomers with symmetry of T_d, C_{3v}, C_{2v}, C_{3v} and T_d.[64] Removing $\{MO_6\}$ octahedrons results in the so-called lacunary POMs that is unsaturated, such as $\{XW_{11}\}$(monolacunary series), $\{XW_{10}\}$(dilacunary series), $\{XW_9\}$(trilacunary series), and so on. Among various POMs, lacunary POMs have received significant attention due to the fact that the properties in this material can be easily tuned by changing their composition and structures. The study of lacunary POMs is a very important research area in polyoxometallates chemistry. While saturated POMs tend to form isolated clusters, lacunary POMs are easy to modify and expand into high-dimensional structures and are an important tool for the derivatization of POMs. In addition, lacunary POMs are easy of forming covalent or iono-covalent bonding interaction, hydrogen-bond interaction and electrostatic interaction with inorganic or organic groups.[65–72] Among them, the use of protonated organic ammonium cations results in an inverse cation templating effect, which has been used to assemble new POM clusters, hybrids, and framework materials.[73–76] In this thesis, some simple ammonium cations with distinct symmetry are introduced to induce POM assembly.

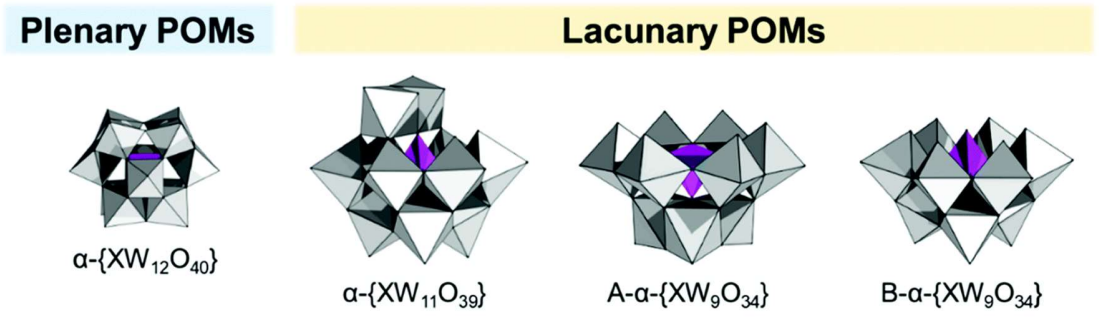

Figure 1-6. Polyhedral representation of the saturated *α*-Keggin POMs and the related "unsaturated" POMs (lacunary POMs).[77]

1-2-2. Sandwich structures of Lacunary Keggin POMs

In contrast to the corresponding saturated POMs, the removal of one or more metal octahedra $\{MO_6\}$ from the saturated POMs structure leads to negative charge-defining domains within the lacunary POMs, resulting in a high nucleophilicity of the lacunary POMs (which can be viewed as a multi-dentate ligand), which can easily coordinate with metal, organometallic and organo-quasimetallic groups to form organometallic complexes and heteropolyoxometalates that may have mono-, bi- or even multi-functional properties. Transition metal ions, lanthanoid ions and main group elements coordinated to the lacunary POMs can form substituted saturated structures, sandwich structures, cluster structures and a series of compounds.[78,79]

1-2-2-1. Sandwich structures of monolacunary Keggin POMs($\{XW_{11}\}$)

There are two basic types of monolacunary Keggin POMs structures, one is a 1:11 series structure $[XM_{11}O_{39}]^{n-}$ formed by the saturated Keggin structure losing one MO_6 octahedron. And the other is a 2:17 series of structure $[X_2M_{17}O_{39}]^{n-}$, which is formed by the loss of a MO_6 octahedra from a 2:18 Dawson structure.

For the 1:11 series structure $[XM_{11}O_{39}]^{n-}$, when one of the MO groups is lost, a vacant M position appears and acts as a pentadentate ligand, which can be coordinated with transition metal ions, lanthanide ions and main group elements to form various heteropolyoxometalates. When the metal ion Z is a Ln atom with a larger diameter, it forms a $Z(XM_{11})_2$ compound, which is a sandwich type structure of monolacunary heteropolyoxometalates. At this point, $Z : XM_{11} = 1 : 2$, and the polyanion plays the role of a tetradentate ligand. Lanthanoid derivatives were the most studied in the early period. Peacock and Weakley first investigated the interaction between $[\alpha\text{-}SiM_{11}O_{39}]^{8-}$ and lanthanoid ions in 1971, and also reported 1 : 1 and 1 : 2 lanthanoid derivatives of $[\alpha\text{-}SiM_{11}O_{39}]^{8-}$.[80,81] And in 2000, Pope and co-workers first reported and characterized the structures of 1:1 $[Ln(\alpha\text{-}SiM_{11}O_{39})(H_2O)_3]^{5-}$ ($Ln = La^{III}, Ce^{III}$) polymers in one-dimensional chains. Subsequently, in 2003, Mialane and his co-workers synthesized $[Ln_n(\alpha\text{-}SiM_{11}O_{39})]^{8-}$, a lanthanoid derivative of $[\alpha\text{-}SiM_{11}O_{39}]^{8-}$ ($Ln = Yb^{III}, Nd^{III}, Eu^{III}$ and Gd^{III}), using a different synthetic method than Pope, and studied and classified its solid structure type (Figure 1-7).[82] In 2004, Mialane also reported the dimeric $[(SiW_{11}O_{39}Ln)_2(\mu\text{-}CH_3COO)_2]^{12-}$ (Ln = Gd, Yb).[83]

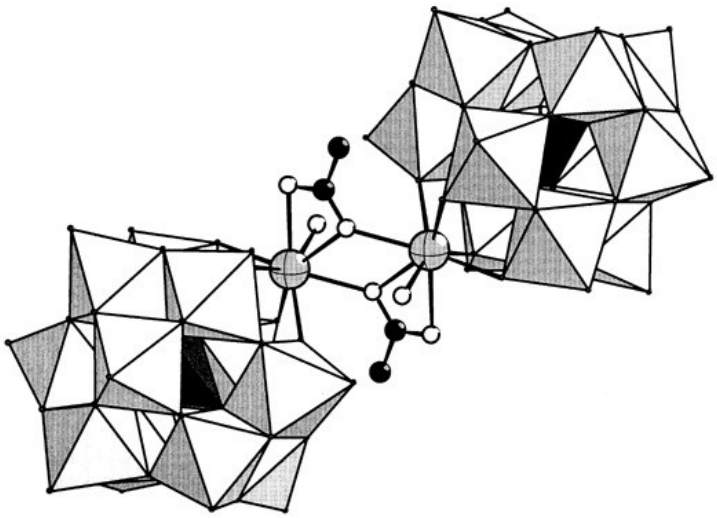

Figure 1-7. Polyhedral representation of complex $[\{Yb(\alpha\text{-}SiW_{11}O_{39})(H_2O)\}_2(\mu\text{-}CH_3COO)_2]^{12-}$.[82]

1-2-2-2. Sandwich structures of dilacunary Keggin POMs({XW_{10}})

The dilacunary structure is usually the $[XM_{10}O_{36}]^{n-}$ series structure obtained by losing two MO_6 octahedra in the saturated Keggin structure. It is metastable, which is not only easy to isomerize in structure, but also difficult to synthesize with low yield. In 1996, Pope's group reported a sandwich structure $[(PhSnOH_2)_2(\gamma\text{-}SiW_{10}O_{36})_2]^{10-}$ based on a dilacunary heteropolyoxometalates γ-SiW_{10}.[84] The same sandwich structure of γ-SiW_{10} was reported by Kortz's group and liu's group in 2006.[85]

1-2-2-3. Sandwich structures of trilacunary Keggin POMs({XW_9})

Another rotational isomer is the $\{XW_9O_{34}\}$ Keggin structure with C_{3v} symmetry obtained by by removal of W_3O_6 trimers from a saturated Keggin $XW_{12}O_{40}$ unit. Depending on the encapsulated heterogroup, whether it is a tetrahedral $\{XO_4\}$ or trigonal pyramidal $\{XO_3\}$ group, two general formula $\{XW_9O_{34}\}$ and $\{XW_9O_{33}\}$ are possible.[86,87] There are four kinds of isomers (α-A, α-B and β-A, β-B) in this series of compounds. In α-Keggin, there are two inequivalent triad positions which can be virtually removed leading to the formation of A-α and B-α trilacunary Keggin POMs with symmetry of C_{3v}. The A-α isomer is the most commonly observed with the $\{XO_4\}$ heterogroups where $X = P^V$, Si^{IV} and Ge^{IV}, while the B-α isomer is common for the $\{XO_3\}$ groups with a lone pair of electrons such as $X = As^{III}$, Sb^{III} and Bi^{III} which contain a lobe of electrons pointing towards the outer of the lacuna. Since the internal oxygen atoms are exposed, these

exposed oxygen atoms become active coordination sites, so this type of compound has strong coordination activity.

The trilacunary keggin POMs structure is most likely to form a sandwich compound by adding metal ions between the two trilacunary keggin POMs units. Knoth reported the first lanthanide compound based on trilacunary Keggin heteropolyoxometalates in 1986.[88] This compound has a sandwich structure consisting of two $[PW_9O_{34}]^{9-}$ (PW_9) units connected by a belt of three lanthanide atoms. The belt contains three oxygen atoms, alternating with three lanthanide atoms (Figure 1-8). Since then, a large number of such Knoth-type structures have been reported one after another.[89–92] Hill synthesized the first examples of sandwich-type POMs that encapsulate CO_3^{2-} in the center of $[(A\text{-}PW_9O_{34})_2(H_2OY)_3CO_3]^{11-}$.[93] Divalent metal derivatives of the A-type sandwich complexes are unstable, converting to complexes containing B-$[XW_9O_{34}]^{n-}$.[94,95] However, the A-type sandwich complexes with trivalent lanthanides are stable toward A to B isomerization and also allow stabilization of the encapsulated carbonate.[96]

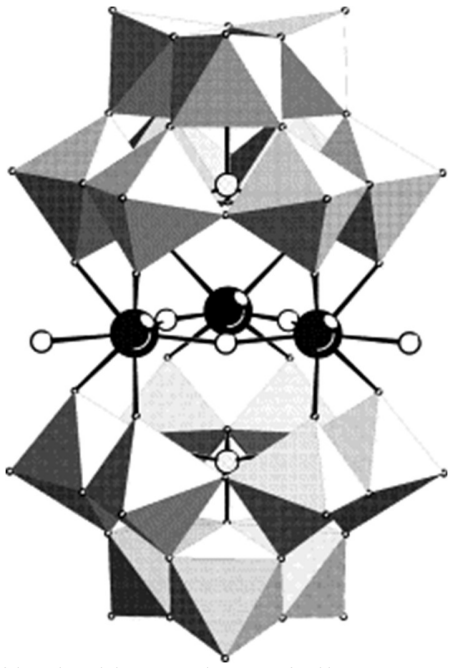

Figure 1-8. Proposed structure of lanthanide complexes of trilacunary $Na_8[HPW_9O_{34}]$ polyoxometalate.[88]

1-3. Single molecular magnets

The design of single-molecule magnets (SMMs) based on the phenomenon of blocking of magnetization at low temperatures has become a hot area of research due to the potential

applications of such compounds in new storage and information-processing technologies. Single molecule magnets refers to the compound retains magnetisation in a single molecule, which can function as nanomagnets.[97] As shown in Figure 1-9, the single-molecule magnet is in a bistable state without being magnetized, in which molecular magnetization possessing same population orients in the opposite direction. The positive and negative *Ms* quantum levels are separated by a thermodynamic activation barrier (U) corresponding to $|D|S^2$, where D (<0) is a zero-field splitting parameter and S is a spin quantum number.[98] The vector sum of the magnetization is zero. After an external magnetic field is applied, the above-mentioned bistable balance is broken, and the vector sum of its magnetization is no longer zero. Then the external magnetic field is removed, and an energy barrier will be generated when the molecular magnetization vector is reoriented. When the temperature falls even below the flip energy barrier, the flip rate slows down, resulting in a slow magnetic relaxation behavior of the magnetization, which is typical of single-molecule magnet behavior.[99] The lowest temperature at which the hysteresis loop can be observed is generally considered to be the blocking temperature (T_B) of single-molecule magnets.[100] In nearly three decades of research on single-molecule magnets, scientists have been working to increase their blocking temperature and flip energy barrier to facilitate their practical applications. The blocking temperature is determined by the flip energy barrier, which is closely related to the type, coordination configuration, uniaxial magnetic anisotropy of the central metal ion, and its axial and equatorial crystal field environment. As mentioned before, recognizing geometry and functionality at the molecular level has relevant implications in the design of molecular structures.

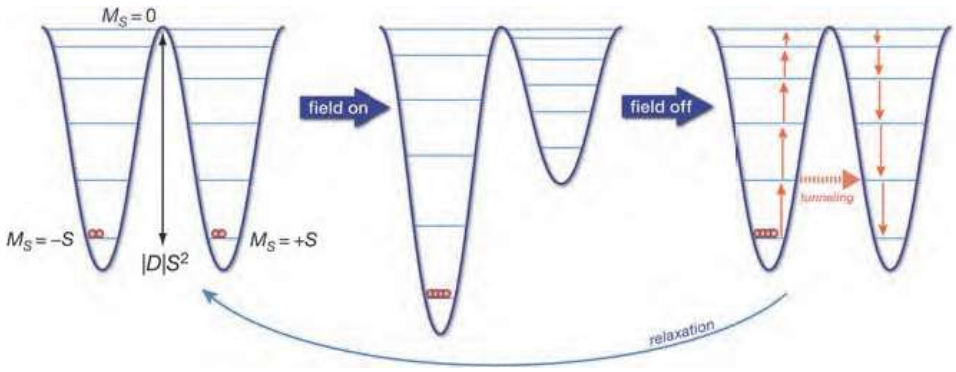

Figure 1-9. The magnetic bistability of SMMs.

In 1993, the discovery of single-molecule magnetism (SMM) in the Mn_{12} complex opened the perspectives for SMM in information storage, molecular spintronics and quantum computing.[101] Then in 2003, the first lanthanide single-molecule magnet $[TbPc_2]^-$ entered the field with a high relaxation energy (U_{eff}) of 331 K that far exceeds the U_{eff} of 3d-SMMs, which has inspired more and more interest of scientists in Ln-SMMs (Figure 1-10).[102] In 2008, through theoretical studies on two Mn_6 compounds with similar compositions and structures, Ruiz E et al. revealed that the magnitude of the anisotropy barrier is mainly determined by the strength of the spin–orbit coupling and cannot be engineered by independently optimizing D and S, since the intrinsic relationship between these two parameters prevents this possibility.[103] Subsequently, lanthanoid with larger ground state spins and stronger magnetic anisotropy than transition metals attract more interest of scientists studying single-molecule magnets. What's more, more and more investigations indicate that the performance of Ln-SMMs is better than 3d-SMMs.[104,105]

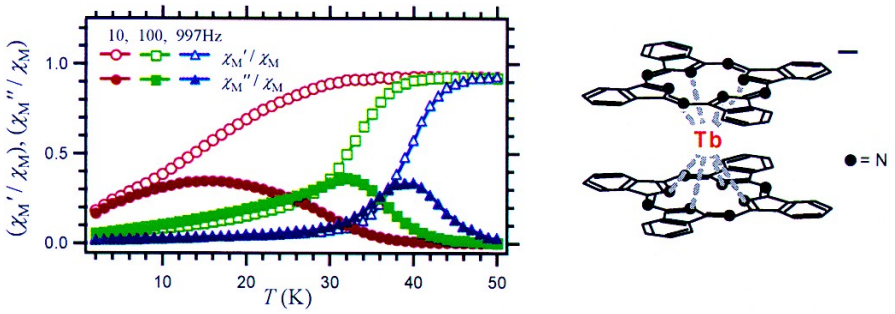

Figure 1-10. The dynamic magnetic properties and molecular structure of double-decker phthalocyanine complexes $[TbPc_2]^-$ TBA^+.[102]

In 2006, the first example of multinuclear Ln-SMM $[Dy_3(\mu_3\text{-}OH)_2L_3Cl(H_2O)_5]Cl_3$ (Dy_3, L = ortho-vanillin) with approximate C_{3h} symmetry, was reported by Powell.[106] The compounds show the unusual coexistence of slow relaxation of the magnetization and an almost diamagnetic ground state (Figure 1-11). Then, it was proved that the origin of the nonmagnetic ground state in dysprosium(III) triangles is the toroidal arrangement of magnetic moments on the dysprosium sites. This is the first time that an almost perfect toroidal magnetic moment has been detected in a molecular magnet. The compound may become a molecularly based multiferroic material.[107] This breakthrough has inspired research into the special magnetic behavior of Ln_3 triangles and enthusiasm for research on multi-core lanthanoid single-molecule magnets.[108–111]

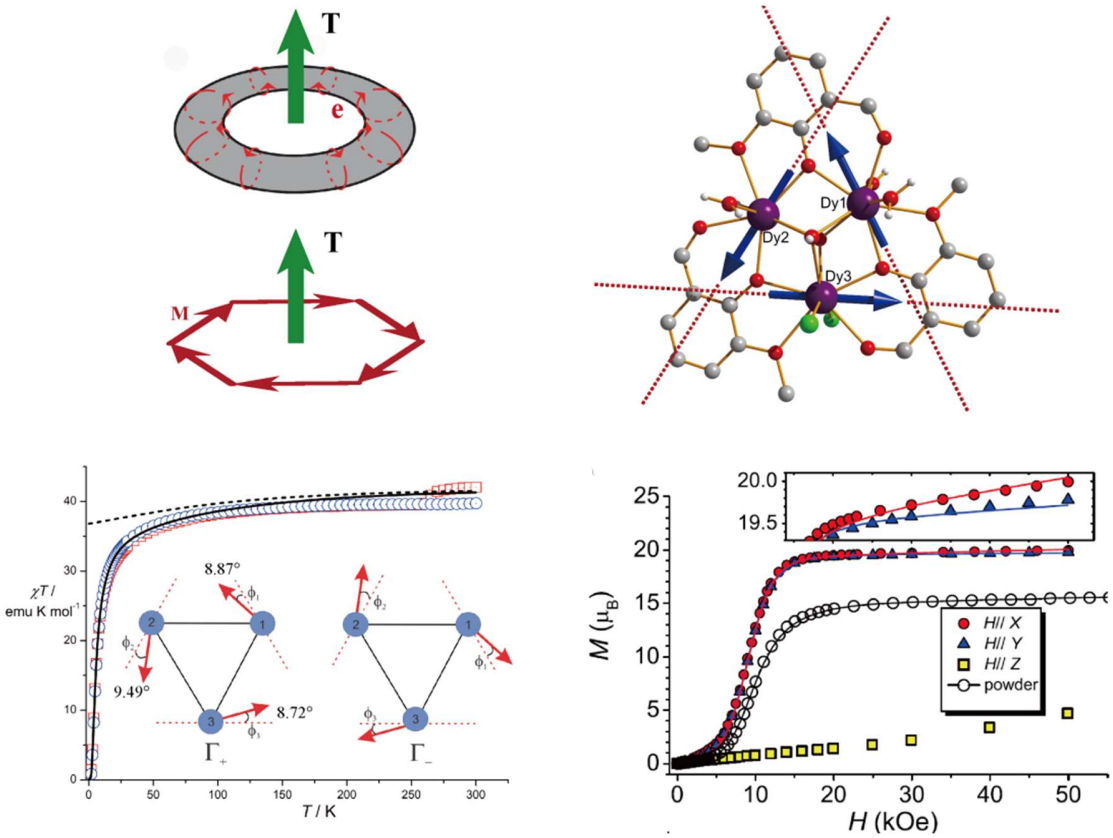

Figure 1-11. (Top) Two examples of a toroidal moment and the structure of Dy_3 with main anisotropy axes (dashed lines) and local magnetizations (arrows) in the ground state. (Bottom) The two components of the ground Kramers doublet andthe static magnetic properties of Dy_3.[106,112]

In 2008, the first example of a POM ($[ErW_{10}O_{36}]^{9-}$) exhibiting SMM behavior with U_{eff} of 55.2 K was reported by M. A. AlDamen. Lanthanides are encapsulated by polyoxometalates (POMs) with coordination geometries similar to those of bis(phthalocyaninato)lanthanide compounds (Figure 1-12). Compared with to organic ligands for Ln-SMMs, lacunary POMs are excellent multidentate O-donor ligands for trivalent Ln ions, and POM ligands can minimize unwanted intermolecular interactions by the three-dimensionally bulky structures and provide coordination geometries and crystal-fields (CFs) that are unavailable with organic ligands.[113]

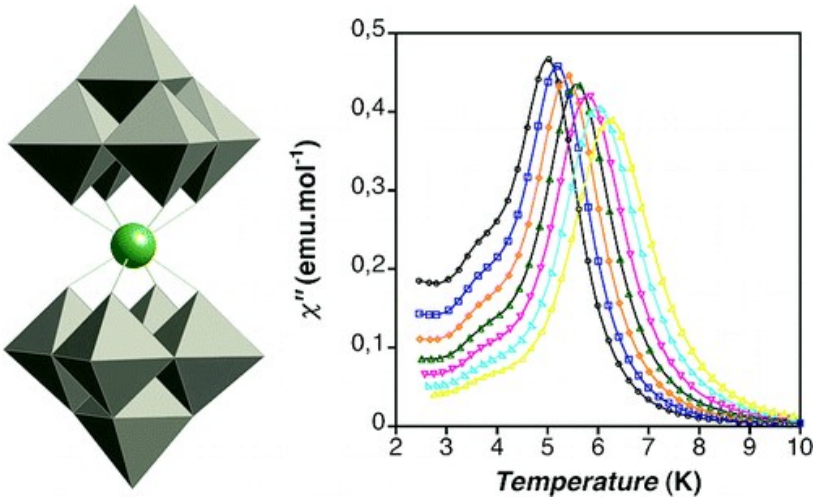

Figure 1-12. The molecular structure (left) and dynamic magnetic properties (right) of the sodium salt of the $[ErW_{10}O_{36}]^{9-}$ polyanion.[113]

In 2016, a series of Ln-based sandwich-type POMs, $Na_{11}[\{Ln(OH)_2\}_3CO_3(PW_9O_{34})_2]$ (Ln = Y, Tb, Dy, Ho, and Er), with CO_3^{2-} bridged Ln_3-triangle sandwiched by two lacunary POMs, were revealed by Giansiracusa *et al* and the SMMs behavior of Ln ions, Dy (III) and Er (III), was indicated by AC magnetic susceptibility measurements (Figure 1-13).[114] It isn't realized that the ground state was described by a noncollinear collective magnetic configuration, such as a nonmagnetic KD corresponding to a toroidal moment, as found in $[Dy_3(\mu_3\text{-}OH)_2L_3Cl(H_2O)_5]Cl_3$ (Dy_3, L = ortho-vanillin) mention before.[106]

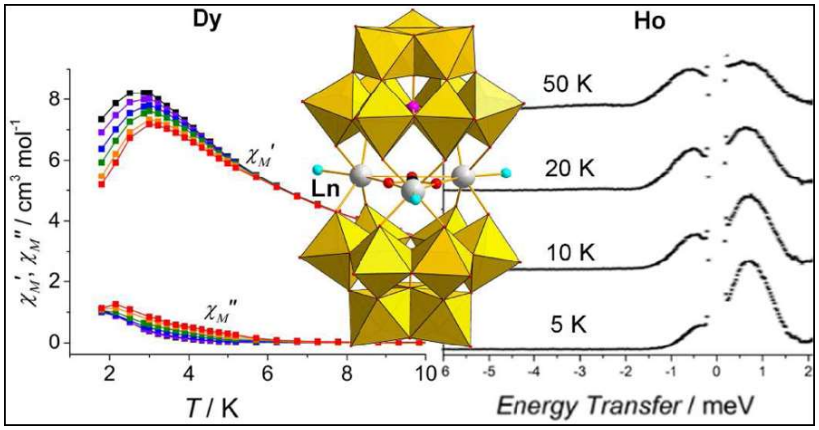

Figure 1-13. The structure, Variable-temperature INS spectra and magnetic properties of $[\{Ln(OH_2)\}_3CO_3(PW_9O_{34})_2]$.[114]

1-4. Research purpose

1) POMs possess high reactive oxygen surface, which enable them of forming covalent or iono-covalent bonding interaction, hydrogen-bond interaction, and electrostatic interaction with inorganic or organic groups. Meanwhile, most of POMs have highly symmetric structure, combined with the directional and flexible hydrogen-bond interaction, which promote them to construct versatile organic-inorganic hybrid materials.
2) On the other hand, electrostatics is the dominant POM–cation interaction, particularly when both species are in close contact. Therefore, the synthetic combination of lacunary POMs with highly basic oxygen atoms and large oxyphilic lanthanoid cations is a powerful strategy to form polynuclear compounds. The μ_3-carbonate-bridged triangles of trivalent lanthanoid ions sandwiched between two lacunary Keggin POMs with C_3 symmetry give a nice platform for investigating peculiar magnetic behaviors such as single molecule magnetic behaviors, toroidal magnetic moments, and spin frustration arising from lanthanoid triangles. In addition, the advantage of the sandwich POMs is that the unwanted intermolecular magnetic interaction between POMs is so weak due to large size of the molecules which are separated by large numbers of counter cations.

Therefore, in this thesis, α-lacunary Keggin POMs [PW_9O_{34}] and [PW_9O_{31}] with many reactive oxygen sites and distinct symmetry are exploited. Meanwhile, as counter cations, a) simple ammonium cations, methylammonium, dimethylammonium, trimethylammonium, tetramethylammonium, diprotonated 1,4-Diazabicyclo[2.2.2]octane cations, b) supramolecular cations constructed of crown-ether and Na^+ ions, [(Na)(B[18]crown-6)], were introduced to regulate the architecture of POMs by hydrogen bond and π interaction to study magnetic properties. This thesis involves two aspects of investigation:

1) In chapter 3, the equilateral triangle motifs composed of three Ln^{3+} ions bridged by one carbonate ligand were successfully constructed within the sandwich POM anions by introducing highly symmetric organic cations. Furthermore, the influence of symmetry compatibility and hydrogen bonding interaction between cations and POM anion, were studied. The α-lacunary Keggin POMs [PW_9O_{34}] with C_{3v} symmetry, which is in favor of the fabrication of equilateral triangle system consist of three lanthanoid ions, was used. Ten sandwich-type POMs with Ln_3-triangle units as belt, $(CH_3)NH_3^+{}_{10}Na[(PW_9O_{34})_2(H_2OLn)_3CO_3]$ (**1**) (Ln = Tb, Dy, Er and Y, for **1-**

Tb, **1-Dy**, **1-Er** and **1-Y**, respectively, MA = methylammonium), $(CH_3)_2NH_2^+{}_{11}[(PW_9O_{34})_2(H_2OTb)_3CO_3]$ (**2**) (DMA = dimethylammonium), $(CH_3)_3NH^+{}_8Na_3[(PW_9O_{34})_2(H_2OTb)_3CO_3]$ (**3**), (TriMA = trimethylammonium), $(CH_3)_4N^+{}_6Na_5[(PW_9O_{34})_2(H_2OTb)_3CO_3]$ (**4**), (TMA = tetramethylammonium), and $([H_2DABCO]^{2+})_6[(PW_9O_{34})_2(H_2OLn)_3CO_3][BF_4]$ (**5**) (Ln = Tb, Dy and Er for **5-Tb**, **5-Dy** and **5-Er**, respectively), were obtained by introducing organic cations MA^+ ($C_{\infty v}$), DMA^+ (C_{2v}), $TriMA^+$ (C_{3v}) and TMA^+ (T_d), $[H_2DABCO]^{2+}$ (D_{3h}). Three kinds of highly centrosymmetric space groups of $P6_3/m$, $R\bar{3}m$ and $P6_3/mcm$ in crystal **1**, **4** and **5** were achieved, respectively. In crystals **1**, sandwich POM (C_{3h}) anions as vertices are connected by one(N1) of three crystallographically independent MA^+(N1, N2 and N3) cations, giving a highly symmetric 3D framework with cages and channels. In the cage and channel, two kinds of supramolecular units with C_{3h} symmetry as guest molecules accommodate, which were constructed by MA^+(N1 and N3) cations and water molecules through hydrogen bonding interaction to be compatible with sandwich POM (C_{3h}) anions in symmetry as well as size. In **4**, sandwich POM anions maintain C_{3v} symmetry under the templating effect of highly symmetric TMA^+ (T_d) cations. In **5**, the assembly architecture of sandwich POM (C_{2v}) anions is leaded by highly symmetric BF_4^- (T_d) anions through hydrogen bonding interaction not the $[H_2DABCO]^{2+}$ (D_{3h}) cations. On the other hand, two polar space groups of $Pna2_1$ and $Cmc2_1$, were obtained in crystals **2** and **3**, respectively, due to the lower symmetry of DMA^+ and $TriMA^+$ cations and the number of hydrogen-bond sites of only two and one. Two or one hydrogen bond sites aren't easy of forming highly symmetric crystal structures by hydrogen bond net of C_3 symmetry, which is necessary for the formation of equilateral triangle of Ln^{3+} ions. Finally, the equilateral triangle motifs consist of three Ln^{3+} ions bridged by one carbonate ligand were successfully achieved in crystals **1** and **4**. What's more, the magnetic susceptibilities of crystals **1-Tb**, **1-Dy**, **1-Er**, **2**, **3** and **4** exhibit temperature-dependence at low temperature under the applied *dc* filed, typical of slow relaxation of the magnetization and field-induced single molecular magnetic behavior. It's worth noting that the magnetic relaxation in equilateral Ln_3-triangle is more prominent, which will be deeply studied in future.

2) In chapter 4, the supramolecular approach is adopted to isolate SMM structures in crystals. Using (Na)(B18C6) as a counter cation, we succeeded in isolating three fluoride-bridged dinuclear Ln complexes with lacunary Keggin ligands (Ln_2POM) in the crystals $[(Na)(B18C6)(H_2O)_{0.5}]_2[(Na)(B18C6)(H_2O)_{1.5}]_2[(Na)(B18C6)(H_2O)]_2[(Na)(B18C6)(H_2O)$

$_{1.75}]_2[((PW_{11}O_{39})Ln(H_2O)_2)_2F)][(Na)(B18C6)]_2(F)\bullet 12H_2O$ (Ln = Tb, Dy and Er for **6-Tb**, **6-Dy** and **6-Er**, respectively). (Na)(B18C6) was one-dimensionally arranged in the crystal, forming a bamboo-like channel structure. Ln_2POM units were embedded between "bamboo nodes" and completely isolated from neighbouring complexes. Thus, it was possible to evaluate the magnetic properties of Ln_2POM as a single molecule. Weak ferromagnetic interactions between Dy cations bridged by fluoride were observed. Dy_2POM (**6-Dy**) and Er_2POM (**6-Er**) display magnetic relaxation characteristics of an SMM at low temperatures Magnetic relaxation proceeded via the Orbach process, and the absolute values of the effective energy barrier and relaxation time indicated that the SMM properties were essentially attributable to single ions. There are two possible reasons for the observed SMM behaviour: the effect of the diamagnetic lacunary POM ligands and the effect of spatial isolation by supramolecular cations. The supramolecular approach is effective in achieving isolated SMM structures in crystals for complexes where spatial isolation is essential for SMM behaviour. [115] In future, we plan to test its usefulness with other SMM candidate molecules.

Chapter II

Experiment

2-1. Crystal structure determination

Single-crystal X-ray diffraction measurements of the all compounds were carried out on a RIGAKU XtaLAB P200 diffractometer equipped with Cu-Kα (λ = 1.54184 Å) and RIGAKU XtaLAB synergy diffractometer equipped with Mo-Kα (λ = 0.71073 Å). The structures were solved by direct methods using SHELXL and refined by full matrix least-squares techniques on F^2 with SHELX.[116–118] Anisotropic thermal parameters were assigned to all non-hydrogen atoms.

2-2. Elemental Analyses

Elemental analyses for C, H and N were performed on a MICRO CORDER JM10 at Global Facility Center, Hokkaido University.

2-3. Infrared Spectroscopy (IR)

Infrared spectra of crystals **1**, **2**, **3**, **4** and $Na_8H[PW_9O_{34}]$ were recorded by FT-IR spectrum instrument made by Perkin Elmer by transmission through KBr disks containing *ca*. 1 % of the compounds. Each sample were mixed with KBr and pressed into disk. Infrared spectra of crystals **5** and **6** were measured by Nicolet iS10 FTIR spectrum instrument equipped with a ATR-unit (Attenuated Total Reflection).

2-4. Thermogravimetric Differential Thermal Analyses (TG-DTA)

Thermogravimetric differential thermal analyses (TG-DTA) were performed on Rigaku Thermo Plus TG-DTA 8120 thermal analysis station employing an Al_2O_3 reference sample, at the temperature range from 295 to @ K at a heating rate of 5 $K \cdot min^{-1}$ and a cooling rate of 5 $K \cdot min^{-1}$ under a flow of N_2 gas (flow rate 50 $mL \cdot min^{-1}$).

2-5. Measurements of Powder X-ray Diffraction Patterns (PXRD)

Powder X-ray diffraction (XRD) patterns were measured with a Rigaku RINT2100 in the 2θ region of 5 - 50°. The measurements were performed with Cu Kα radiation (λ = 1.5418 Å) at

scanning rate of $1.2° \cdot min^{-1}$ under an applied electric voltage and current of 40 KV and 40 mA, respectively.

2-6. X-ray photoelectron spectroscopy

X-ray photoelectron spectroscopy (XPS) data were collected on a JPS-9200 X-ray photoelectron spectrometer, using monochromatic Al Kα radiations (hν = 1486.6 eV).

2-7. Scanning electron microscopy (SEM) and energy dispersive X-ray spectroscopy (EDS)

SEM images and EDS compositional line profiles were obtained by using SU8230.

2-8. Superconducting Quantum Interference Device (SQUID)

Measurements of direct current magnetic susceptibility were performed on Quantum Design MPMS3 of Faculty of Science, Hokkaido University. And alternating current magnetic susceptibility were conducted on MPMS-5S SQUID magnetometer at science faculty of Hiroshima University. Measurement was made on the sample holder (plastic wrap) under identical conditions.

2-9. Starting materials

All chemicals were of reagent grade and were used as received. Sodium Tungstate (VI) Dihydrate was purchased from Wako Pure Chemical Industries. $RECl_3 \cdot 6H_2O$ (RE = Tb, Dy, Er and Y) were purchased from Merck company. Methylamine Hydrochloride, dimethylammonium hydrochloride, trimethylammonium hydrochloride, tetramethylammonium chloride, *m*-fluoroanilinium and 1,4-Diazabicyclo[2.2.2]octane were purchased from TCI Fine Chemicals. Dibenzo-24-crown-8-ether and Tetrafluoroboric Acid is purchased from Fujifilm company. The precursor lacunary Keggin POM $Na_8H[PW_9O_{34}]$ was obtained according to the literature.[119] $(H_2DABCO^{2+})(BF_4^-)_2$ and (*m*-fluoroanilinium$^+$)(BF_4^-) were synthesized according to literature.[120]

2-10. Synthesis of lacunary POM ($Na_8H[PW_9O_{34}]$)

$$Na_2WO_4{\cdot}2H_2O + H_3PO_4 \xrightarrow{\text{Glacial acetic acid}} Na_8H[PW_{10}O_{32}]$$

Scheme 2-1. The reaction formula of preparing $Na_8H[PW_9O_{34}]$.

120 g (0.36 mol) of sodium tungstate dihydrate $Na_2WO_4{\cdot}2H_2O$ was added into a 300 ml beaker with 150 g of water, stirring with a magnetic stirring bar until the solid was completely dissolved. Phosphoric acid (85%) was added dropwise with stirring (4.0 ml, 0.06 mol). Glacial acetic acid (22.5 ml, 0.40 mol) was added dropwise with vigorous stirring. Large quantities of white precipitate form during the addition. The solution was stirred for 1 h, and the precipitate was collected by suction filtration and heated by vacuum drying at 100 °C. Yield: 62.8 g, 65.1 %. Selected IR data (KBr, cm^{-1}): 3444(s), 1638(s), 1584(w), 1140(w), 1413(m), 1056 (s), 1014 (m), 933 (s), 885 (m), 833 (s), 740～780 (s, broad). A pair of characteristic bands at 1014 and 1056 cm^{-1} corresponding to the v_3 vibrational mode of PO_4 of A-type trivacant Keggin unit implies that the loss of local symmetry. As for the bands at 700-1000 cm^{-1}, that is caused by the asymmetric stretch of the W–O_c–W (700–780 cm^{-1}) and W–O_b–W (880–910 cm^{-1}) bridges and of the W–O_d terminal bonds at around 940 cm^{-1} (O_d is a terminal oxygen, O_b is a bridging oxygen between corner-sharing octahedra, and O_c is a bridging oxygen between edge-sharing octahedra). The reaction formula is shown in scheme 2-1.

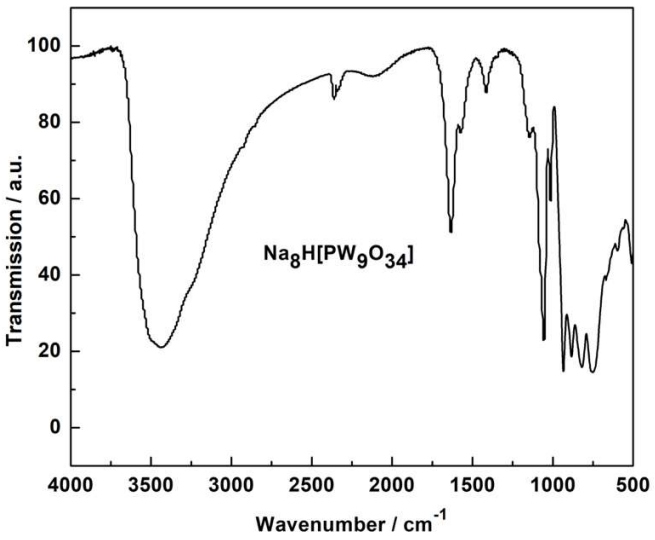

Figure 2-1. The IR spectra of $Na_8H[PW_9O_{34}]$.

2-11. Synthesis of (H_2DABCO^{2+})(BF_4^-)$_2$ and (*m*-fluoroanilinium$^+$)(BF_4^-)

$$DABCO + HBF_4 \xrightarrow{CH_3CN} (H_2DABCO^{2+})(BF_4^-)_2$$

Scheme 2-2. The reaction formula of preparing (H_2DABCO^{2+})(BF_4^-)$_2$.

(H_2DABCO^{2+})(BF_4^-)$_2$ and (*m*-fluoroanilinium$^+$)(BF_4^-) were synthesized by similar procedures reported in literature.[120] The synthesis of (H_2DABCO^{2+})(BF_4^-)$_2$ will be elaborated as representation. To a solution of 30 mL containing 10 mmol (1.12 g) 1,4-Diazabicyclo[2.2.2]octane, 10 mmol (1.6 mL) of HBF_4 is added, stirring for 2 hour. $CHCl_3$ was added into mixture solution, which is left in refrigerator at -10 °C overnight. Then large quantities of white needle crystals formed and collected by suction filtration. The reaction formula is shown in scheme 2-2.

Figure 2-2a shows the infrared spectra of (H_2DABCO^{2+})(BF_4^-)$_2$, the peaks appearing at 1193, 1016, 972, 890, 770 and 763 cm^{-1} attributed to BF_4^- stretching vibrations. The peaks in the ranges 1220-1620 cm^{-1} and 2700-3200 cm^{-1} are associated with the peaks of $[H_2DABCO]^{2+}$ cation.[121] Figure 2-2b shows the infrared spectra of (*m*-fluoroanilinium$^+$)(BF_4^-). The peaks in the ranges 1425-1620 cm^{-1} are assigned to stretching vibration of aromatic ring skeleton. And the peaks around 1292 and 1257 cm^{-1} are ascribed to stretching vibration of C-F bond.[122]

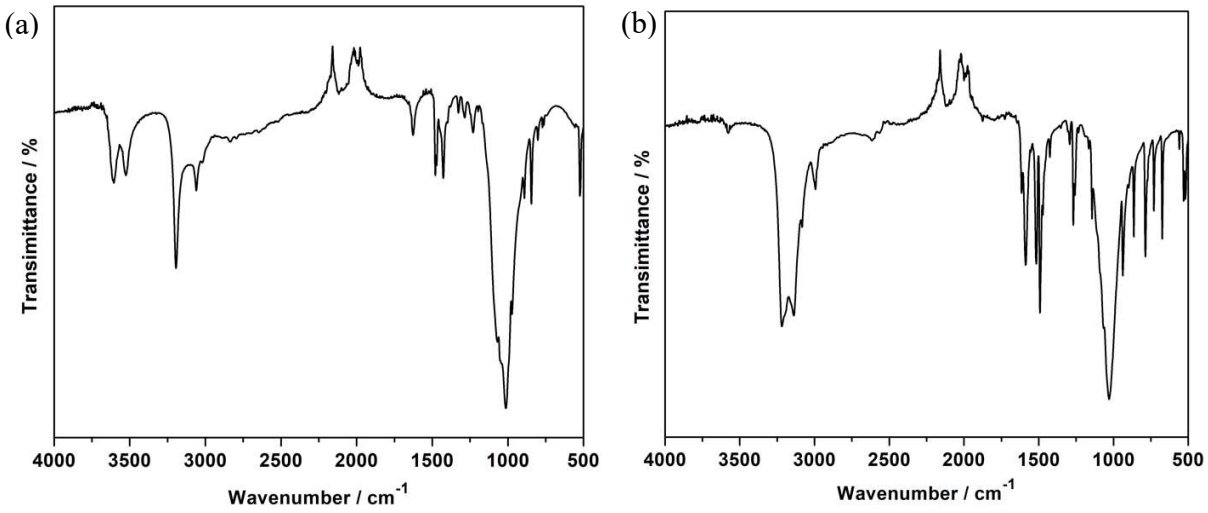

Figure 2-2. The IR spectra of (H_2DABCO^{2+})(BF_4^-)$_2$ (a) and (*m*-fluoroanilinium$^+$)(BF_4^-) (b).

Chapter III

Equilateral and symmetry breaking lanthanoid triangles in sandwich-type polyoxometalates regulated by simple organic cations: magnetic properties

3-1. Introduction

The first lanthanoid SMM, $[TbPc_2]^-$ having only one Tb^{3+} ion at the center of the complex showed a high relaxation energy (U_{eff}) of 331 K that far exceeds the U_{eff} of 3*d*-SMMs.[102] A large number of lanthanoid complexes based on SMM have been studied so far.[105,123–127] Among them, a greatly noticeable thing is that the Dy_3-triangle complexes reported by Powell group show an unprecedented phenomena: features typical of single molecular magnetic behaviors are observed in spite of almost non-magnetic ground state which is due to the toroidal arrangement of magnetic moments on the dysprosium sites in dysprosium(III) triangles.[106,107]

The synthetic combination of lacunary POMs with highly basic oxygen atoms and large oxyphilic lanthanoid cations is a powerful strategy to form polynuclear compounds.[128–133] The μ_3-carbonate-bridged triangles of trivalent rare-earth ions sandwiched between two lacunary Keggin POMs give a nice platform for investigating peculiar magnetic behaviors such as single molecule magnetic behaviors, toroidal magnetic moments, and spin frustration arising from lanthanoid triangles.[134,135] In addition, the advantage of the sandwich POMs is that the unwanted intermolecular magnetic interaction between POMs is so weak due to large size of the molecules which are separated by large numbers of counter cations.[136–140] In the present study, we devoted to constructing equilateral Ln_3-triangle system by adjusting compatibility of symmetry and hydrogen bond interaction between organic cations and sandwich POM anions, which can be platform for investigating novel magnetic properties, such as toroidal magnetic moment, frustrated spin, and SMM behavior and so on.

The ideal lacunary Keggin α-A-POM anion($PW_9O_{34}^{7-}$) possesses symmetry of C_{3v}.[141] Therefore, μ_3-carbonate-bridged triangles of trivalent lanthanoid ions sandwiched between two lacunary Keggin α-A-POMs have potential to give equilateral triangle of trivalent rare-earth ions. Although, the crystals of $K_{10}Na[(A\text{-}\alpha\text{-}AsW_9O_{34})_2(LnOH_2)_3(CO_3)]\cdot nH_2O$ happened to have equilateral triangle structure, most of POMs showed distorted structures in the crystals.[136,138–140,142,143] The crystals of sandwiched POMs with μ_3-carbonate-bridged triangles so far reported possessed simple alkali metal cations as counter cation. Due to highly symmetric cation structure as well as three-dimensionally isotropic nature of coulombic interaction with anionic species, the cations cannot regulate the structure of POMs, which readily distorted according to intermolecular interactions within the packing structure of the crystal.

We already reported that highly flexible supramolecular cations can regulate the crystal symmetry and realize noncentrosymmetric crystal structure even for spherical Keggin crystals.[144] By using counter cations with moderate symmetry, we should regulate the crystal structure of POMs and realize their symmetric structure within the crystal. In this work, we adopted methylammonium (MA^+, $C_{\infty v}$), dimethylammonium (DMA^+, C_{2v}), trimethylammonium($TriMA^+$, C_{3v}) and tetramethylammonium (TMA^+, T_d) having hydrogen bond sites of 3, 2, 1 and 0 as organic counter cations, respectively. A series of POMs with Ln_3-triangle sandwiched were obtained: $(CH_3)NH_3^+{}_{10}Na[(PW_9O_{34})_2(H_2OLn)_3CO_3]$ (**1**) (Ln = Tb, Dy, Er and Y, for **1-Tb**, **1-Dy**, **1-Er** and **1-Y**, respectively, MA = methylammonium), $(CH_3)_2NH_2^+{}_{11}[(PW_9O_{34})_2(H_2OTb)_3CO_3]$ (**2**) (DMA = dimethylammonium), $(CH_3)_3NH^+{}_8Na_3[(PW_9O_{34})_2(H_2OTb)_3CO_3]$ (**3**), (TriMA = trimethylammonium) and $(CH_3)_4N^+{}_6Na_5[(PW_9O_{34})_2(H_2OTb)_3CO_3]$ (**4**), (TMA = tetramethylammonium). And by introducing diprotonated 1,4-Diazabicyclo[2.2.2]octane cation (D_{3h}) and simple anion BF_4^- (T_d), $([H_2DABCO]^{2+})_6[(PW_9O_{34})_2(H_2OLn)_3CO_3][BF_4]$ (**5**) (Ln = Tb, Dy and Er, for **5-Tb**, **5-Dy** and **5-Er**, respectively) were obtained. Successfully, the equilateral Ln_3-triangle motifs were successfully realized by alternating the symmetry compatibility and hydrogen bonding interaction between the introduced organic cations or anions and sandwich POM anions and the magnetic properties of them were studied, as will be discussed in detail.

3-2. Synthesis of crystals $(CH_3)NH_3^+{}_{10}Na[(PW_9O_{34})_2(H_2OLn)_3CO_3]\cdot nH_2O$ (1) (Ln = Tb, Dy, Er and Y for 1-Tb, 1-Dy, 1-Er and 1-Y, respectively, MA = methylammonium), $(CH_3)_2NH_2^+{}_{11}[(PW_9O_{34})_2(H_2OTb)_3CO_3]\cdot 23H_2O$ (2) (DMA = dimethylammonium), $(CH_3)_3NH^+{}_8Na_3[(PW_9O_{34})_2(H_2OTb)_3CO_3]\cdot 15H_2O$ (3), (TriMA = trimethylammonium), $(CH_3)_4N^+{}_6Na_5[(PW_9O_{34})_2(H_2OTb)_3CO_3]\cdot 20H_2O$ (4), (TMA = tetramethylammonium), and $([H_2DABCO]^{2+})_6[(PW_9O_{34})_2(H_2OLn)_3CO_3][BF_4]\cdot 5H_2O$ (5) (Ln = Tb, Dy and Er

for 5-Tb, 5-Dy, 5-Er, respectively).

$(MeNH_3^+)_{10}Na[(PW_9O_{34})_2(H_2OTb)_3CO_3]\cdot 10H_2O$ (**1-Tb**). Solid $TbCl_3\cdot 6H_2O$ was dissolved in 10 mL H_2O, during stirring, then a solution of Na_2CO_3 (1.00 M) was added slowly, giving rise to pH = 6.1. After the temperature of the solution is up to 80 ºC, $Na_8H[PW_9O_{34}]$ (1.0 g, 0.42 mmol) was added and the mixed solution was kept stirring at 80 ºC for 1 hour. Then the solution was cooled to room temperature and centrifugated to remove the insoluble material. Methylamine Hydrochloride (0.27 g, 4.00 mmol) was added into the clear solution and kept still for 1 day, resulting in colorless block crystals. Yield: 26% (based on Tb). Anal. calcd for $C_{11}H_{86}Tb_3N_{10}NaO_{84}P_2W_{18}$ (%): C 2.37, H 1.56, N 2.51; found (%): C 2.24, H 2.01, N 2.42. Selected IR data (KBr, cm^{-1}): 3406(w), 3124(s), 1613(m), 1470(s), 1264(w), 1070(s), 1013(w), 942(w), 912(w), 780(m), 703(m), 514(w).

$(MeNH_3^+)_{10}Na[(PW_9O_{34})_2(H_2ODy)_3CO_3]\cdot 10H_2O$ (**1-Dy**). Synthesized as crystal **1-Tb** except that $TbCl_3\cdot 6H_2O$ was replaced by $DyCl_3\cdot 6H_2O$. Yield: 36% (based on Dy). Anal. calcd for $C_{11}H_{86}Dy_3N_{10}NaO_{84}P_2W_{18}$ (%): C 2.37, H 1.55, N 2.51; found (%): C 2.29, H 1.94, N 2.47. Selected IR data (KBr, cm^{-1}): 3433(w), 3124(s), 1613(m), 1470(s), 1264(w), 1070(s), 1013(w), 942(w), 912(w), 780(m), 703(m), 514(w).

$(MeNH_3^+)_{10}Na[(PW_9O_{34})_2(H_2OEr)_3CO_3]\cdot 9H_2O$ (**1-Er**). Synthesized as crystal **1-Tb** except that $TbCl_3\cdot 6H_2O$ was replaced by $ErCl_3\cdot 6H_2O$. Yield: 36% (based on Er). Anal. calcd for $C_{11}H_{84}Er_3N_{10}NaO_{83}P_2W_{18}$ (%): C 2.37, H 1.52, N 2.51; found (%): C 2.25, H 1.88, N 2.40. Selected IR data (KBr, cm^{-1}): 3417(m), 3130(s), 1613 (m), 1481(s), 1264 (w), 1070(s), 1013(w), 942(w), 912(w), 780(m), 696(m), 514(w).

$(MeNH_3^+)_{10}Na[(PW_9O_{34})_2(H_2OY)_3CO_3]\cdot 8.5H_2O$ (**1-Y**). Synthesized as crystal **1-Tb** except that $TbCl_3\cdot 6H_2O$ was replaced by $YCl_3\cdot 6H_2O$. Yield: 35% (based on Y). Anal. calcd for $C_{11}H_{83}Y_3N_{10}NaO_{82.5}P_2W_{18}$ (%): C 2.47, H 1.57, N 2.62; found (%): C 2.30, H 2.07, N 2.45. Selected IR data (KBr, cm^{-1}): 3439(m), 3130(s), 1613(m), 1488(s), 1264(w), 1070(s), 1016(w), 944(w), 912(w), 787(m), 703(m), 514(w).

$(CH_3)_2NH_2^+{}_{11}[(PW_9O_{34})_2(H_2OTb)_3CO_3]\cdot 23H_2O$ (**2**). Synthesized as crystal **1-Tb** except that methylammonium hydrochloride was replaced by dimethylammonium hydrochloride. Yield: 37% (based on Tb). Anal. calcd for $C_{23}H_{140}Tb_3N_{11}O_{97}P_2W_{18}$ (%): C 4.63, H 2.36, N 2.58; found (%): C

3.87, H 1.28, N 1.97. Selected IR data (KBr, cm^{-1}): 3447(s), 3112(w), 2968(w), 2790(m), 2425(w), 1625(s), 1465(s), 1242(w), 1062(s), 1009(s), 944(w), 913(w), 782(m), 700(m), 515(m).

$(CH_3)_3NH^+_8Na_3[(PW_9O_{34})_2(H_2OTb)_3CO_3]\cdot 15H_2O$ (**3**). Synthesized as crystal **1-Tb** except that methylammonium hydrochloride was replaced by trimethylammonium hydrochloride. Yield: 20% (based on Tb). Anal. calcd for $C_{25}H_{116}Tb_3N_8Na_3O_{89}P_2W_{18}$ (%): C 5.12, H 1.99, N 1.91; found (%): C 5.90, H 1.71, N 2.13. Selected IR data (KBr, cm^{-1}): 3436(s), 3084(w), 3015(w), 2956(m), 2705(s), 2475(m), 1630(m), 1476(s), 1254(m), 1062(s), 1005(w), 982(s), 936(m), 910(w), 783(s), 700(m), 512(w).

$(CH_3)_4NH^+_6Na_5[(PW_9O_{34})_2(H_2OTb)_3CO_3]\cdot 20H_2O$ (**4**). Synthesized as crystal **1-Tb** except that methylammonium hydrochloride was replaced by tetramethylammonium hydrochloride. Yield: 37% (based on Tb). Anal. calcd for $C_{25}H_{118}Tb_3N_6Na_5O_{94}P_2W_{18}$ (%): C 5.03, H 1.99, N 1.41; found (%): C 4.97, H 1.40, N 1.27. Selected IR data (KBr, cm^{-1}): 3463(s), 3030(w), 1625(m), 1483(s), 1264(w), 1070(s), 1010(m), 944(w), 907(w), 783(s), 696(m), 501(w).

$([H_2DABCO]^{2+})_6[(PW_9O_{34})_2(H_2OTb)_3CO_3][BF_4]\cdot 5H_2O$ (**5-Tb**). Synthesized as crystal **1-Tb** except that methylammonium hydrochloride was replaced by $(H_2DABCO^{2+})(BF_4^-)_2$ (2 mmol, 0.5756 g) and DABCO (2 mmol, 0.224 g). Yield: 8% (based on Tb). Selected IR data (KBr, cm^{-1}): 3416(s), 3017(s), 2815(w), 2787(w), 2631(w), 1620(s), 1498(s), 1471(m), 1397(w), 1364(w), 1327(w), 1213(w), 1055(s), 1010(m), 936(s), 908(m), 889(w), 829(s), 781(s), 689(s), 579(w), 517(w).

$([H_2DABCO]^{2+})_6[(PW_9O_{34})_2(H_2ODy)_3CO_3][BF_4]\cdot 5H_2O$ (**5-Dy**). Synthesized as crystal **1-Tb** except that $TbCl_3\cdot 6H_2O$ was replaced by $DyCl_3\cdot 6H_2O$. Yield: 18% (based on Dy). Anal. calcd for $C_{37}N_{12}H_{100}BF_4Dy_3O_{79}P_2W_{18}$ (%): C 7.50, H 1.70, N 2.84; found (%): C 7.70, H 1.59, N 2.81. Selected IR data (KBr, cm^{-1}): 3414(s), 3011(s), 2813(w), 2784(w), 2634(w), 1620(s), 1495(s), 1465(m), 1391(w), 1361(w), 1325(w), 1215(w), 1052(s), 1008(m), 934(s), 907(m), 882(w), 828(s), 775(s), 688(s), 578(w), 513(w).

$([H_2DABCO]^{2+})_6[(PW_9O_{34})_2(H_2OEr)_3CO_3][BF_4]\cdot 5H_2O$ (**5-Er**). Synthesized as crystal **1-Tb** except that $TbCl_3\cdot 6H_2O$ was replaced by $ErCl_3\cdot 6H_2O$. Yield: 8% (based on Er). Anal. calcd for $C_{37}N_{12}H_{100}BF_4Er_3O_{79}P_2W_{18}$ (%): C 7.49, H 1.70, N 2.83; found (%): C 7.45, H 1.53, N 2.73. Selected IR data (KBr, cm^{-1}): 3416(s), 3017(s), 2811(w), 2787(w), 2631(w), 1620(s), 1498(s), 1471(m), 1397(w), 1363(w), 1327(w), 1212(w), 1055(s), 1010(m), 936(s), 908(m), 888(w), 829(s), 781(s), 689(s), 579(w), 517(w).

3-3. Crystal structure of crystal 1.

X-ray diffraction data reveals that the crystals of **1**, $(CH_3)NH_3^+{}_{10}Na[(PW_9O_{34})_2(H_2OLn)_3CO_3]\cdot nH_2O$ (Ln = Tb, Dy, Er, and Y for **1-Tb**, **1-Dy**, **1-Er** and **1-Y**), were isomorphous, crystalizing in the highly symmetric hexagonal space group $P6_3/m$. The crystal structure of crystal **1-Tb** will be discussed in detail for representation. Crystal **1-Tb** consists of 1/6 sandwich POM anion, 1/3 Na^+ cation, 5/3 MA^+ cations (N1, N2 and N3) and 17/6 water molecules within independent unit as shown in Figure 3-1. As shown in Figure 3-2, a triangle ($\{Tb_3CO_3\}$) unit composed of three Tb^{3+} ions bridged by a μ_3-η^2:η^2:η^2-carbonate ligand is sandwiched between two lacunary Keggin {A-α-PW_9O_{34}} units. The carbonate-bridged terbium triangle is equilateral with Tb···Tb distance of 4.890 Å, which is on the mirror plane with C_3 axis perpendicular to the triangle plane through the carbon atom in carbonate. Each oxygen atom of carbonate jointing two of three Tb^{3+} ions doesn't lie on the edge of equilateral triangle and the Tb-O distances are different to each other (Tb1–$O_{carbonate}$ = 2.432 Å, Tb1–$O^1{}_{carbonate}$ = 2.463 Å. Therefore, C_{3h} symmetry is observed in sandwich POM anion of crystal **1-Tb**. The encapsulated CO_3^{2-} displays D_{3h} symmetry, which is unusual in metallocarbonate complexes.[136,138–140,145]

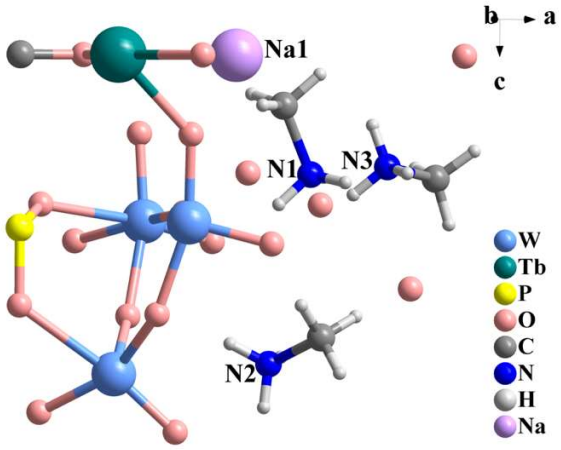

Figure 3-1 The asymmetric unit of crystal **1-Tb**.

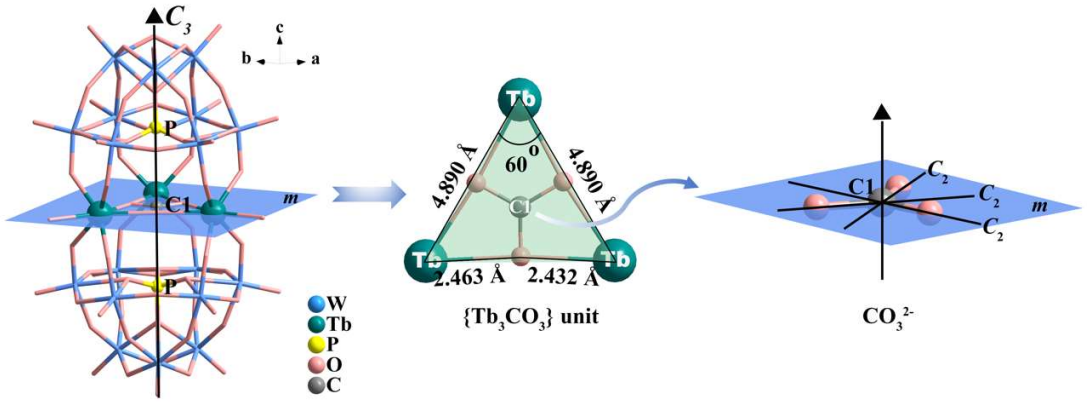

Figure 3-2. The structure of sandwich POM anion in crystal **1-Tb**. The equilateral triangle structure constructed by {$TbCO_3$}unit (Middle). The symmetry of CO_3^{2-} in {$TbCO_3$}unit (right).

The polymer framework of crystal **1** is constructed from sandwich POM anions as vertices and one (N2) of three crystallographycally independent MA^+ cations (N1, N2 and N3) as linkers. And supramolecular units constructed of one of another two crystallographycally independent MA^+ cations (N2 and N3) as guest molecules accommodate in the framework. As shown in Figure 3-3a, it can be found every sandwich POM anion is surrounded by twelve MA^+ cations (N2), which are evenly distributed on both sides of the triangle({Tb_3CO_3}) plane by hydrogen bonding interaction (N2-H···O12(POM) = 2.956 Å, <N2-H···O12(POM) = 151.13°, N2-H···O17(POM) = 2.995 Å, <N2-H···O17(POM) = 172.89°, N2-H···O19(POM) = 3.047 Å, <N2-H···O19(POM) = 165.99°). Each sandwich POM anion is connected to six sandwich POM anions, through (MA)N2-H···O(POM) hydrogen bonding interaction, forming triangular bipyramid structure (large secondary building units, SBUs) with a approximately spherical-like nano-sized cage with a diameter of about 6.23 Å (taking into account the van der Waals radii of the atoms) (Figure 3-3b). The key SBU in crystal **1** is a bipyramidal unit with five sandwich POM anions at five vertices connected by twelve MA^+ (N2) cations. The framework was then achieved by connecting the SBU with other units through corner sharing of the triangular bipyramid. A view down *c* direction reveals threefold symmetric one-dimensional (1D) cylindrical channels with the diameter of 5.4 Å along (taking into account the van der Waals radii of the atoms) as shown in Figure 3c.

The sandwich POM anion unit provides a structural motif with threefold symmetry, and the MA^+(N2) cations linkers provide an infinite axis symmetry element. However, it is not the direct combination of these two that creates the highly symmetric hexagonal space group of the crystal, because C_∞ axis of MA^+(N2) cations aren't coincident with the C_3 axis of sandwich POM anion

unit. Instead, the origin of the nanometer-sized channels can be considered as arising from the formation of lager secondary building units (Figure 3-3b).

Two kinds of supramolecular units possessing C_{3h} symmetry constructed from one of the other two crystallographically independent MA^+ (N1 and N3) cations exist as guest molecules in the cages and channels of the framework structure of crystal **1**, which will be elaborated next.

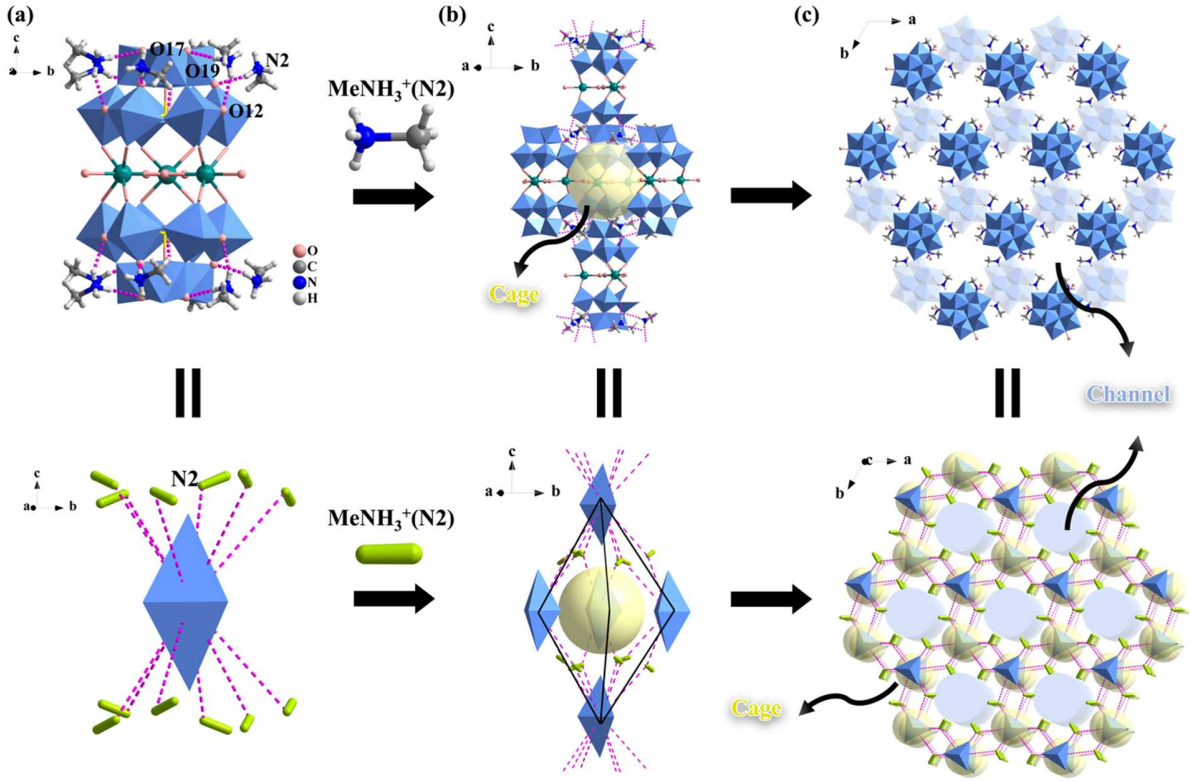

Figure 3-3. Single crystal structure of crystal **1**. (a) Sandwich POM anions as subunits are connected to 12 MA^+ (N2) cations as linkers by hydrogen bonding interaction. The sandwich POM anion is abstracted as a triangular bipyramidal (bottom). (b) The bipyramidal cage built from the stack arrangement of five sandwich POM anions connected by MA^+ (N2) cations through hydrogen bonding interaction. (c) 3D framework structure with a 1D cylindrical channel along the crystallographic *c*-axis. Hydrogen bonding is shown in magenta dotted line.

As shown in Figure 3-4, for crystal **1**, as guest molecules, supramolecular units ($\{(MeNH_3^+)_2H_2O\}$) of another crystallographically independent MA^+ (N1) is formed in the cage. For crystal **1-Tb**, **1-Dy** and **1-Er**, $\{(MeNH_3^+)_2H_2O\}$ is composed of six disordered MA^+ cations (N1) and two disordered water molecules (O1), with the occupancy of 1/3 and 1/2 for N1 and O1,

respectively. Resembling a pair of cymbals, two disordered water molecules (O1) on the C_3 axis are each connected to three disordered MA^+ (N1) cations through hydrogen bonding interaction (Table 3-1), thus constituting supramolecular unit $\{(MeNH_3^+)_2(H_2O)\}$ with C_{3h} symmetry. And for crystal **1-Y**, $\{(MeNH_3^+)_2H_2O\}$ is composed of six disordered MA^+ cations (N1) and three disordered water molecules (O1), with the occupancy of 1/3 for both N1 and O1, in which three disordered water molecules (O1) at mirror plane are sandwiched between six MA^+ cations by hydrogen-bond interaction (Table 3-1). The $\{(MeNH_3^+)_2(H_2O)\}$ is connected to five surrounding sandwich POM anions by hydrogen-bond interaction as shown in Figure 3-5 and Table 3-2.

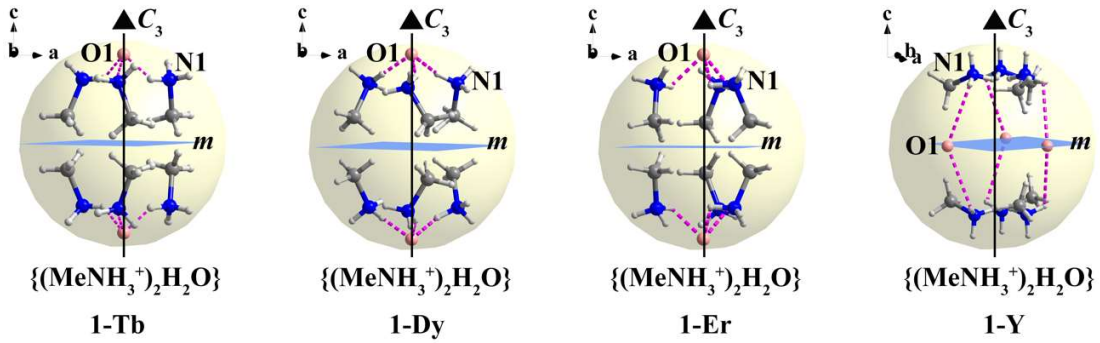

Figure 3-4. Hydrogen bonding supramolecular units ($\{(MeNH_3^+)_2H_2O\}$) constructed by MA^+ (N1)cations and water molecules (O1) accommodated in the cage of **1**. Hydrogen bonding is shown in magenta dotted line.

Table 3-1. The data of hydrogen bond existing in supramolecular units($\{(MeNH_3^+)_2H_2O\}$) accommodating in the cage of crystal **1**.

Compound	Hydrogen bonding units	Distance/ Å	Angle/°
1-Tb	N1-H···O1(H_2O)	2.004	152.90
1-Dy	N1-H···O1(H_2O)	2.312	154.81
1-Er	N1-H···O1(H_2O)	2.128	102.29
1-Y	N1-H···O1(H_2O)	3.226	106.49

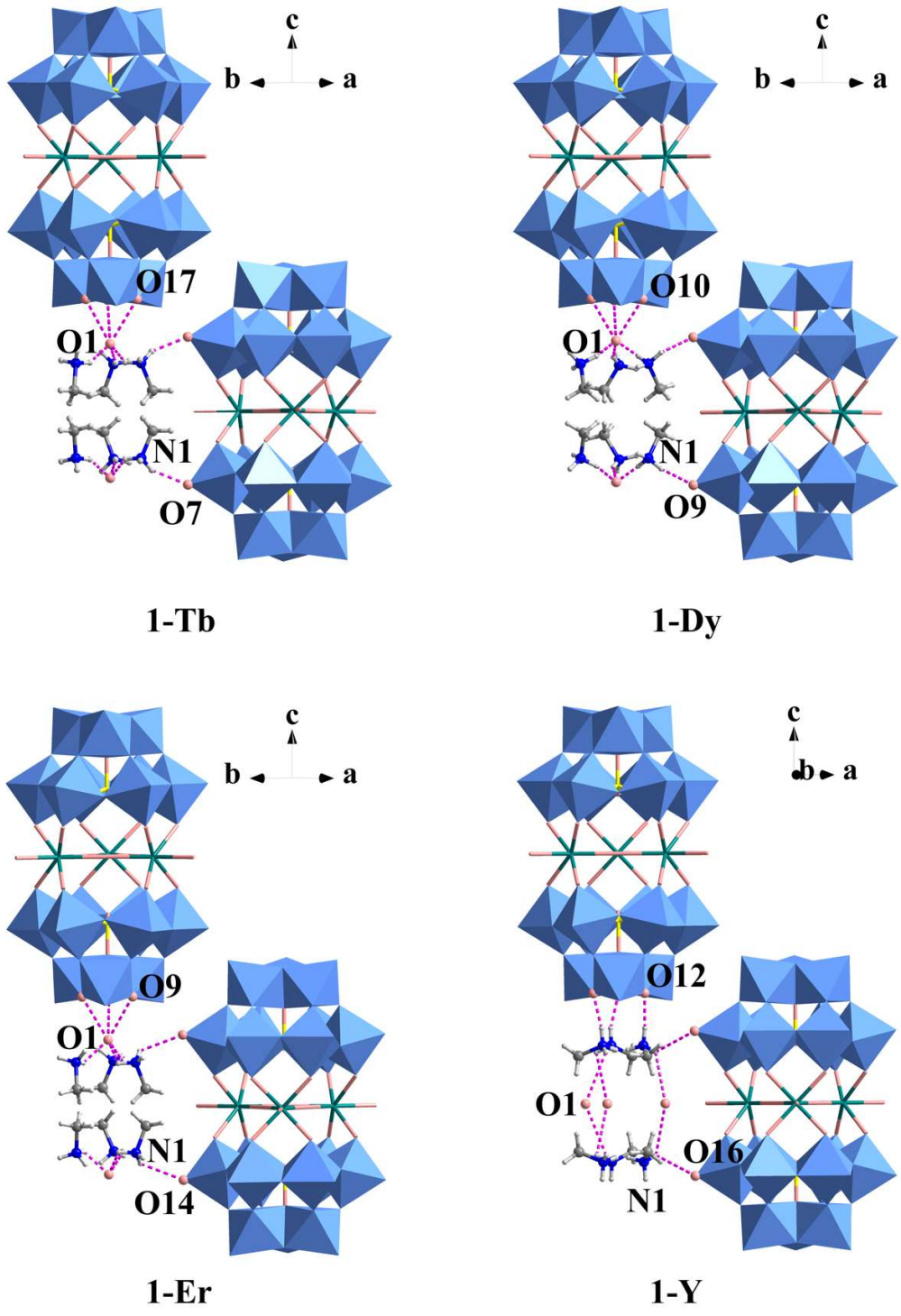

Figure 3-5. The hydrogen bonding interaction between $\{(MeNH_3^+)_2H_2O\}$ units existing in cages and surrounding sandwich POM anions in crystal **1**. Hydrogen bonding is shown in magenta dotted line.

Table 3-2. The data of hydrogen bonding between supramolecular units($\{(MeNH_3^+)_2H_2O\}$) accommodating in the cage and surrounding sandwich POM anions in crystal **1**.

Compound	Hydrogen bonding units	Distance/ Å	Angle/°
1-Tb	N1-H···O7(POM)	2.784	148.16
	O1(H_2O)···O17(POM)	3.163	
1-Dy	N1-H···O9(POM)	2.705	138.74
	O1(H_2O)···O10(POM)	2.585	
1-Er	N1-H···O14(POM)	2.824	101.50
	O1(H_2O)···O9(POM)	2.690	
1-Y	N1-H···O12(POM)	2.756	164.94
	N1-H···O16(POM)	2.819	96.50

As shown in Figure 3-6, the channel was filled with supramolecular units $\{(MeNH_3^+)_2(H_2O)_3\}$ of another crystallographycally independent MA^+(N3) for crystals **1-Tb**, **1-Dy** and **1-Er**. For crystal **1-Y**, supramolecular unitss $\{(MeNH_3^+)_2(H_2O)_{1.5}\}$ of MA^+ (N3) were filled in the channel. In the channel of **1**, $\{(MeNH_3^+)_2(H_2O)_x\}$ units are stacking along the crystallographic *c* axis in a 3-fold helical manner (Figure 3-6b). Resembling an ancient Chinese sandglass, one water molecule (O4, crystal **1-Tb** and **1-Dy**) or three disordered water molecules (O4, crystal **1-Er**) at center is connected to six disordered MA^+ cations showing C_{3h} symmetry, and each disordered MA^+ cation is connected to another disordered water molecule (O3), through hydrogen bonding interaction (Table 3-3), giving supramolecular unit $\{(MeNH_3^+)_2(H_2O)_3\}$. The occupancy of both N3(MA^+) and O3(H_2O) is 1/3 in **1-Tb**, **1-Dy** and **1-Er**, respectively. Different from **1-Tb**, **1-Dy**, the water molecule (O4) in crystal **1-Er** is disordered at three positions with the occupancy of 1/3 for O4. For crystal **1-Y**, three disordered water molecules (O4) at mirror plane are sandwiched between six disordered MA^+ (N3) cations, and then every three disordered MA^+ (N3) cations are connected to one disordered water molecules (O3) by hydrogen bonding interaction (Table 3-3), giving rise to $\{(MeNH_3^+)_2(H_2O)_{1.5}\}$ with C_{3h} symmetry. The occupancy of N3(MA^+), O3(H_2O) and O4(H_2O) is 1/3, 1/4 and 1/3 in **1-Y**, respectively. $\{(MeNH_3^+)_2(H_2O)_x\}$ in the channel is connected to three surrounding sandwich POM anions by hydrogen bonding interaction as shown in Figure 3-7 and Table 3-4.

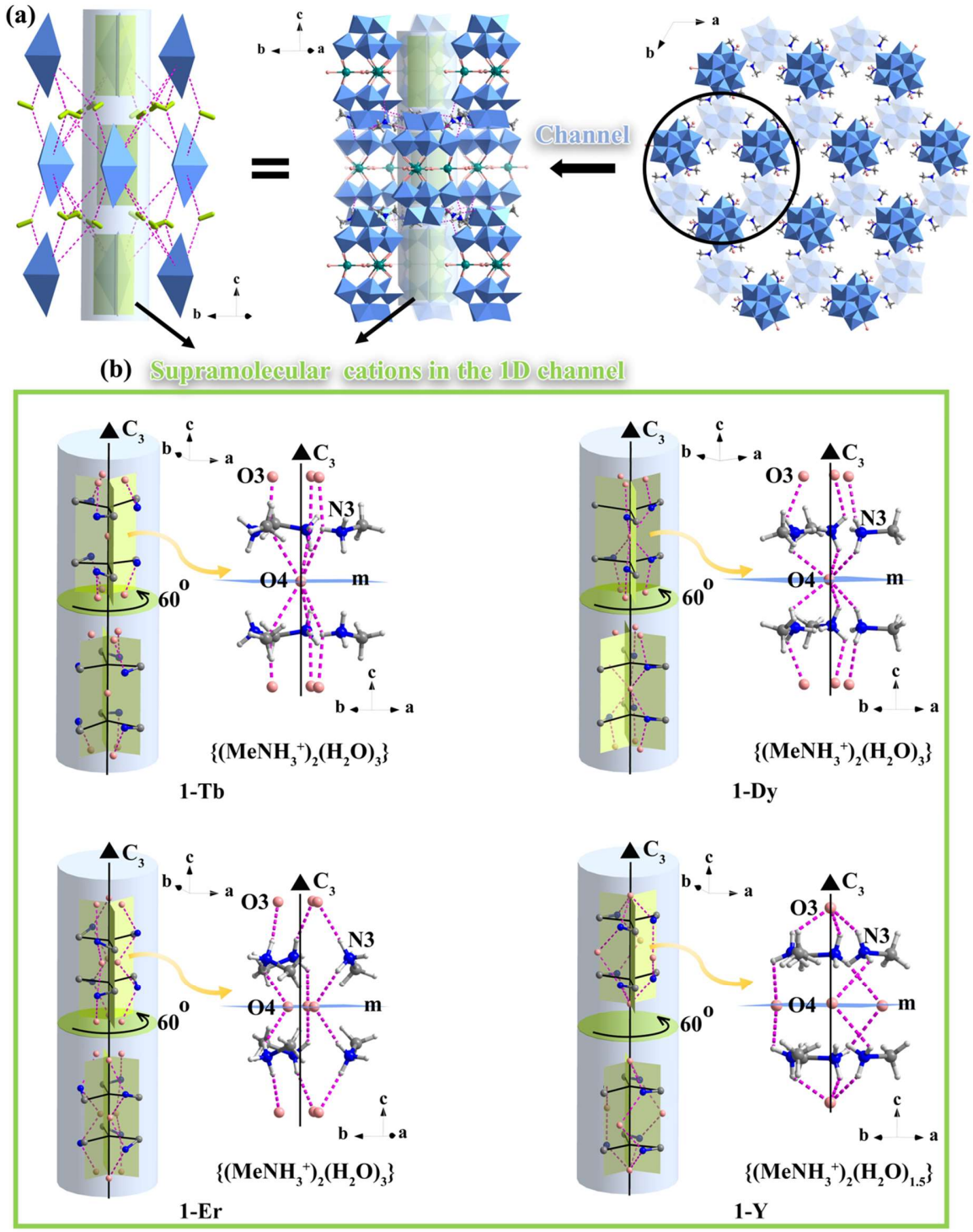

Figure 3-6. (a) Threefold symmetric one-dimensional (1D) cylindrical channels in crystal **1**. (b) The structure of hydrogen bonding supramolecular units ($\{(MeNH_3^+)_2(H_2O)_x\}$) constructed by MA^+ (N3) cations and water molecules (O3 and O4) accommodated in the channel of crystal **1**. Hydrogen bonding is shown in magenta dotted line.

Table 3-3. The data of hydrogen bonding existing in supramolecular units ($\{(MeNH_3^+)_2(H_2O)_x\}$) accommodating in the channel of crystal **1**.

Compound	Hydrogen bonding units	Distance/ Å	Angle/°
1-Tb	N3-H···O3(H_2O)	2.710	96.60
	N3-H···O4(H_2O)	3.021	109.75
1-Dy	N3-H···O3(H_2O)	2.698	116.39
	N3-H···O4(H_2O)	2.821	119.56
1-Er	N3-H···O3(H_2O)	3.017	170.04
	N3-H···O4(H_2O)	2.775	134.10
1-Y	N3-H···O3(H_2O)	2.685	128.03
	N3-H···O4(H_2O)	3.076	111.20

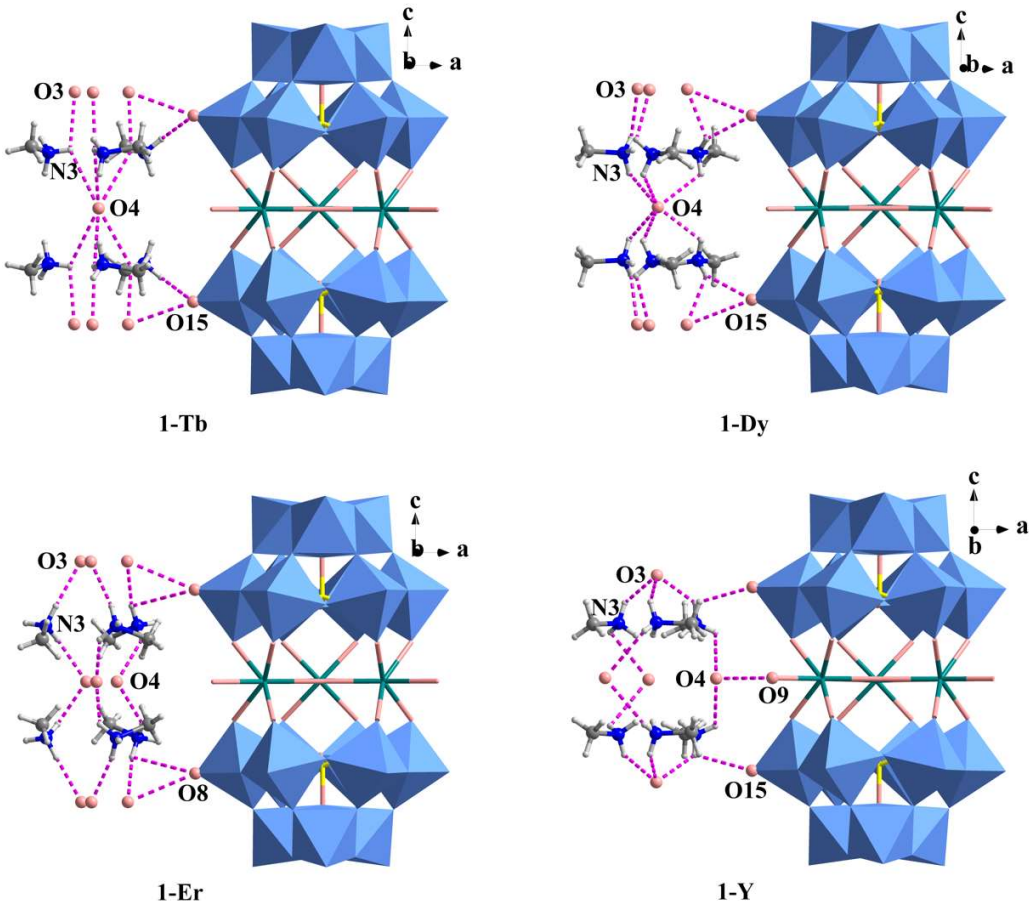

Figure 3-7. The hydrogen bonding interaction between $\{(MeNH_3^+)_2(H_2O)_x\}$ units existing in channel and surrounding sandwich POM anions in crystal **1**. Hydrogen bonding is shown in magenta dotted line.

Table 3-4. The data of hydrogen bonding between $\{(MeNH_3^+)_2(H_2O)_x\}$ units accommodating in the channel and surrounding sandwich POM anions in crystal **1-Ln**.

Compound	Hydrogen bonding units	Distance/ Å	Angle/°
1-Tb	N3-H···O15(POM)	2.907	153.76
	O3(H_2O)···O15(POM)	2.916	
1-Dy	N3-H···O15(POM)	3.014	146.21
	O3(H_2O)···O15(POM)	2.996	
1-Er	N3-H···O8(POM)	3.535	108.58
	O3(H_2O)···O8(POM)	2.888	
1-Y	N3-H···O15(POM)	3.044	111.96
	O3(H_2O)···O15(POM)	3.103	

In addition, as shown in Figure 3-8, the shortest distance between Tb^{3+} ions of neighboring POM anions is 11.564 Å, which means no inter POM interaction exists in crystal **1-Tb**.

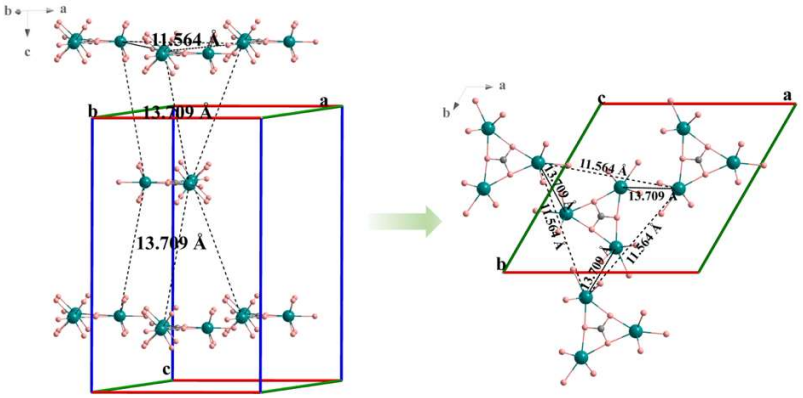

Figure 3-8. The distance between Tb^{3+} ions of sandwich POM anions of crystal **1-Tb**.

3-4. Crystal structure of crystal 2.

X-ray results shows that crystal **2** crystalizes in orthorhombic $Pna2_1$ polar space group. Crystallographically independent unit consist of one sandwich POM anion, eleven DMA^+ (N1, N2, N3, N4, N5, N6, N7, N8, N9, N10, N11) cations and 23 water molecules (Figure 3-9). The structure of sandwich POM anion is similar with the anion of crystal **1** except for symmetry. As shown in Figure 3-10, the $\{Tb_3CO_3\}$ formed scalene with Tb···Tb distance of 4.915 Å, 4.852 Å and 4.868

Å. The D_{3h} symmetry of encapsulated CO_3^{2-} ligand disappeared at the same time. In addition, the P-C-P bonds between carbonate carbon and axial phosphorous atoms were distorted (<P1–C1–P2 = 178.19°, P1···C: 3.559 Å, P2···C: 3.536 Å), showing that sandwich POM has polar structure.

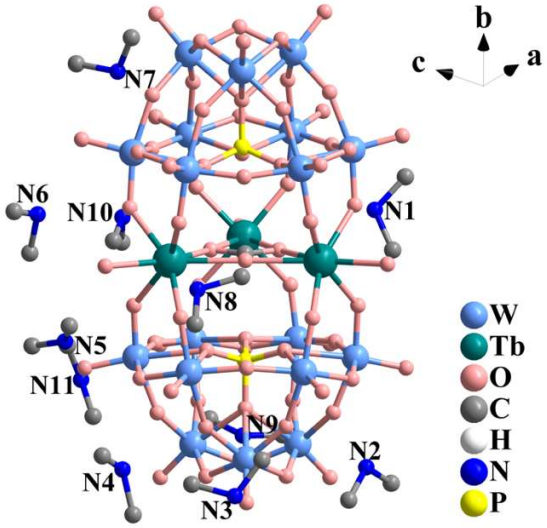

Figure 3-9. The asymmetric unit of crystal **2-Tb**.

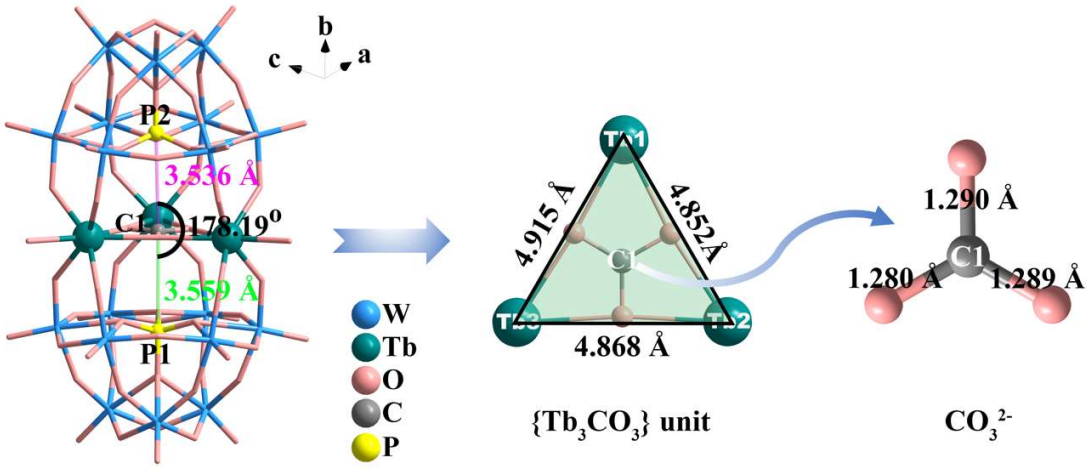

Figure 3-10. The structure of sandwich POM anion in crystal **2**. The distorted triangle structure constructed by {$TbCO_3$}unit (Middle). The structure of CO_3^{2-} in {$TbCO_3$}unit (right). The distance between P1and C1 and the distance between P2 and C1 are shown in light green and magenta, respectively.

As shown in Figure 3-11, we can find that sandwich POM anions assemble in zigzag style along *a* axis, which are aligned parallel to *b* axis and closed packing along the *c* axis. It can be noticed that neighboring polar sandwich POM anions are arranged in opposite directions whether in *a*

direction or in *b* direction, indicating that polarity are canceled in *a* or *b* direction. As shown in Figure 3-11a, all polar sandwich POM anions are arranged at same direction along *c* axis, generating $Pna2_1$ polar space group. In the cavity between sandwich POM anions, DMA^+ cations and water molecules fill. It can be noticed that C_3 symmetry hasn't been given in crystal **2**, which may be assigned to only two hydrogen bond sites exist in DMA^+ cation. It's difficult for two hydrogen bond sites to form structure with C_3 symmetry. The shortest distance between Tb^{3+} ions of neighboring POM anions is 9.457 Å shown in Figure 3-12**,** implying no interaction between POM anions.

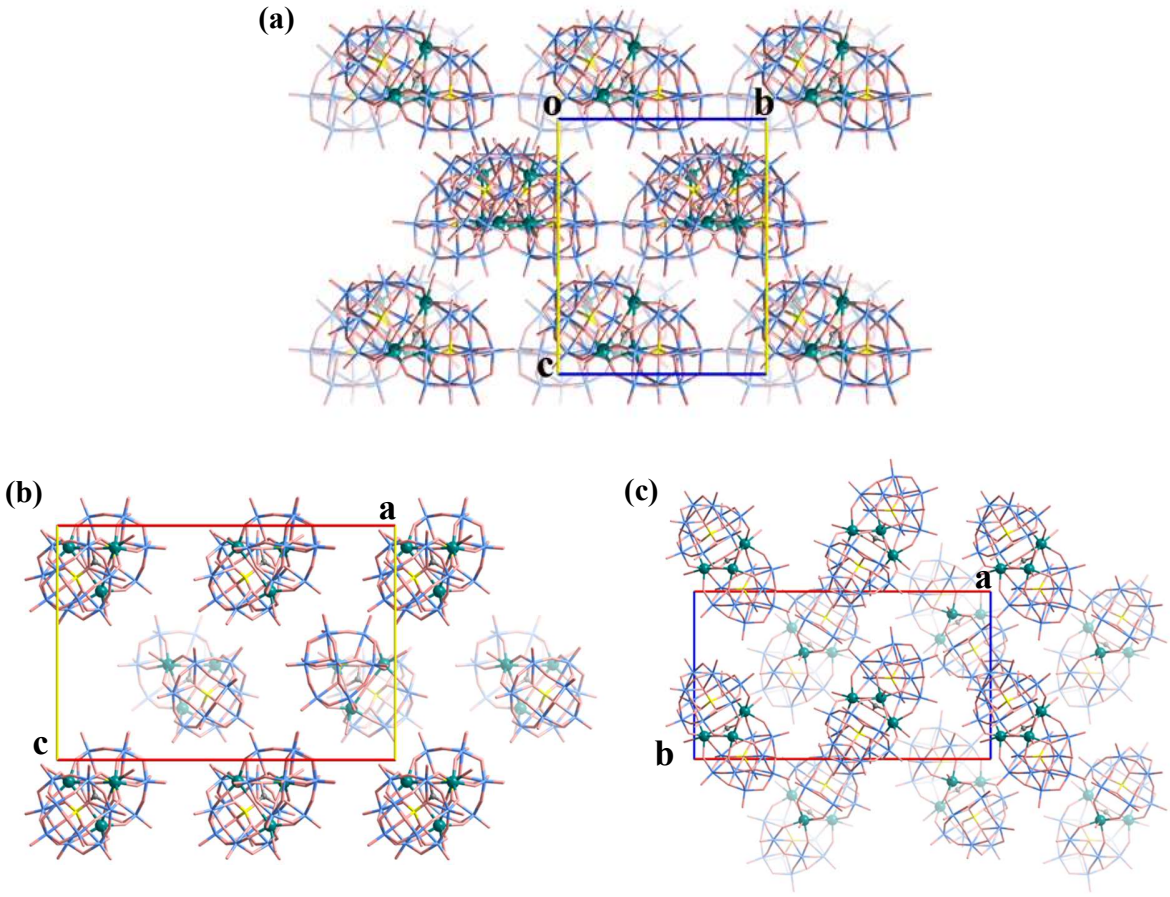

Figure 3-11. The packing arrangement of sandwich POM anions along *a* axis (a), *b* axis (b) and *c* axis (c) in crystal **2**.

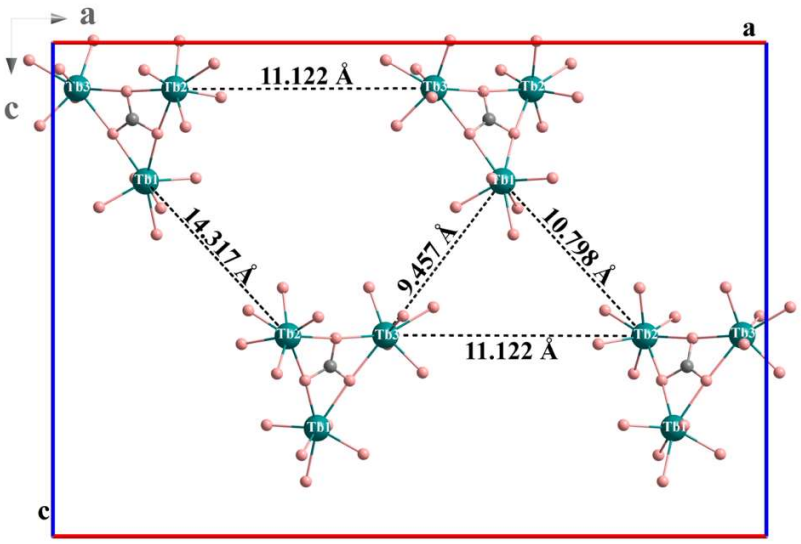

Figure 3-12. The distance between Tb^{3+} ions of sandwich POM anions of crystal **2.**

3-5. Crystal structure of crystal 3.

For the crystal structure of **3**, it also belongs to orthorhombic group, crystalizing in polar $Cmc2_1$ space group. As shown in Figure 3-13, there are half sandwich POM anions, 5/2 Na^+ ions, 11/2 $TriMA^+$ (N1, N2, N3, N4, N5, N6) cations and 17/2 water molecules in its crystallographically independent unit**.** The structure of sandwich POM anion within crystal **3** is also distorted as in the case of crystal **2**, with isosceles-type triangle$\{Tb_3CO_3\}$, Tb···Tb distances of 4.861 Å, 4.861 Å and 4.867 Å, respectively, and the D_{3h} symmetry of CO_3^{2-} ligand is lost. The P-C-P bonds between carbonate carbon and axial phosphorous atoms are distorted (<P1–C1–P2 = 179.02º, P1···$C_{carbonate}$: 3.567 Å, P2···$C_{carbonate}$: 3.536 Å) (Figure 3-14).

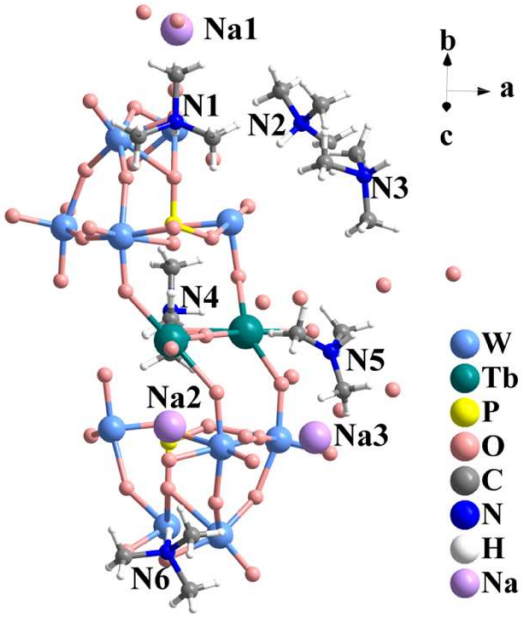

Figure 3-13. The asymmetric unit of crystal **3-Tb**.

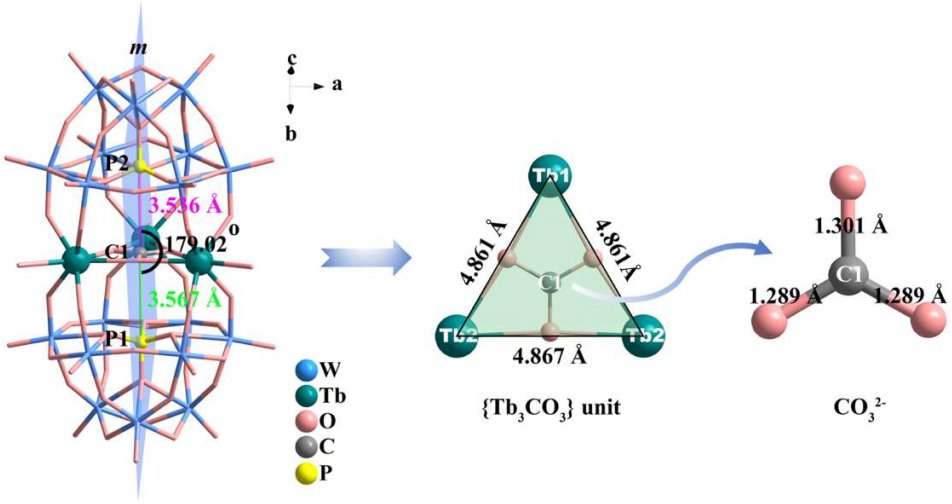

Figure 3-14. The structure of sandwich POM anion in crystal **3**. The isosceles triangle structure constructed by {$TbCO_3$}unit (Middle). The structure of CO_3^{2-} in {$TbCO_3$}unit (right). The distance between P1and C1 and the distance between P2 and C1 are shown in light green and magenta, respectively.

As shown in Figure 3-15, sandwich POM anions are packing with rhombus-like style along the *ac* plane, and then closed pack along the *b* axis. Na^+ ions, $TriMA^+$ cations and water molecules occupy the space between sandwich POM anions. It can be found that C_3 symmetry isn't displayed in packing structure of crystal **1-Tb** but symmetry of mirror plane parallel with *bc* plane mentioned before, which means polarity of sandwich POM anions are cancelled along *a* axis. In addition, as

shown in Figure 3-15c, the polarity along *b* axis is 0 because polar sandwich POM anions are arranged in opposite directions. However, along the *c* axis, neighboring polar sandwich POM anions are arranged in same direction, thus forming the polar axis for $Cmc2_1$ space group (Figure 3-15a). The closest distance between Tb^{3+} ions of neighboring sandwich POM anions is 10.315 Å, indicating no interaction between sandwich POM anions (Figure 3-16).

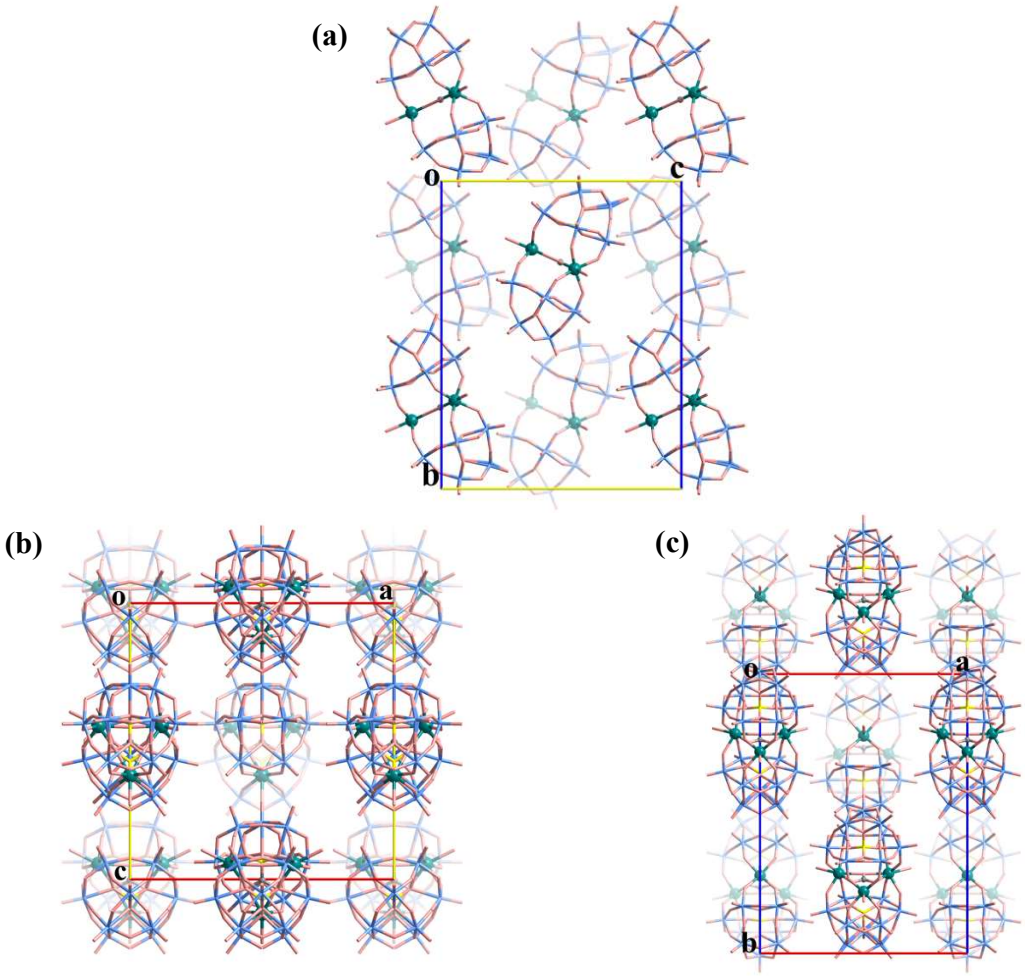

Figure 3-15. The packing arrangement of sandwich POM anions along *a* axis (a), *b* axis (b) and *c* axis (c) in crystal **3**.

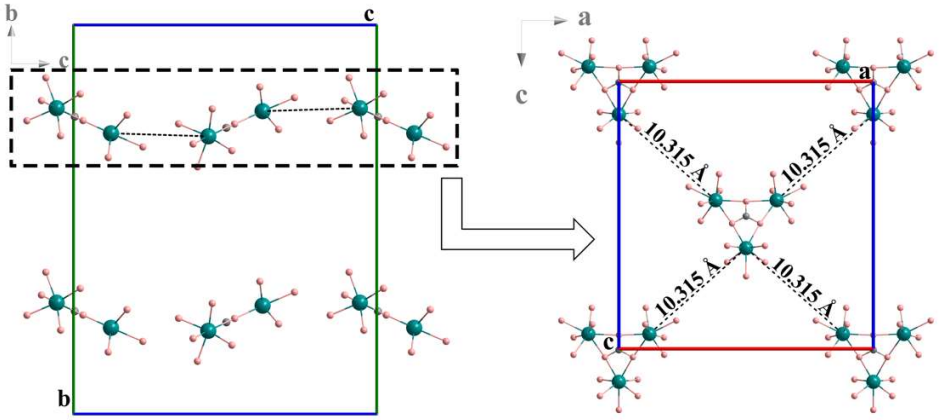

Figure 3-16. The distance between Tb^{3+} ions of sandwich POM anions of crystal **3**.

3-6. Crystal structure of crystal 4.

The crystal of **4** belongs to highly symmetric trigonal $R\bar{3}m$ space group. The crystal consists of 1/6 sandwich POM anions, two TMA^+ cation, 4/3 disordered Na^+ ions and $7\frac{1}{12}$ water molecules partially disordered within independent unit (Figure 3-17). As shown in Figure 3-18, similar with crystal **1**, the $\{Tb_3CO_3\}$ triangle is equilateral with Tb···Tb distance of 4.876 Å, with C_3 rotation axis through carbon atom perpendicular to the carbonate plane. Different from crystal **1**, there are three mirror planes through C_3 axis, perpendicular with $\{Tb_3CO_3\}$ triangle plane in crystal **4**, giving the same distance between every O atom of carbonate ligand and every Tb^{3+} ion (Tb1–$O_{carbonate}$ = 2.441 Å). The original D_{3h} symmetry of encapsulated CO_3^{2-} ligand is kept as in the case of crystal **1**. On the other hand, distances between P atoms and $C_{carbonate}$ atom was different to each other(<P1–$C_{carbonate}$–P2 = 180°, P1··· $C_{carbonate}$: 3.581 Å, P2··· $C_{carbonate}$: 3.571 Å). As a result, the sandwich POM anion adopts C_{3v} symmetry.

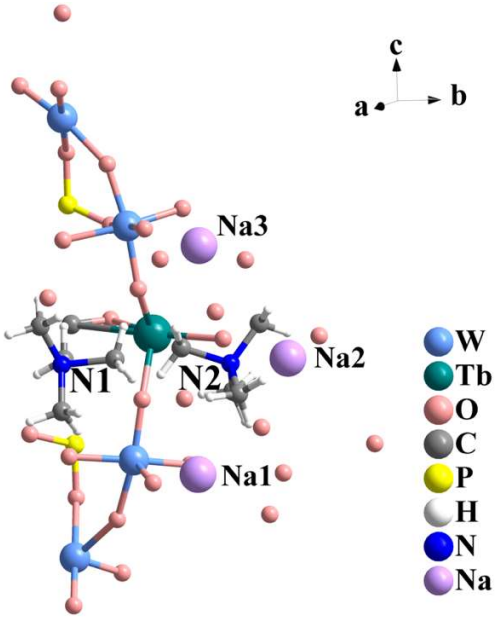

Figure 3-17. The asymmetric unit of crystal **4**.

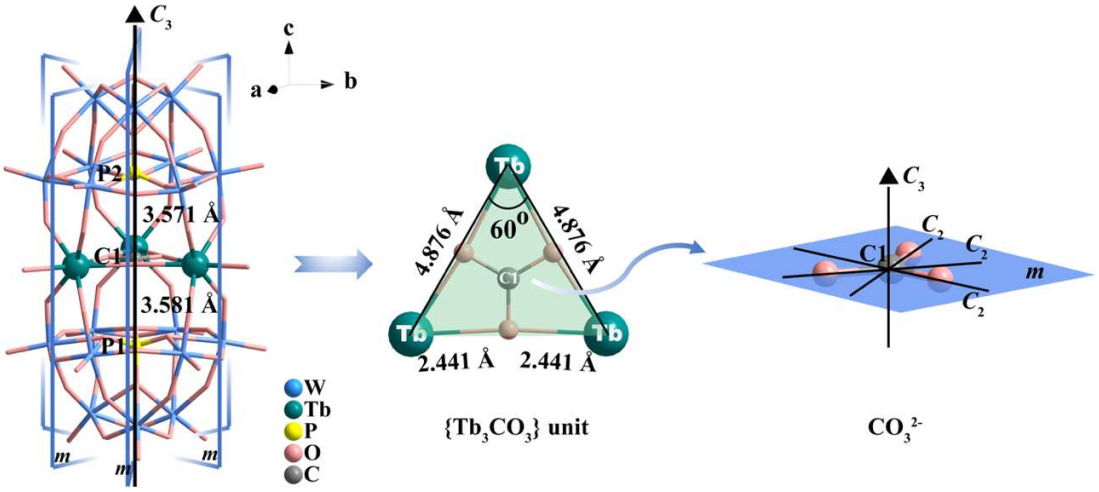

Figure 3-18. The structure of sandwich POM anion in crystal **4**. The equilateral triangle structure constructed by {$TbCO_3$} unit (Middle). The symmetry of CO_3^{2-} in {$TbCO_3$} unit (right).

Different from crystal **1**, the 3D framework of crystal **4** was constructed with sandwich POM anions as vertices and with Na^+ cations as linkers by electrostatic interaction, and TMA^+ cations as guest molecules accommodate in the framework. There is no strong hydrogen bonding interaction between sandwich POM anions. As shown in Figure 3-19a, each sandwich POM anion

is connected to six disordered $Na1^+$ ions, six disordered $Na2^+$ ions and six disordered $Na3^+$ ions, in which $Na1^+$ ions are arranged at one side of $\{Tb_3CO_3\}$ triangle plane and $Na2^+$ ions and $Na3^+$ ions are arranged at another side of $\{Tb_3CO_3\}$ triangle plane. Every sandwich POM anion is connected to three sandwich POM anions by six $Na1^+$ ions and three anions by six $Na3^+$ ions as shown in Figure 3-19b. Then six anions are in staggered arrangement due to the narrow shape of a sandwich POM anion. Further, sandwich POM anions assemble into three-dimensionally in a manner of cubic close packing with channel in a squashed style (Figure 3-19c and d). Along *c* axis, one $Na1^+$ ion, one $Na2^+$ ion and one $Na3^+$ ion are bridged by water molecules by strong electrostatic interaction as shown in Figure 3-19e, forming a twisted and rigid chain with repeat unit···Na1-H_2O-Na2-H_2O-Na3···. It can be noticed that two disordered $Na2^+$ ions are very close with an interatomic distance of 2.853 Å and one disordered water molecule with chemical occupancy of 2/3 for O atom exist between them. The channel was divided into compartments separated by "bamboo nodes" as a result of the penetration of $Na2^+$ ions and water molecules. Disordered TMA^+ (N1 and N2) cations were embedded in each of the compartments separated by the bamboo nodes.

The data of electrostatic interaction between Na^+ ions and water molecules, and the electrostatic interaction between Na^+ ions and sandwich POM anions are shown in Table 3-5. Disordered TMA^+ (N1 and N2) cations are accommodated in compartments, which is symmetric over one of mirror planes perpendicular to $\{Tb_3CO_3\}$ triangle plane. For TMA^+ (N1) cation, N1, C2 and C4 atoms are at the mirror plane, C3 and C5 atoms are disordered in two positions, which are symmetrical over the mirror plane. And for TMA^+ (N2) cation, N2 and C9 atoms are at the mirror plane, C6, C8 and C7 atoms are disordered in two positions, which are symmetrical over the mirror plane.

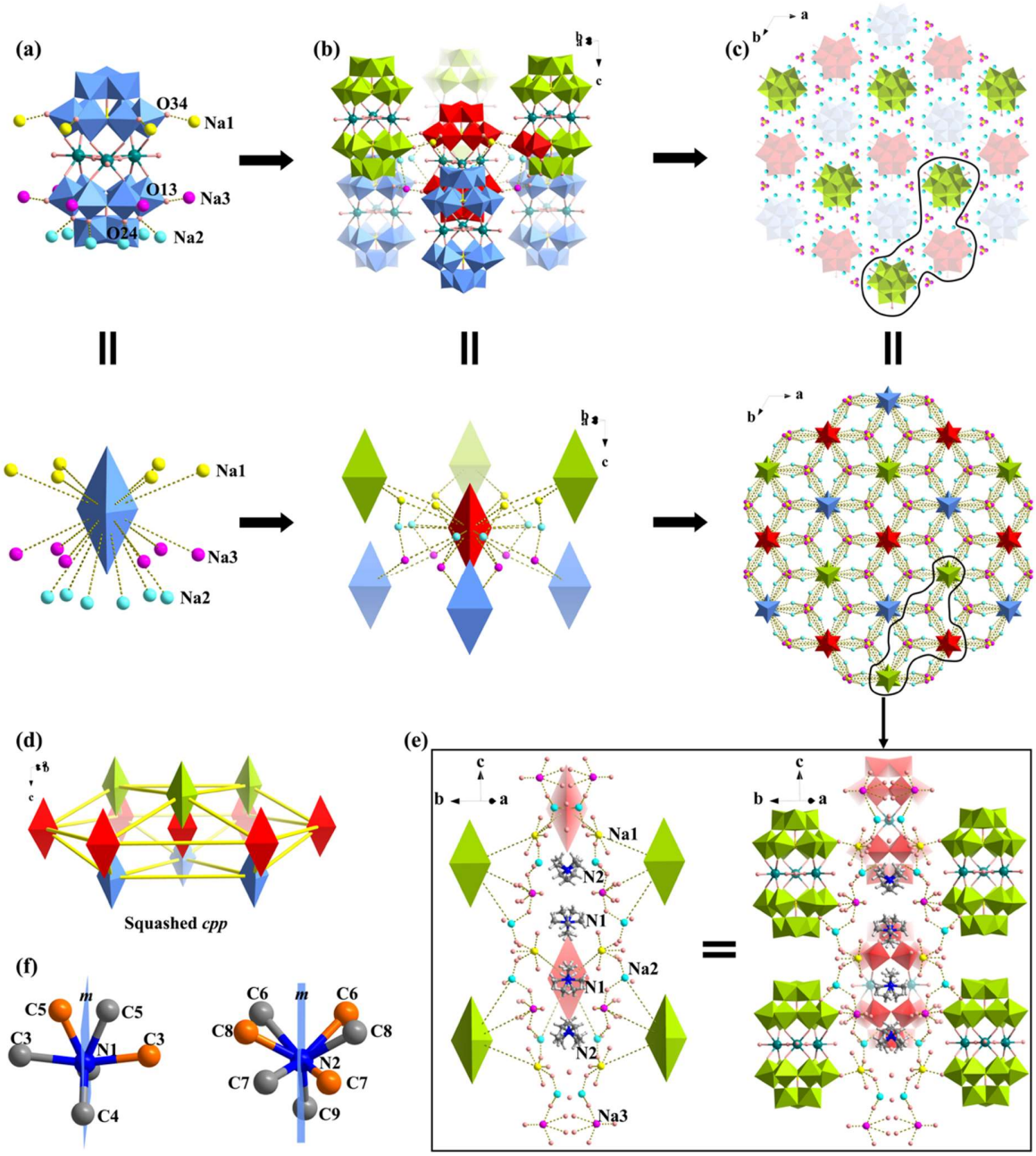

Figure 3-19. Single crystal structure of crystal **4**. (a) Sandwich POM anions as subunits are connected to 18 Na^+ ions as linkers by electrostatic interaction. The sandwich POM anion is abstracted as a triangular bipyramidal (bottom). (b) The sandwich POM anions are connected by Na^+ ions. (c) 3D framework structure of sandwich POM anions with channels along *c* axis. (d) The squashed *cpp* mode of sandwich POM anions packing. (e) The twist chains constructed of Na^+ ions and water molecules by electrostatic interaction. (f) The disorder structure of TMA^+ cations (N1 and N2) accommodating in the compartments separated by the bamboo nodes. The electrostatic interaction is shown in dark green dotted line.

Table 3-5. The data of electrostatic interaction between Na^+ ions and water molecules, and the electrostatic interaction between Na^+ ions and sandwich POM anions in crystal **4**.

Na···O(POMs/H_2O)	Distance/ Å
Na3···O13(POM)	2.135
Na2···O24(POM)	2.820
Na1···O34(POM)	2.465
Na1···O2(H_2O)	2.492
Na1···O2A(H_2O)	2.475
Na1···O5(H_2O)	2.309
Na2···O2(H_2O)	3.371
Na2···O3(H_2O)	2.513
Na2···O10(H_2O)	3.389
Na3···O3(H_2O)	2.336
Na3···O10(H_2O)	2.786
Na3···O18(H_2O)	2.120

3-7. Crystal structure of crystal 5.

X-ray diffraction data reveals that the crystals of **5**, $([H_2DABCO]^{2+})_6[(PW_9O_{34})_2(H_2OLn)_3CO_3][BF_4]\cdot 5H_2O$ (Ln = Tb, Dy and Er), were isomorphous, crystalizing in the highly symmetric hexagonal space group $P6_3/mcm$. The crystal structure of crystal **5-Er** will be discussed in detail for representation. Crystal **5-Er** consists of 1/3 sandwich POM anion, ¼ BF_4^- anions, 3 $[H_2DABCO]^{2+}$ cations and $3\frac{3}{4}$ water molecules within independent unit as shown in Figure 3-20. As shown in Figure 3-21, the structure of sandwich POM anion within crystal **5-Er** is also distorted as in the case of crystal **3**, with isosceles-type triangle $\{Er_3CO_3\}$ and Er···Er distances of 4.818 Å, 4.818 Å and 4.807 Å, where the D_{3h} symmetry of CO_3^{2-} ligand is lost. In addition, two mirror planes exist in crystal **5**, one coinciding with the Ln_3-triangle($\{Er_3CO_3\}$) plane and the other passing through the carbon atoms in the $\{Er_3CO_3\}$ perpendicular to the triangle plane. The P-C-P bonds between carbonate carbon and axial phosphorous atoms are distorted (<P1–C1–P1 = 179.38°). The sandwich POM anion doesn't exhibit C_3 symmetry although the whole crystal structure display highly symmetric structure with C_3 axis.

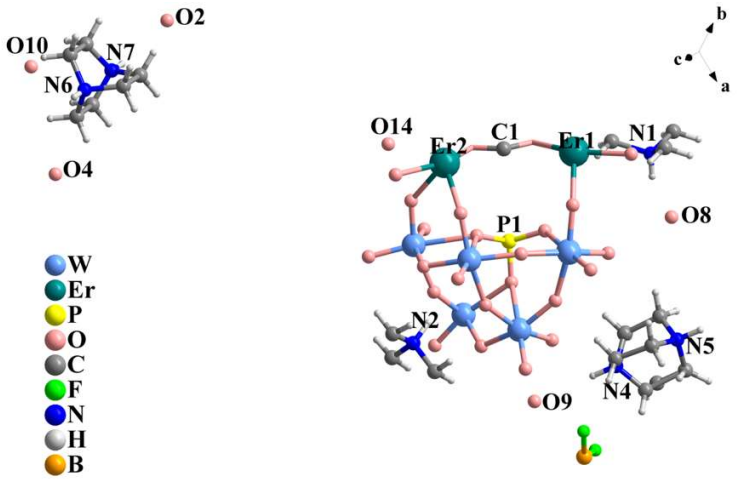

Figure 3-20. Th asymmetric unit of crystal **5-Er**.

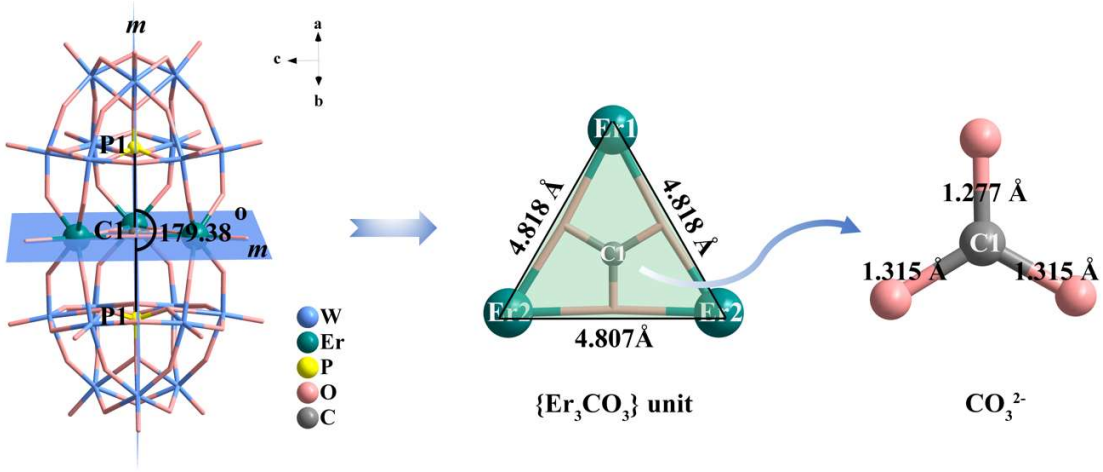

Figure 3-21. The structure of sandwich POM anion in crystal **5-Er**. The distorted triangle structure constructed by {$TbCO_3$} unit (Middle). The structure of CO_3^{2-} in {$TbCO_3$} unit (right).

The polymer framework of crystal **5** is constructed from sandwich POM anions and one ([N4, N5]) of four crystallographycally independent $[H_2DABCO]^{2+}$ cations ($[N1]_2$, $[N2]_2$, [N4, N5] and [N6, N7]) as linkers and with BF_4^- as vertices. And the other $[H_2DABCO]^{2+}$ cations ($[N1]_2$, $[N2]_2$ and [N6, N7]) and water molecules as guest molecules accommodate in the framework. As shown in Figure 3-22c, with a S_3 axis parallel with *c*-axis through B atom and F2 atom, three F3 atoms of each BF_4^- anion are connected to six disordered water molecules (O9) and another F2 atom is connected to three disordered $[H_2DABCO]^{2+}$ cations ([N4, N5)) by hydrogen-bond interaction, forming a chain ···O9···BF_4^-···$[H_2DABCO]^{2+}$···BF_4^-···O9···. Then, each $[H_2DABCO]^{2+}$ cation ([N4,

N5)) is connected one sandwich POM anion, forming 3-dimensional packing structure with a channel of 21.29 Å by hydrogen bonding interaction, in which $[H_2DABCO]^{2+}$ cations of [N6, N7] and water molecules accommodate (Figure 3-22, Figure 3-23a). A S_3 axis through the center of the channel can be observed. $[H_2DABCO]^{2+}$ cations of $[N1]_2$ and $[N2]_2$ filled the space between two neighboring sandwich POM anions as shown in Figure 3-23b-d. In crystal 5-Er, highly symmetric of $[H_2DABCO]^{2+}$ (D_{3h}) cations with two hydrogen-bond sites are used as counter cations, which isn't suitable for forming structure with C_3 symmetry. But $[H_2DABCO]^{2+}$ cations can be used as a node to construct structure with C_3 symmetry because the two hydrogen-bond sites are at the C_3 axis, which is similar with cylinder. Therefore, at the existence of highly symmetric BF_4^- anions (T_d) with the strongly negative F atoms, $[H_2DABCO]^{2+}$ cations and water molecules acting as nodes, the chain possessing S_3 symmetry was constructed. Furthermore, the symmetry of the whole structure is mainly controlled by the symmetry of the chain built of BF_4^- anions (T_d) connected by nodes.

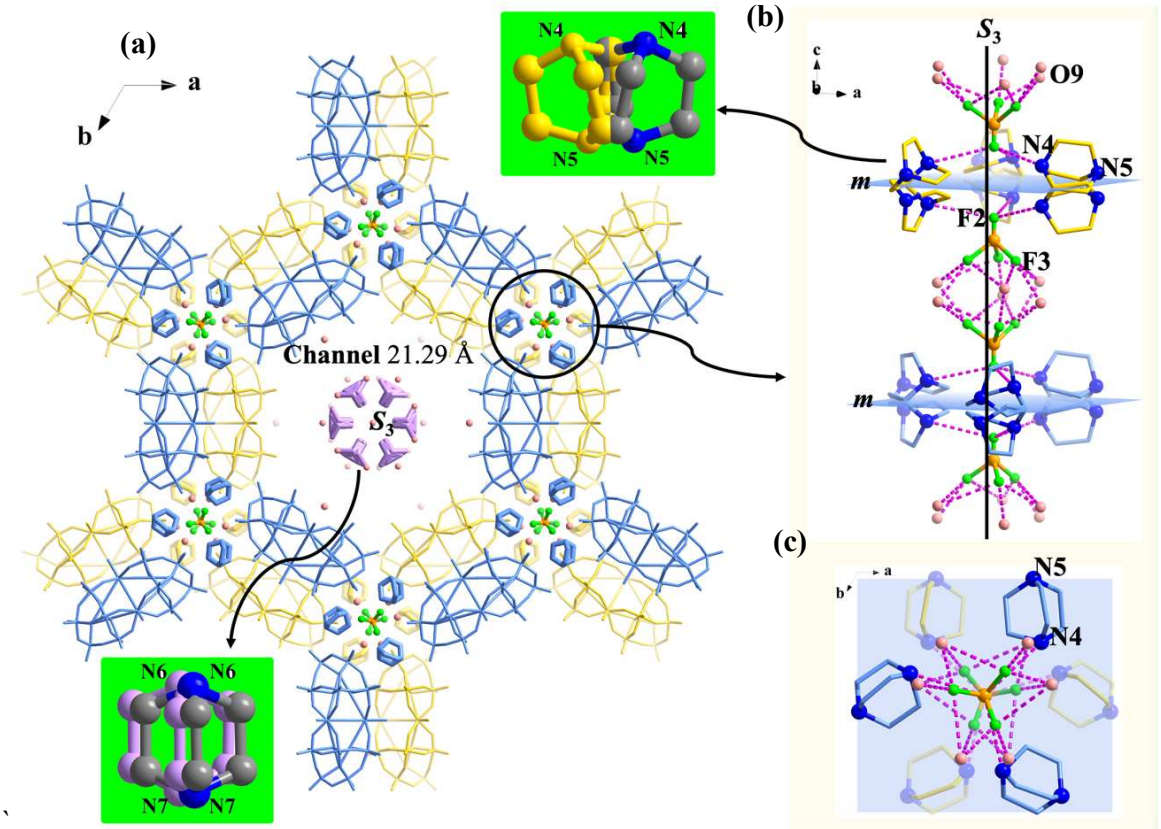

Figure 3-22. (a) The packing structure of crystal 5-Er. The structure of the chain built of BF_4^- anions, $[H_2DABCO]^{2+}$ (N4, N5) cations (shown in blue and gold) and water molecules by hydrogen-bond interaction (···O9···BF_4^-···$[H_2DABCO]^{2+}$··· BF_4^-···O9···) along *b* (b) and *c* (c) axis. The sandwich POM anions at neighboring layers along c axis are shown in blue and gold stick mode. $[H_2DABCO]^{2+}$ cations (N4 and N5) that are at the same layer with sandwich POM anions are shown in blue and gold color ball and stick mode. $[H_2DABCO]^{2+}$ (N6, N7) cations accommodating in the channel are shown in lavender are shown in in lavender ball and stick mode. Water molecules are shown in pink. Hydrogen atoms are omitted for clarity.

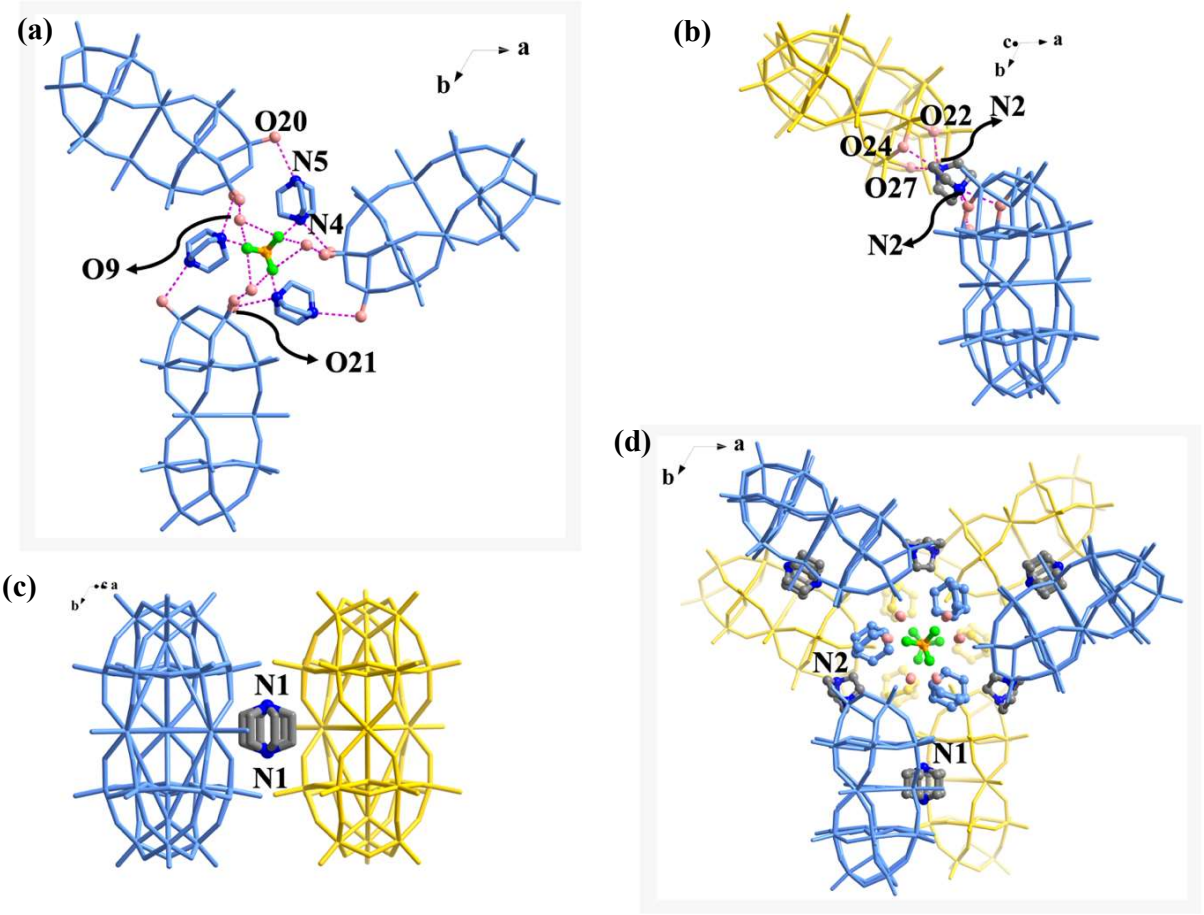

Figure 3-23. (a) The hydrogen bonding interaction between sandwich POM anions and the chain showed in Figure 3-22b and c. (b) (c) (d) The arrangement of $[H_2DABCO]^{2+}$ cations of N1and N2 within the crystal **5-Er**. Hydrogen atoms are omitted for clarity. N: blue; C: dark gray; O: pink.

Table 3-6. The data of hydrogen bonding between $[H_2DABCO]^{2+}$ cations and sandwich POM anions or BF_4^- anions and hydrogen-bond between water molecules and BF_4^- anions in crystal **5-Er**.

Hydrogen bonding units	Distance/ Å	Angle/^{o}
N2-H···O27(POM)	3.078	134.48
N2-H···O22(POM)	3.014	133.61
N2-H···O24(POM)	2.871	128.89
N4-H···F2(BF_4^-)	3.227	110.488
N4-H···O21(POM)	3.136	121.614
N5-H···O20(POM)	3.290	155.039
N6-H···O10(H_2O)	3.152	130.64
N6-H···O2(H_2O)	3.221	135.28
O9(H_2O)···F3(BF_4^-)	2.262	
O9(H_2O)···F3(BF_4^-)	3.032	
O9(H_2O)···O1(POM)	2.383	
O14(H_2O)···O29(POM)	3.141	
O8(H_2O)···O25(POM)	3.026	
O8(H_2O)···O26(POM)	2.766	

3-8. Discussion of crystal structures.

Three kinds of highly centrosymmetric space groups of $P6_3/m$, $R\bar{3}m$ and $P6_3/mcm$ in crystal **1**, **4** and **5** were achieved, respectively. Two polar space groups of $Pna2_1$ and $Cmc2_1$, were obtained in crystals **2** and **3**, respectively.

Ideal lacunary Keggin α-A-POM possesses symmetry of C_{3v}, which is readily distorted and affected by cations and solvent molecules in solution. Although, an ideal sandwich POM anion should display D_{3h} symmetry, in which the Ln_3-triangle is equilateral having C_3 axis perpendicular to the plane. In this work, not only $MA^+(C_{\infty v})$, $DMA^+(C_{2v})$, $TriMA^+(C_{3v})$ and $TMA^+(T_d)$ cation possessing 3, 2, 1 and 0 hydrogen-bond sites but also $[H_2DABCO]^{2+}$ (D_{3d}) with two hydrogen-bond sites and BF_4^- anions (T_d) both possessing high symmetry are exploited, in which MA^+ cations constructed hydrogen bonding network of C_3 symmetry with the sandwich POM anions and water molecules utilizing three hydrogen-bonding sites at $-NH_3^+$ moiety. And BF_4^- anions

constructed hydrogen bonding network of S_3 symmetry with sandwich POM anions, $[H_2DABCO]^{2+}$ cations and water molecules.

In the crystal **1**, Hydrogen bonding supramolecular units ($\{(MeNH_3^+)_x(H_2O)_y\}$ having C_{3h} symmetry and compatible size with sandwich POM anions are formed due to the $C_{\infty v}$ symmetry and three hydrogen bond sites of MA^+ cation. The POM network was formed with another crystallographically independent MA^+ (N2) different from those forming supramolecular units (N1 and N3). The C_{3h} symmetry of the POM was maintained even in the crystal embedding supramolecular units of C_{3h} symmetry in the cage and channel of the POM network, resulting in a highly symmetric space group $P6_3/m$ of crystal **1**.

For crystal **4**, sandwich POM anions are connected by Na^+ ions. Since the interaction with Na^+ is essentially electrostatic and isotropic and the templating effect of the highly symmetric structure (T_d) of TMA^+ cations, POMs packed in a squashed cubic closest packing style, leading to highly symmetric $R\bar{3}m$ space group. And the C_{3v} symmetry was maintained with sandwich POM anions. The channel within the network are filled with TMA^+ and H_2O molecules, whose assembly structure suited to the symmetry of POM network. Sandwich POM anion doesn't keep the ideal symmetry D_{3h} but adopt C_{3v} symmetry. It can be attributed to squashed cubic closest packing style adopted by crystal **4**. The POMs have taken the narrow shape due the electrostatic interaction with Na^+ to suit in the squashed cubic closest packing.

Crystals **2** and **3** take polar space groups of $Pna2_1$ and $Cmc2_1$, respectively. In crystal **2**, sandwich POM anions are linked by DMA^+ cations (C_{2v}) with only two hydrogen bond sites by hydrogen-bond interaction. It is difficult to keep C_3 symmetry fulfilling the crystal packing with lower symmetry of DMA^+ cations having two hydrogen bond sites. In crystal **3**, sandwich POM anions are connected by Na^+ not by $TriMA^+$ cations. Due to the influence of $TriMA^+$ cations through hydrogen bond interaction, C_3 axis of $TriMA^+$ cations aren't parallel with that of POM. In addition, compared with ideal sandwich POM anions, $TriMA^+$ cations have a lower symmetry. As a result, only a σ_v mirror plane is kept in the crystal **3**, giving rise to a polar $Cmc2_1$ space group.

Different from crystals **1**, **2**, **3** and **4**, in crystal **5**, not only $[H_2DABCO]^{2+}$ (D_{3h}) cations but also BF_4^- (T_d) anions with high symmetry are introduced. The BF_4^- anions (T_d) possess same symmetry with TMA^+ cations(T_d) in crystal **4**, while the TMA^+ cations don't have the ability of forming strong directional hydrogen bond. Within crystal **5**, the highly symmetric BF_4^- anions (T_d) with the

strongly negative F atoms lead the formation of highly symmetric hydrogen bonding nets structure with distorted sandwich POM anions, highly symmetric $[H_2DABCO]^{2+}$ cations and water molecules as nodes, resulting a highly centrosymmetric $P6_3/mcm$ space group.

Finally, the equilateral triangle motifs composed of three Ln^{3+} ions bridged by one carbonate ligand are achieved in **1** and **4** under the effects of highly symmetric supramolecular units $\{(MeNH_3^+)_2(H_2O)_x\}$ (C_{3h}) and TMA^+ (T_d) cations, respectively.

3-9. IR spectra

The IR spectra of crystals **1, 2, 3, 4** and **5** are shown in the Figure 3-24. A characteristic band in all the compounds is around 1470 cm^{-1}, which is assigned to coordinated CO_3^{2-} stretch. A stretching vibration of C-N bond around 1425 cm^{-1} can be found, indicating the existence of organic cations in crystals **1**, **2**, **3** and **4** (Figure 3-24 a and b). For crystals **5**, the peaks appearing at 1010, 888, and 780 cm^{-1} can be attributed to BF_4^- stretching vibrations. The peaks in the ranges 1210-1620 cm^{-1} and 2700-3200 cm^{-1} are associated with the peaks of $[H_2DABCO]^{2+}$ cation. That indicate the existence of H_2DABCO^{2+} cations and BF_4^- anions in crystals **5**.

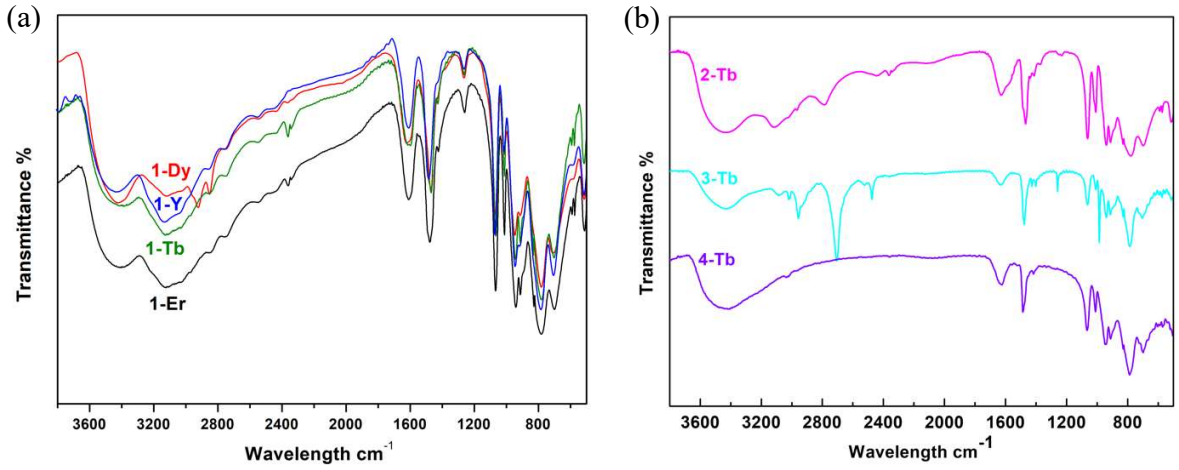

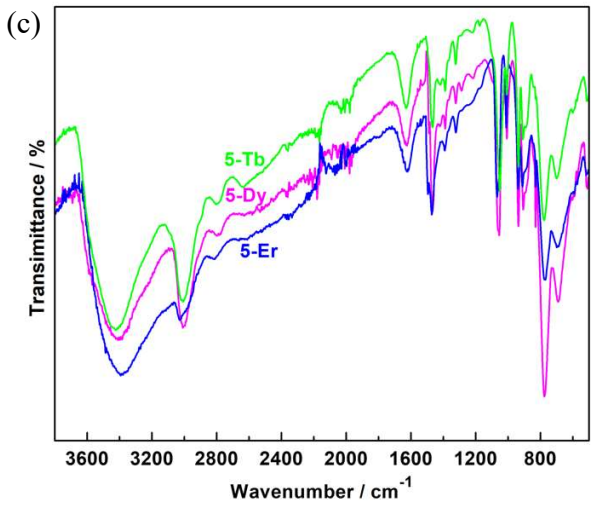

Figure 3-24. The IR spectra of crystals **1, 2, 3, 4** and **5**.

3-10. Power X-ray diffraction analysis

The purity of crystalline powders of compounds **1, 2, 3, 4** and **5** was confirmed by powder X-ray diffraction (PXRD), which is shown in Figure 3-25. The experimental patterns of **1, 2, 3, 4** and **5** are in accord with the corresponding simulated patterns derived from the single crystal data, indicating the presence of mainly one crystalline phase.

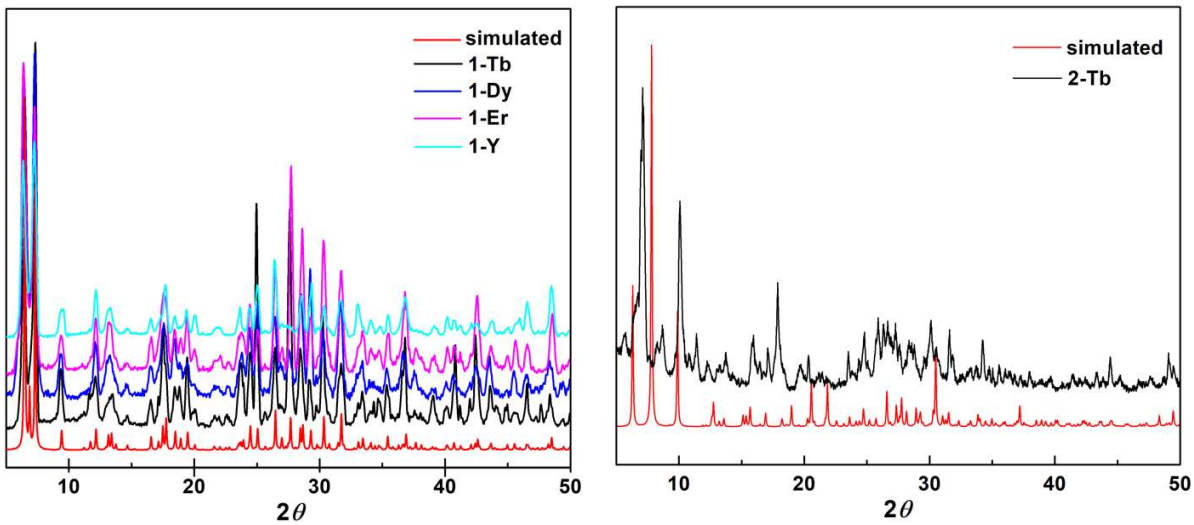

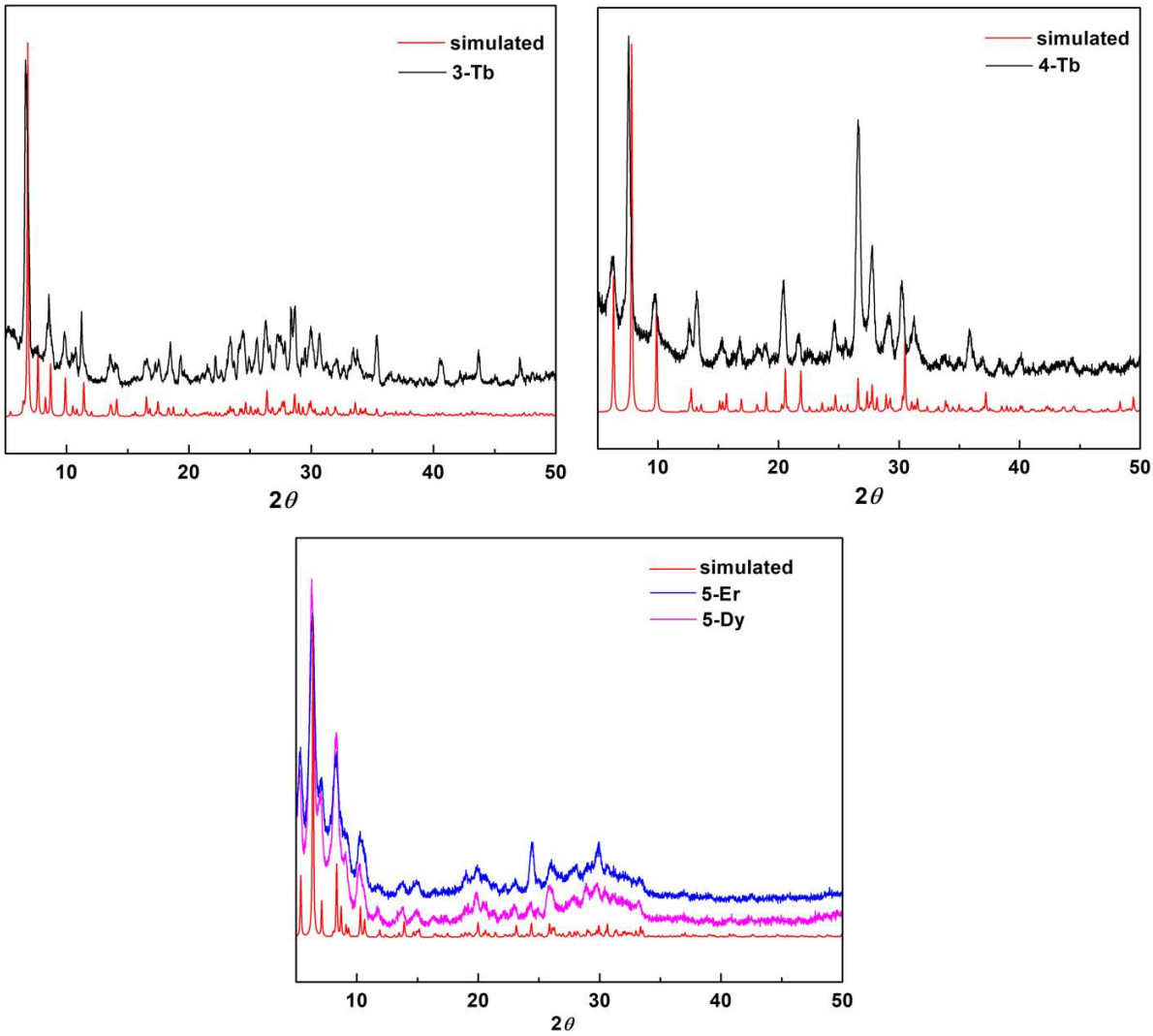

Figure 3-25 PXRD patterns of crystals **1, 2, 3, 4** and **5**.

3-11. Thermogravimetric analysis

As shown in the Figure 3-26, the crystals **1** display a similar trend as the temperature increases since they are isomorphic. About 9% loss from 20 to 140 °C is consistent with the loss of solvent water molecules. Then, from 140 °C, the methylammonium cation start decomposition until 400 °C, almost 6% loss is in accordance with the theory value. Subsequently, approximately 1% loss in the range of 640 to 750 °C can be observed, which is attributed to the decomposition of carbonate in the POM. For crystal **2**, the loss of about 7.5% from 20 to 140 °C is consistent with the loss of 26 water molecules and about 8.5% loss is corresponding to the decomposition of eleven DMA^+ cations from 140 to 400 °C. For crystal **3**, about 9 % loss from 200 to 450 °C is consistent with the

decomposition of eight $TriMA^+$ cations. About 7.5% loss from 300 to 500 °C is in accord with the loss of five TMA^+ cations in crystal **4**. In crystal **5**, the 13% loss of $[H_2DABCO]^+$ cations from 300 to 750 °C can be observed, which is consistent with the theory value.

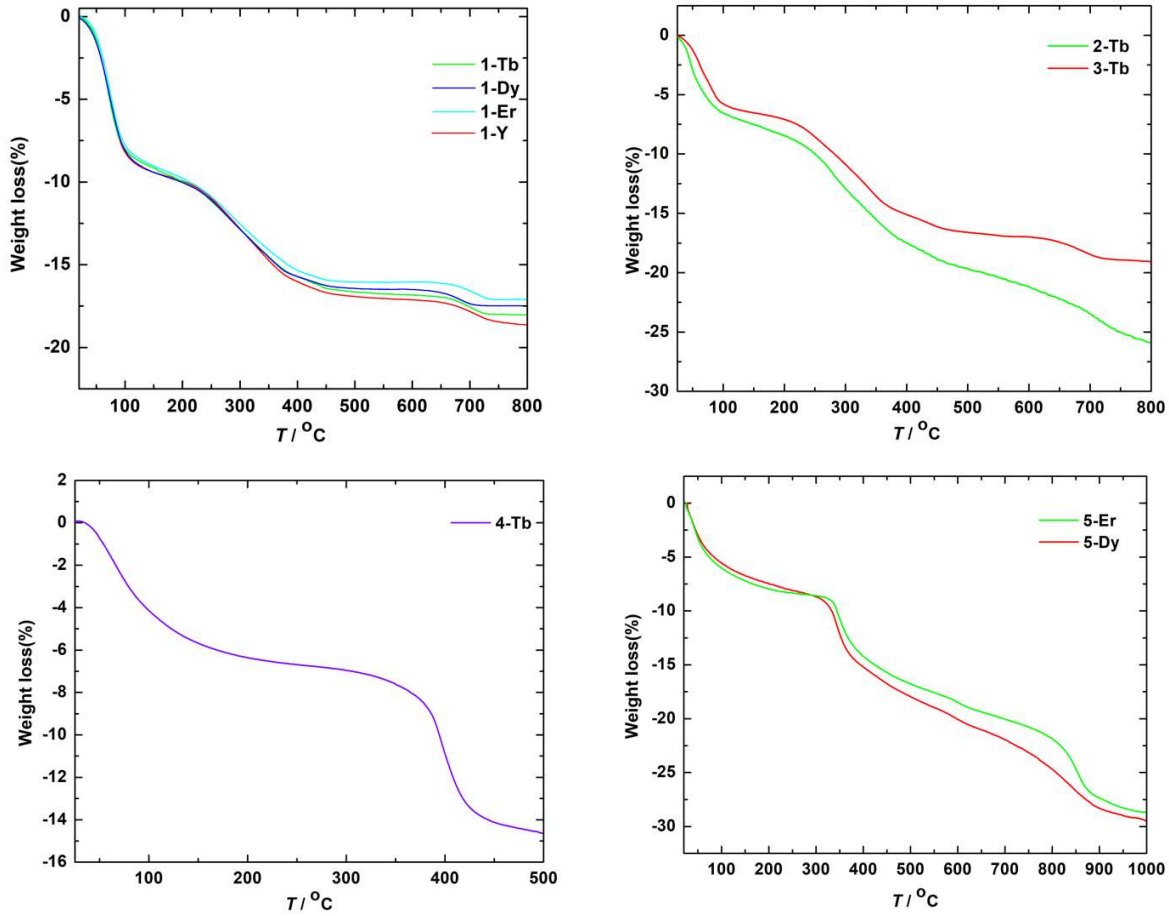

Figure 3-26. Thermogravimetric analysis of crystals **1, 2, 3, 4** and **5.**

3-12. Crystallographic data of the crystals 1, 2, 3, 4 and 5.

Table 3-7. Crystallographic and structure refinements for crystals **1**.

Compound	**1-Tb**	**1-Dy**	**1-Er**	**1-Y**
Formula	$C_{11}H_{86}Tb_3N_{10}NaO_{84}P_2W_{18}$	$C_{11}H_{92}Dy_3N_{10}NaO_{87}P_2W_{18}$	$C_{11}H_{82}Er_3N_{10}NaO_{83}P_2W_{18}$	$C_{11}H_{83}Y_3N_{10}NaO_{82.5}P_2W_{18}$
fw/g mol^{-1}	5573.65	5638.42	5578.62	5336.55
cryst syst	hexagonal	hexagonal	hexagonal	hexagonal
space group	*P*6$_3$/*m*	*P*6$_3$/*m*	*P*6$_3$/*m*	*P*6$_3$/*m*
a/Å	15.77430(10)	15.7767(3)	15.7833(5)	15.80568(8)
b/Å	15.77430(10)	15.7767(3)	15.7833(5)	15.80568(8)
c/Å	25.7532(2)	25.7856(5)	25.7635(6)	25.81439(11)
α/deg	90	90	90	90
β/deg	90	90	90	90
γ/deg	120	120	120	120
V/Å^3	5549.60(8)	5558.3(2)	5558.1(4)	5584.94(6)
Z	2	2	2	2
T/K	293	293	293	293
ρ_{calc}/g cm^{-3}	3.310	3.350	3.320	3.160
μ/mm^{-1}	43.765	45.144	38.516	36.349
F(000)	4856.0	4927.0	4874.0	4692.0
2*θ*/°	6.47 to 145.018	6.47 to 146.114	6.466 to 144.152	6.458 to 145.016
Reflections collected	19218	24228	19126	24101
Independent reflections	3725 [R_{int} = 0.0475]	3745 [R_{int} = 0.0779]	3682 [R_{int} = 0.0639]	3747 [R_{int} = 0.0371]
data/restraints/ param	3725/44/239	3745/90/250	3682/279/243	3747/52/241
R_{int}	0.0475	0.0779	0.0639	0.0371
R_1 [I > 2σ(I)]	0.0475	0.0584	0.0703	0.0321
wR_2 (all data)	0.1346	0.1671	0.1871	0.0902
GOF on F^2	1.080	1.089	1.072	1.138
$\Delta\rho_{max/min}$/e Å^{-3}	2.10/-2.56	3.53/-4.00	3.42/-3.33	1.87/-1.53

Table 3-8. Crystallographic and structure refinements for crystals **2**, **3** and **4**.

Compound	**2-Tb**	**3-Tb**	**4-Tb**
Formula	$C_{23}H_{140}Tb_3N_{11}O_{97}P_2W_{18}$	$C_{25}H_{116}Tb_3N_8Na_3O_{89}P_2W_{18}$	$C_{25}H_{118}Tb_3N_6Na_5O_{94}P_2W_{18}$
fw/g mol^{-1}	5971.21	5870.00	5969.98
cryst syst	orthorhombic	orthorhombic	trigonal
space group	*Pna*2$_1$	*Cmc*2$_1$	*Rm*
a/Å	30.3799(3)	20.3011(4)	22.5757(3)
b/Å	17.2014(2)	27.3357(5)	22.5757(3)
c/Å	21.0389(3)	21.3208(4)	40.1916(5)
α/deg	90	90	90
β/deg	90	90	90
γ/deg	90	90	120
V/Å^3	10994.4(2)	11831.8(4)	17739.8(5)
Z	4	4	6
T/K	94(2)	94(2)	93.7(8)
ρ_{calc}/g cm^{-3}	3.576	3.277	3.326
μ/mm^{-1}	20.793	19.323	19.348
F(000)	10544.0	10356.0	15756.0
2*θ*/°	3.872 to 61.948°	4.566 to 61.624°	4.288 to 61.776
Reflections collected	60941	31621	61738
Independent reflections	23517 [R_{int} = 0.0181]	12431 [R_{int} = 0.0376]	5990 [R_{int} = 0.0347]
data/restraints/ param	23517/124/1403	12431/162/812	5990/122/376
R_{int}	0.0181	0.0376	0.0347
R_1 [I > 2σ(I)]	0.0261	0.0357	0.0380
wR_2 (all data)	0.0676	0.0959	0.0938
GOF on F^2	1.106	1.028	1.180
$\Delta\rho_{max/min}$/e Å^{-3}	1.72/-1.58	2.58/-1.81	1.94/-1.93

Table 3-9. Crystallographic and structure refinements for crystals **5**.

Compound	**5-Er**	**5-Dy**	**5-Tb**
Formula	$C_{37}N_{12}H_{100}BF_4Er_3O_{79}P_2W_{18}$	$C_{37}N_{12}H_{100}BF_4Dy_3O_{79}P_2W_{18}$	$C_{37}N_{12}H_{100}BF_4Tb_3O_{79}P_2W_{18}$
fw/g mol^{-1}	5936.87	5922.59	5911.87
cryst syst	hexagonal	hexagonal	hexagonal
space group	*P*6$_3$/*mcm*	*P*6$_3$/*mcm*	*P*6$_3$/*mcm*
a/Å	37.8923(2)	38.1495(2)	38.0321(2)
b/Å	37.8923(2)	38.1495(2)	38.0321(2)
c/Å	20.2715(2)	20.3834(2)	20.3866(2)
α/deg	90	90	90
β/deg	90	90	90
γ/deg	120	120	120
V/Å^3	25206.8(4)	25691.2(4)	25537.4(3)
Z	9	9	9
T/K	94	94	94
ρ_{calc}/g cm^{-3}	2.307	3.355	2.057
μ/mm^{-1}	25.534	43.939	28.444
F(000)	15271.0	22626.0	12974.0
2*θ*/°	6.386 to 145.55	4.632 to 145.136	4.64 to 144.84
Reflections collected	104412	97375	105793
Independent reflections	8813 [R_{int} = 0.0660]	8951 [R_{int} = 0.0848]	8800 [R_{int} = 0.0980]
data/restraints/ param	8813/471/519	8951/0/256	8800/0/291
R_{int}	0.0660	0.0848	0.0980
R_1 [I > 2σ(I)]	0.0947	0.0802	0.0898
wR_2 (all data)	0.2767	0.2666	0.2751
$\Delta\rho_{max/min}$/e Å^{-3}	3.52/-2.17	6.37/-7.35	4.83/-6.76

3-13. Magnetic properties

3-13-1. Static magnetism.

Temperature dependence of molar magnetic susceptibilities (χ_m) of compounds **1, 2, 3, 4** and **5** on polycrystalline samples were measured in the temperature range of 1.8 – 300 K under an applied magnetic field of 1000 Oe (Figure 3-27). Susceptibility measured for crystal **1-Y** with non-magnetic Y cation were employed as the diamagnetic correction for the paramagnetic analogues. The $\chi_M T$ values 33.01, 36.87, 35.86 and 35.72 cm^3 K mol^{-1} for crystals **1-Tb**, **2-Tb**, **3-Tb** and **4-Tb** are consistent with the theoretical values for three free Tb^{3+} ions 35.46 (Tb, $^7F_6$). The $\chi_M T$ values 43.04 and 32.12 cm^3 K mol^{-1} for crystals **1-Dy** and **1-Er** at room temperature are consistent with the theoretical values for three free Ln^{3+} ions 42.51 (Dy, $^6H_{15/2}$) and 34.44 (Er, $^4I_{15/2}$), respectively.

Upon cooling, the $\chi_M T$ values of all the crystals were almost constant above 100 K and then decreased with decreasing temperature. The $\chi_M T$ values decrease rapidly below 50 K, reaching 20.95, 15.62, 17.76, 23.14, 21.97 and 22.42 cm^3 K mol^{-1} at 2.0 K, for crystals **1, 2, 3, 4** and **5**, respectively. The decline of $\chi_M T$ values at lower temperatures should be due to the decrease occupancy of the excited Stark sublevels of the Ln^{3+} ions and/or the antiferromagnetic interaction of the paramagnetic ion in the system.[146] The behavior apparently is different from the Dy_3-triangle complexes reported by Powell group, in which the vanishing susceptibility at low T was observed due to the toroidal arrangement of magnetic moments on the dysprosium sites.[147]

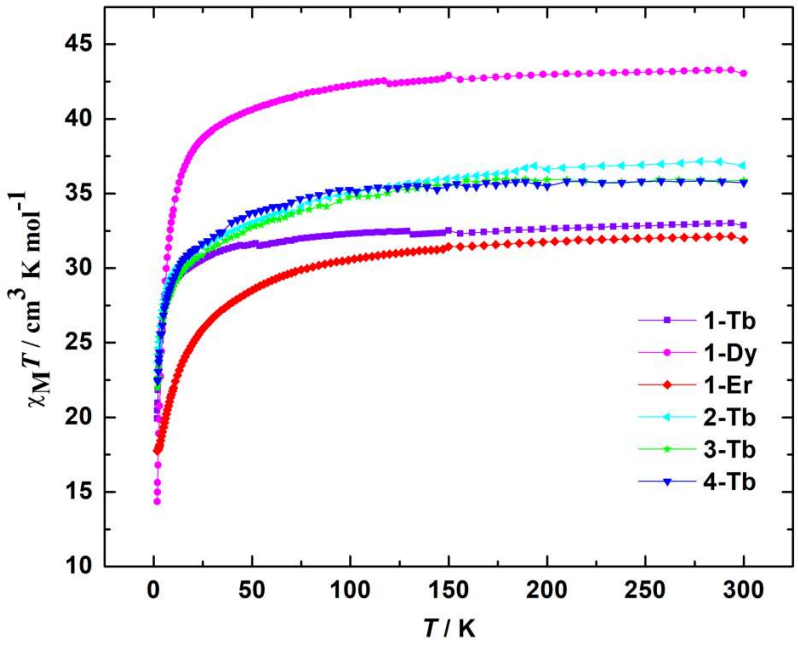

Figure 3-27. Plots of magnetic susceptibility ($\chi_M T$) *vs* temperature (T) for compounds **1-Ln**, **2-Tb**, **3-Tb**, and **4-Tb**, respectively.

3-13-2. Dynamic magnetic properties.

In order to investigate the magnetic dynamics of compounds **1-Ln**, **2-Tb**, **3-Tb** and **4-Tb,** the temperature dependencies of the alternating current (*ac*) susceptibility were measured with an oscillating 3 Oe *ac* magnetic field under 0 – 4000 Oe *dc* field. Under zero *dc* field, in the range of 1.8 – 10 K, the crystal **1-Tb**, **2-Tb**, **3-Tb** and **4-Tb** did not show any signal of frequency-dependence in both in-phase(χ') and out-of-phase(χ'') plots (Figure 3-28).

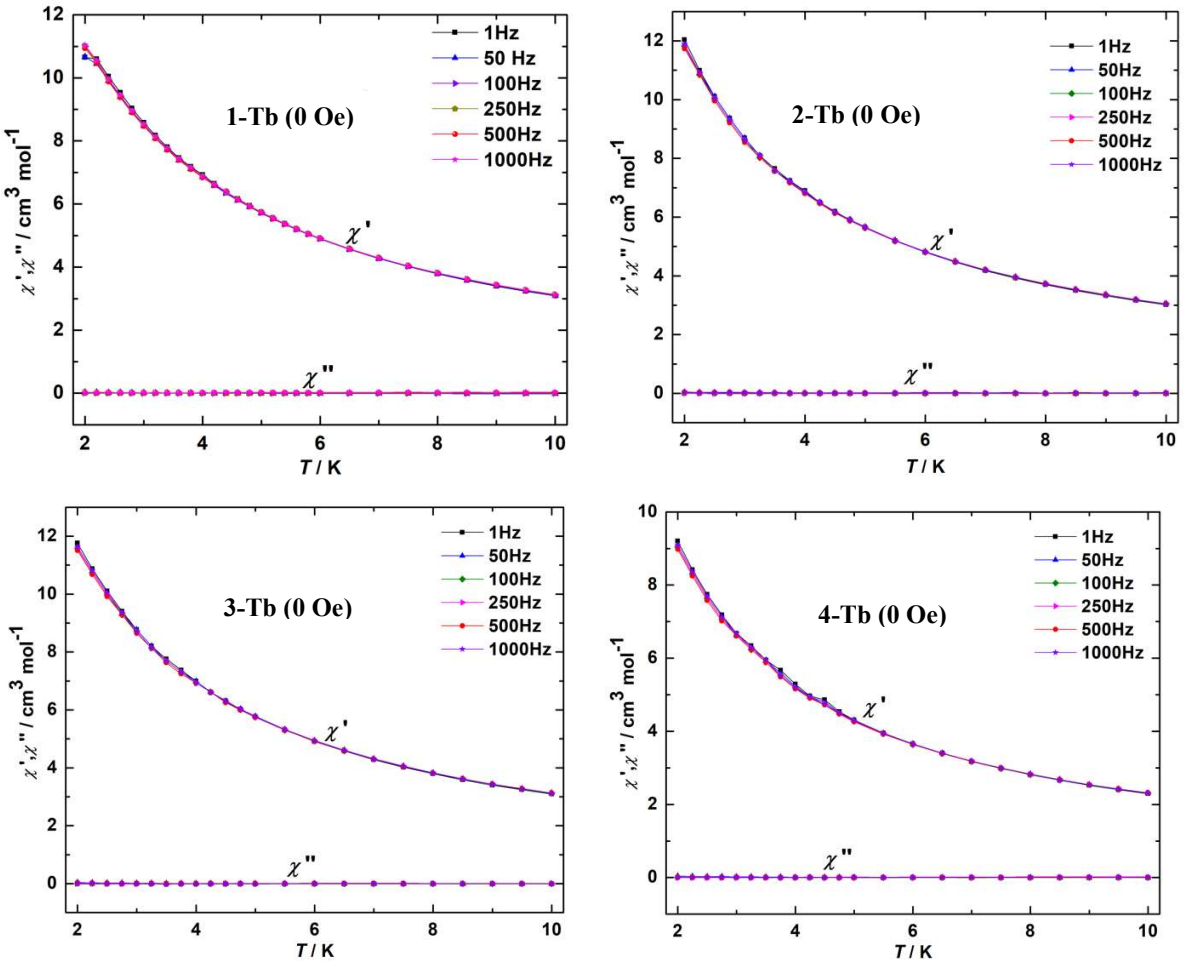

Figure 3-28. Temperature dependence of χ' and χ'' signals of the *ac* susceptibilities under different frequency (Hz) for crystal **1-Tb**, **2-Tb**, **3-Tb** and **4-Tb**, in zero static field and an oscillating field of 3 Oe.

The application of a *dc* field may fully or partly remove the ground state degeneracy and suppress the quantum tunneling.[148,149] The scale of applied *dc* field was determined by measuring susceptibilities at 2, 3 and 4 K, in static field from 0–10000 Oe and an oscillating field of 3 Oe. As shown on Figure 3-29, the out-of-phase susceptibilities (χ'') of crystals **1-Tb**, **1-Dy**, **1-Er**, **2-Tb**, **3-Tb** and **4-Tb** at 2, 3 and 4 K all display peaks at *dc* fields of 4000, 3000, 2000, 3000, 4000 and 5000 Oe, respectively.

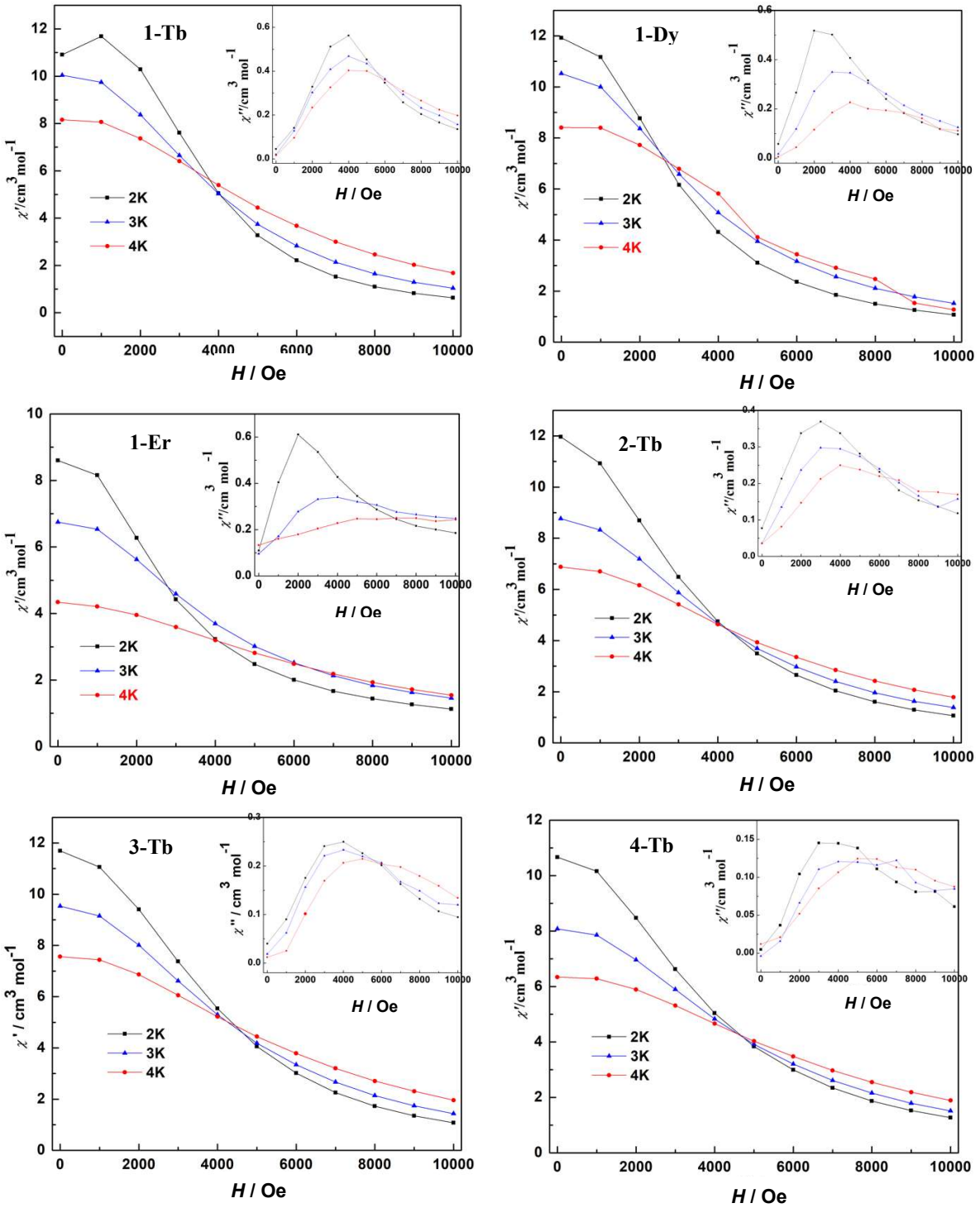

Figure 3-29. Field dependence of χ' and χ'' signals of the *ac* susceptibilities under different temperature (2, 3 and 4 K) for **1-Tb** (a), **1-Dy** (b), **1-Er** (c), **2-Tb** (d), **3-Tb** (e) and **4-Tb** (f) in static field from 0–10000 Oe and an oscillating field of 3 Oe.

Therefore, the *ac* magnetic susceptibilities of compounds **1-Tb**, **1-Dy**, **1-Er**, **2-Tb**, **3-Tb** and **4-Tb** were measured under the applied magnetic field of 4000, 3000, 2000, 3000, 4000 and 5000 Oe, respectively (Figure 3-30). With applied *dc* field, all the crystals showed frequency dependence with obvious peaks, typical of slow relaxation of the magnetization and field induced single molecular magnetic behavior, which means quantum tunneling is suppressed effectively. Especially for crystals **1-Tb**, **1-Dy**, **1-Er** and **4-Tb**, two peaks more obvious can be observed, which means more than one relaxation process exist in these crystals, indicating the relaxation behaviors in equilateral systems are more prominent. This will be deeply studied in future.

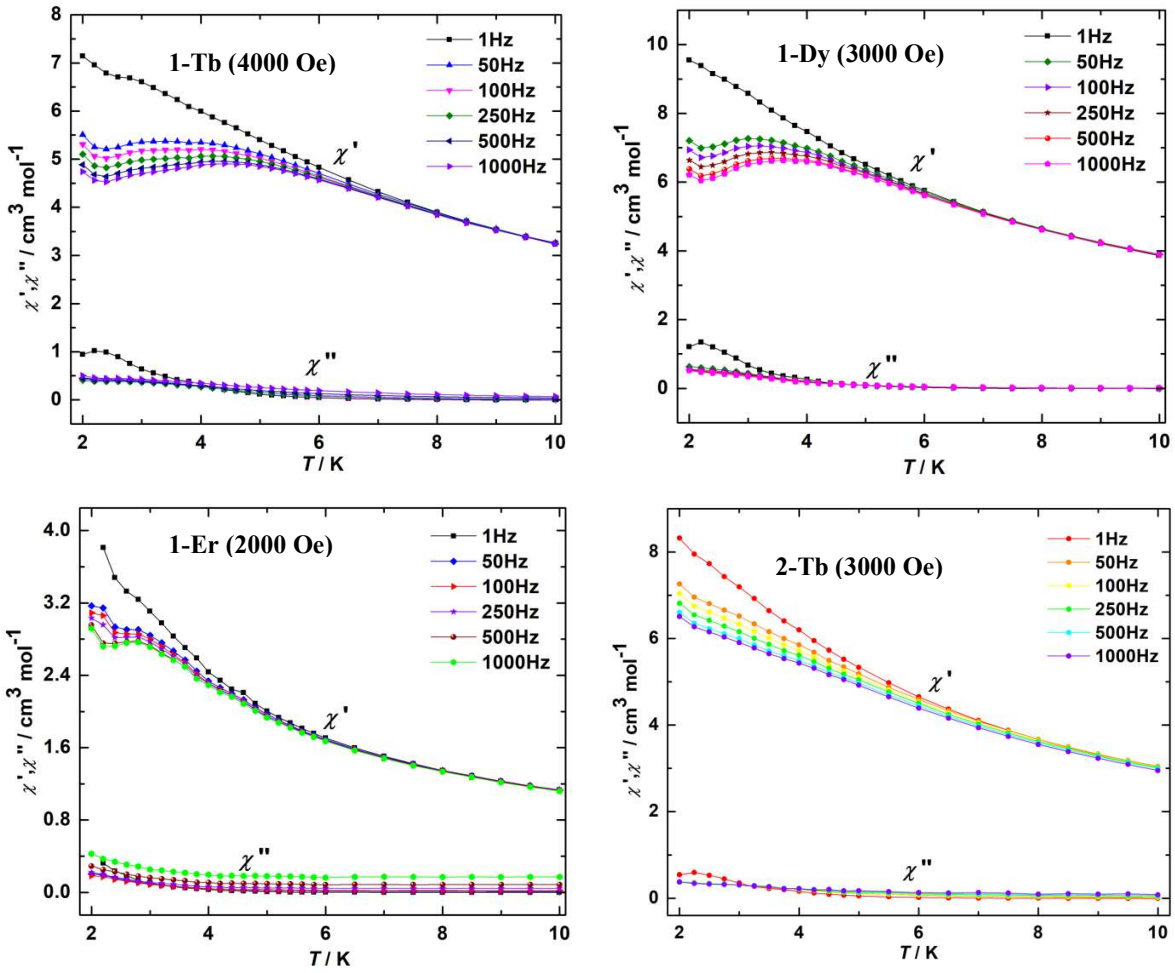

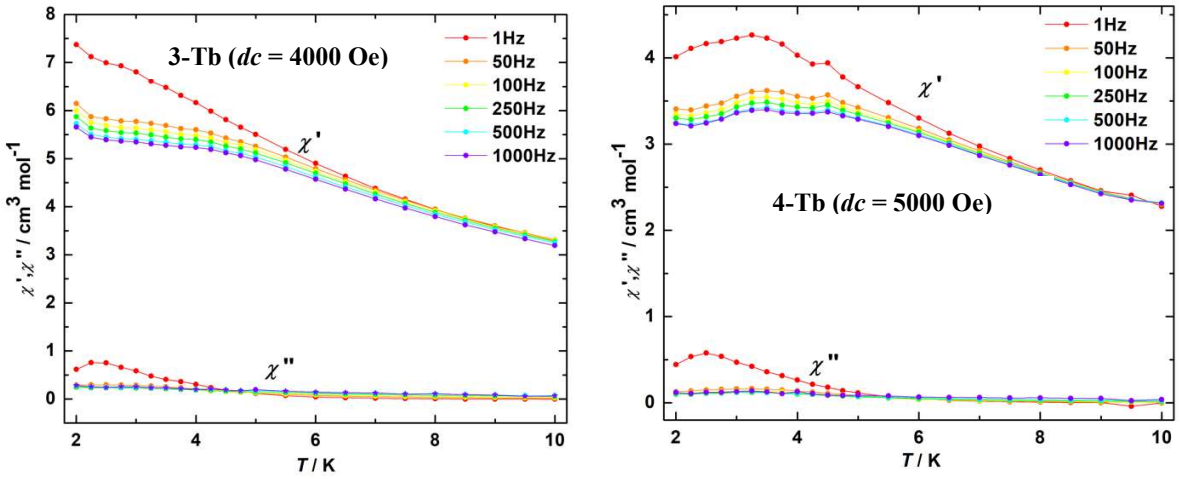

Figure 3-30. Temperature dependence of χ' and χ''signals of the *ac* susceptibilities under different frequency (Hz) for **1-Tb** (H_{dc} = 4000 Oe), **1-Dy** (H_{dc} = 3000 Oe), **1-Er** (H_{dc} = 2000 Oe), **2-Tb** (H_{dc} = 3000 Oe), **3-Tb** (H_{dc} = 4000 Oe) and **4-Tb** (H_{dc} = 5000 Oe) with an oscillating field of 3 Oe, respectively.

3-14. Conclusion

In this work, ten sandwich-type POMs $(CH_3)NH_3^+{}_{10}Na[(PW_9O_{34})_2(H_2OLn)_3CO_3]$ (**1**) (Ln = Tb, Dy, Er and Y, for **1-Tb**, **1-Dy**, **1-Er** and **1-Y**, respectively, MA = methylammonium), $(CH_3)_2NH_2^+{}_{11}[(PW_9O_{34})_2(H_2OTb)_3CO_3]$ (**2**) (DMA = dimethylammonium), $(CH_3)_3NH^+{}_8Na_3[(PW_9O_{34})_2(H_2OTb)_3CO_3]$ (**3**), (TriMA = trimethylammonium), $(CH_3)_4N^+{}_6Na_5[(PW_9O_{34})_2(H_2OTb)_3CO_3]$ (**4**), (TMA = tetramethylammonium), and $([H_2DABCO]^{2+})_6[(PW_9O_{34})_2(H_2OLn)_3CO_3][BF_4]$ (**5**) (Ln = Tb, Dy and Er for **5-Tb**, **5-Dy**,and **5-Er**, respectively), were obtained by introducing organic cations MA^+ ($C_{\infty v}$), DMA^+ (C_{2v}), $TriMA^+$ (C_{3v}) and TMA^+ (T_d), $[H_2DABCO]^{2+}$ (D_{3h}) and anion BF_4^- (T_d). Three kinds of highly centrosymmetric space groups of $P6_3/m$, $R\bar{3}m$ and $P6_3/mcm$ in crystal **1**, **4** and **5** were achieved, respectively. In crystals **1**, sandwich POM (C_{3h}) anions as vertices are connected by one(N1) of three crystallographically independent MA^+(N1, N2 and N3) cations, giving a highly symmetric 3D framework with cages and channels. In the cage and channel, two kinds of supramolecular units with C_{3h} symmetry as guest molecules accommodate, which were constructed by MA^+(N1 and N3) cations and water molecules through hydrogen bonding interaction to be compatible with sandwich POM (C_{3h}) anions in symmetry as well as size. In **4**, sandwich POM anions maintain C_{3v} symmetry under the templating effect of highly symmetric TMA^+ (T_d) cations. In **5**, the assembly

architecture of sandwich POM (C_{2v}) anions is leaded by highly symmetric BF_4^- (T_d) anions through hydrogen bonding interaction not the $[H_2DABCO]^{2+}$ (D_{3h}) cations. On the other hand, two polar space groups of $Pna2_1$ and $Cmc2_1$, were obtained in crystals **2** and **3**, respectively, due to the lower symmetry of DMA^+ and $TriMA^+$ cations and the number of hydrogen-bond sites of only two and one. Two or one hydrogen bond sites aren't easy of forming highly symmetric crystal structures by hydrogen bond net of C_3 symmetry, which is necessary for the formation of equilateral triangle of Ln^{3+} ions. Finally, the equilateral triangle motifs consist of three Ln^{3+} ions bridged by one carbonate ligand were successfully achieved in crystals **1** and **4**. What's more, the magnetic susceptibilities of crystals **1-Tb**, **1-Dy**, **1-Er**, **2**, **3** and **4** exhibit temperature-dependence at low temperature under the applied *dc* filed, typical of slow relaxation of the magnetization and field-induced single molecular magnetic behavior. It's worth noting that the magnetic relaxation in equilateral Ln_3-triangle is more prominent, which will be deeply studied in future.

Chapter IV

Fluoride-Bridged Dinuclear Lanthanoid Complexes Showing Single-molecule Magnetic Behavior: Supramolecular Approach to Isolate Magnetic Molecules

4-1. Introduction

Single-molecule magnets (SMMs) can be applied to ultra-high-density data storage,[150] quantum computing,[151] and spintronics[152] because of their nontrivial memory effect and quantum phenomena.[153–159] SMMs are molecule with energy barrier to spin reversal which induces magnetization without external magnetic field. This magnetization relaxes slowly in time at low temperature, resulting in a frequency dependence of the dynamic susceptibility. They are "molecule-sized permanent magnets" that exhibit magnetic hysteresis, although they have no magnetic long-range order. In order to observe this behaviour, a well isolated Ising ground state must be favored.[160] In other word, the ground state should consist of pure m_J state with the greatest value and a large energy barrier. The pure m_J state will prevent the quantum tunneling of the magnetization whereas the energy barrier will prevent the thermal relaxation.[161] In the case of lanthanides based SMM, the electronic configuration can be controlled by an adjustment of the coordination environment around the ions.[162] A large magnetic anisotropy appears as a result of the interaction between the orbital angular momentum component and ligand field potential. Therefore, the use of lanthanides enables the creation of SMMs with single ions (single-ion magnets (SIMs)).[161,163–168]

Because the magnetic properties of SMMs originate from a single molecule, the molecules of SMMs must be magnetically separated within the crystal.[115,169–171] Several approaches have been reported to achieve magnetic shielding between magnetic molecules, utilizing bulky lacunary polyoxometalates (POMs) as ligands.[172–176] For example, E. Coronado *et al.* reported that $[LnW_{10}O_{36}]^{9-}$ (Ln = Tb, Dy, Ho, and Er), in which lacunary POMs sandwich lanthanide ions, exhibit magnetic relaxation characteristic of SMMs.[177] Larger lacunary POMs can be used to construct lanthanide multinuclear complexes.[174] In particular, the diamagnetic ligands Keggin and Wells-Dawson type lacunary heterotungstates can sandwich and magnetically isolate multinuclear units, and a variety of lanthanoid multinuclear complexes have been synthesized.[173,174,176] For example, $(TBA)_{8.5}H_{1.5}[(PW_{11}O_{39})_2Dy_2X_2(H_2O)_2]\cdot 6H_2O$ (X = OH; F; OAc), in which the Dy dinuclear unit bridged by two F^-, OH^- or OAc^-, $Dy_2X_2(H_2O)_2$, is sandwiched by lacunary

Keggin, is reported.[178] Bridging ligands between lanthanides play an important role in SMM behavior. In these crystals, the fluoride- and hydroxyde-bridged complexes exhibit SMM behavior with U_{eff} = 98 and 74 cm^{-1}, respectively, while the acetate-bridged complex does not exhibit SMM behavior.

It is also possible to use counter cations to spatially isolate the complex to ensure SMM behavior. We previously showed that supramolecular structures comprising crown ethers and inorganic or organic ammonium cations exhibit large amplitude motions such as molecular rotation in crystals.[179–185] The cation is isolated from the counter anion to ensure space for molecular motion in the crystal. For example, in the crystal of (4,4'-bipyridinium)(dibenzo[24]crown-8)$[Ni(dmit)_2]^-$, where $dmit^{2-}$ = 1,3-dithio-2-thione-4,5-dithiolate, mono-protonated 4,4′-bipyridinium is connected via hydrogen bonds to form a pseudo polyrotaxane structure by penetrating dibenzo[24]crown-8.[186] One of the pyridine rings of 4,4'-bipyridinium exhibits rotational motion at about 293 K as a result of its isolation from the other molecules. Supramolecular cationic structures are also useful for isolating counter anions. In the case of Cs_2([18]crown-6)$_3[Ni(dmit)_2]^-_2$, [18]crown-6 rotates in the Cs_2([18]crown-6)$_3$ triple-decker structure.[185] The counter anion, $[Ni(dmit)_2]^-$, forms a dimer, which is completely isolated and surrounded by supramolecular cations.

In this study, we focused on dinuclear Ln complexes with a lacunary Keggin ligand.[187–189] To ensure the separation of the complexes, (Na)(B18C6) (B18C6 = benzo[18]crown-6) supramolecular cations were introduced into the crystal. Within the crystal, (Na)(B18C6) formed two types of tetramers via C-H•••O, π•••π and C-H•••π interactions, each of which was arranged in one dimension to form a bamboo-like channel structure. The fluoride-bridged Ln dinuclear complexes coordinated with two lacunary Keggin ligands and four H_2O molecules. {$[(PW_{11}O_{39})Ln(H_2O)_2]_2F$} ($Ln_2$POM, Ln = Tb, Dy and Er for **6-Tb**, 6-**Dy** and **6-Er**) was divided by a "bamboo node" and completely isolated from the neighboring complexes. The crystals **6-Dy** and **6-Er** exhibited the magnetic relaxation characteristics of an SMM at low temperatures.

4-2. Synthesis of crystals $[(Na)(B18C6)(H_2O)_{0.5}]_2[(Na)(B18C6)(H_2O)_{1.5}]_2[(Na)(B18C6)(H_2O)]_2[(Na)(B18$

C6)(H_2O)$_{1.75}$]$_2$[(($PW_{11}O_{39}$)Ln(H_2O)$_2$)$_2$F)][(Na)(B18C6)]$_2$(F)•12H_2O (6-Ln) (Ln = Tb, Dy and Er for 6-Tb, 6-Dy and 6-Er, respectively).

[(Na)(B18C6)(H_2O)$_{0.5}$]$_2$[(Na)(B18C6)(H_2O)$_{1.5}$]$_2$[(Na)(B18C6)(H_2O)]$_2$[(Na)(B18C6)(H_2O)$_{1.75}$]$_2$[(($PW_{11}O_{39}$)Dy(H_2O)$_2$)$_2$F)][(Na)(B18C6)]$_2$(F)•12H_2O (**6-Dy**) Solid $DyCl_3 \cdot 6H_2O$ was dissolved in 10 mL of H_2O during stirring, and a solution of Na_2CO_3 (1.00 M) was then slowly added, resulting in a pH level of 6.1. After the solution temperature reached 80 °C, $Na_8H[PW_9O_{34}]$ (1.0 g, 0.42 mmol) was added, and the mixture was stirred at 80 °C for 1 h. The solution was then cooled to room temperature and centrifuged to remove insoluble material. The aqueous solution containing B18C6 (400 mg, 1.28 mmol) and (*m*-fluoroanilinium$^+$)(BF_4^-) (120 mg, 0.6 mmol) was added to the clear solution and stirred for 4 h at room temperature. After filtration, the filtrate was maintained for 1 d, resulting in colorless block crystals. Yield: 46% (based on Dy). Anal. calcd for $C_{160}H_{296}Dy_2Na_{10}O_{166}F_2P_2W_{22}$ (%): C 20.07, H 3.12; found (%): C 21.01, H 3.06, where calculations were based on a composition assuming that the water molecules of the guest and the water coordinated to Na were desorbed during the experimental manipulation. Selected IR data (ATR, cm^{-1}): 3643(m), 3458(w), 3129(w), 2921(w), 2873(m), 2712(w), 2280(w), 2111(w), 1630(w), 1594(m), 1503(s), 1450(s), 1351(m), 1289(w), 1250(s), 1214(s), 1118(s), 1086(m), 1038(s), 943(s), 881(s), 806(s), 744(w), 690(w), 592(w).

[(Na)(B18C6)(H_2O)$_{0.5}$]$_2$[(Na)(B18C6)(H_2O)$_{1.5}$]$_2$[(Na)(B18C6)(H_2O)]$_2$[(Na)(B18C6)(H_2O)$_{1.75}$]$_2$[(($PW_{11}O_{39}$)Er(H_2O)$_2$)$_2$F)][(Na)(B18C6)]$_2$(F)•12H_2O (**6-Er**). Synthesized as crystal **6-Dy** except $DyCl_3 \cdot 6H_2O$ was replaced by $ErCl_3 \cdot 6H_2O$. Yield: 42% (based on Er). Anal. calcd for $C_{160}H_{296}Er_2Na_{10}O_{166}F_2P_2W_{22}$ (%): C 20.05, H 3.11; found (%): C 21.04, H 3.01. Selected IR data (KBr, cm^{-1}): 3627(m), 3461(m), 3170(w), 2913(w), 2881(m), 2745(w), 2295(w), 2119(w), 1634(w), 1585(m), 1503(s), 1455(s), 1352(m), 1293(w), 1252(s), 1211(s), 1115(s), 1080(m), 1039(s), 943(s), 877(s), 802(s), 747(w), 695(w), 595(w).

[(Na)(B18C6)(H_2O)$_{0.5}$]$_2$[(Na)(B18C6)(H_2O)$_{1.5}$]$_2$[(Na)(B18C6)(H_2O)]$_2$[(Na)(B18C6)(H_2O)$_{1.75}$]$_2$[(($PW_{11}O_{39}$)Tb(H_2O)$_2$)$_2$F)][(Na)(B18C6)]$_2$(F)•12H_2O (**6-Tb**). Synthesized as crystal **6-Dy** except $DyCl_3 \cdot 6H_2O$ was replaced by $TbCl_3 \cdot 6H_2O$. Yield: 42% (based on Tb). Anal. calcd for $C_{160}H_{296}Tb_2Na_{10}O_{166}F_2P_2W_{22}$ (%): C 20.08, H 3.12; found (%): C 21.44, H 3.11. Selected IR data (KBr, cm^{-1}): 3651(m), 3442(m), 3146(w), 2913(w), 2873(m), 2712(w), 2287(w), 2119(w),

1630(w), 1589(m), 1506(s), 1451(s), 1355(m), 1293(w), 1255(s), 1211(s), 1115(s), 1073(m), 1039(s), 940(s), 877(s), 802(s), 743(w), 695(w), 592(w).

4-3. Crystal structure of crystals 6.

X-ray diffraction data reveals that the crystals of **6-Ln**, $[(Na)(B18C6)(H_2O)_{0.5}]_2[(Na)(B18C6)(H_2O)_{1.5}]_2[(Na)(B18C6)(H_2O)]_2[(Na)(B18C6)(H_2O)_{1.75}]_2[((PW_{11}O_{39})Ln(H_2O)_2)_2F)][(Na)(B18C6)]_2(F)\bullet 12H_2O$ (Ln = Dy, Er and Tb) were isomorphous, crystalizing in triclinic, $P\text{-}\bar{1}$ space group. The crystal structure of crystal **6-Dy** will be discussed in detail for representation. Half of the Dy_2POM structure, four (Na)(B18C6) units coordinated by water molecules, $[(Na)(B18C6)(H_2O)_{1.75}]$, $[(Na)(B18C6)(H_2O)_{1.5}]$, $[(Na)_2(B18C6)_2(H_2O)]$ and $[(Na)_2(B18C6)_2(H_2O)_{0.5}]$, denoted as **A** – **D**, respectively, are crystallographically independent.

One water molecule with an occupancies of 0. 5 in **A**, two water molecules with an occupancy of 0.5 and 1 in **B**, one water molecule with an occupancy of 1 in **C**, and two water molecules with occupancies of 0.75 and 1.0 in **D**, respectively, were coordinated to Na^+ (Figure 4-1). In addition, six water molecules were isolated within the crystal as crystallographically independent guest molecules. Electron densities that could not be assigned to individual atoms were subtracted using the SQUEEZE function of the PLATON program.[190] The composition of the crystals was also determined from X-ray photoelectron spectroscopy (XPS). XPS measurements confirmed the presence of C, H, O, Dy, W, Na, and F atoms, but no B or N atoms were observed (Figure 4-11). The composition ratio of Na, P, and F was estimated to be 5 : 1 : 1 from SEM-EDX measurements (Figure 4-12 and Table 4-1), corresponding to the estimation about the number of (Na)(B18C6) and fluoride ion. Based on the elemental analyses and charge balance of the crystal, the two (Na)(B18C6) units and one fluoride ion should exist in the crystal in addition to the assigned molecules. The thermogravimetric analysis suggests that total number of the H_2O is approximately 28 (see Figure 4-10). The number of water molecules in the crystal **6-Dy** assigned by X-ray analysis is 25.5 per formula. There are about three H_2O molecules in the crystal that were not assigned by structural analysis. The electron density not assigned to individual atoms (224 e^-/mol) would consist of one (Na)(B18C6) unit (178 e^-/mol), one

fluoride ion (10 e^-/mol), and about three H_2O molecules (10 e^-/mol each). Since crystal **6-Dy** would not form without (*m*-fluoroanilinium$^+$)(BF_4^-), the source of the F atom, we conclude that the fluoride-bridged Dy dinuclear complex is present in the crystal.[191]

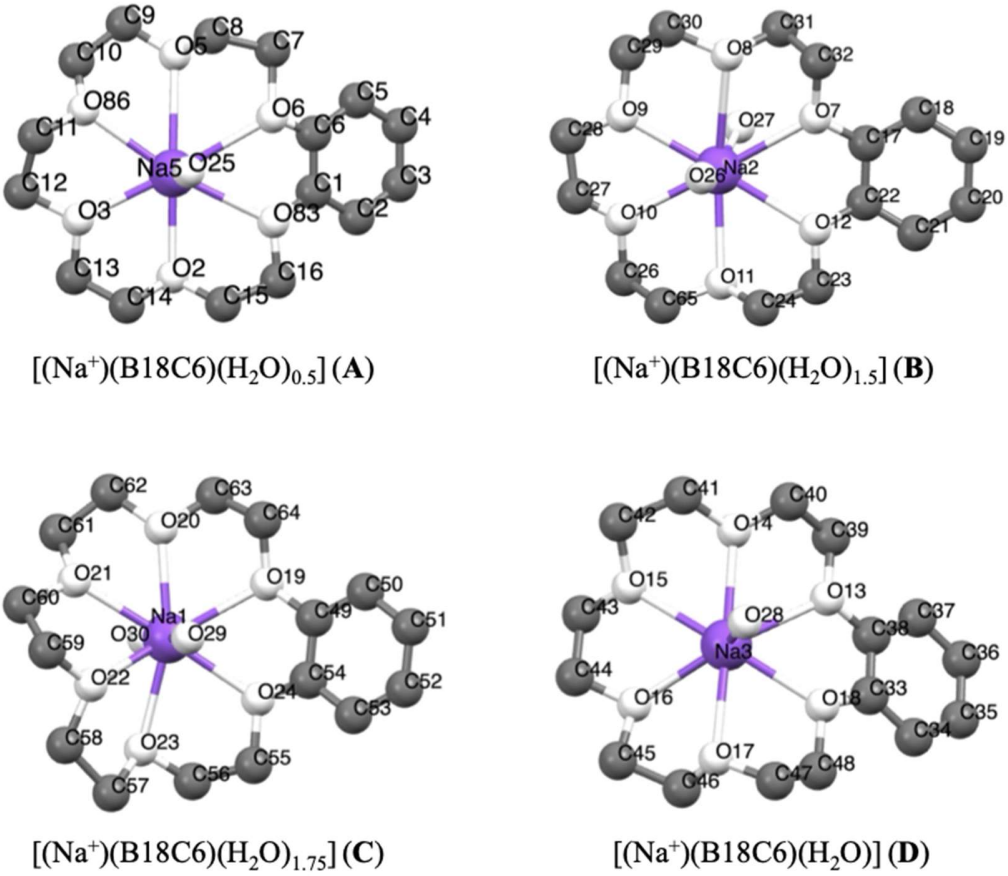

Figure 4-1. Crystallographically independent structure of (Na)(B18C6) units (**A**, **B**, **C**, and **D**) in crystal **6-Dy** at 94 K. Hydrogen atoms are omitted for clarity. Gray, white and purple atoms correspond to carbon, oxygen and sodium, respectively.

Figure 4-2 shows the structure of Dy_2POM. Lacunary POM ligand is disordered over two sites with the occupancy ratio of 0.556(8) : 0.444(8) (Figure 4-3). In Dy_2POM, four O atoms

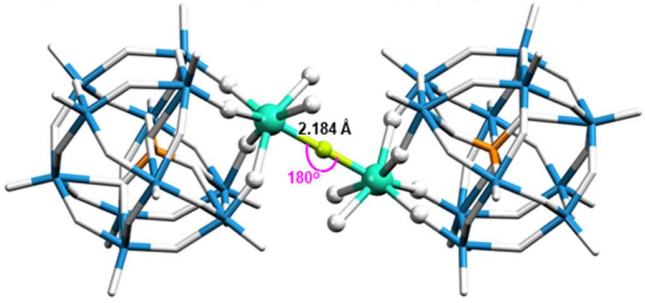

of the lacunary Keggin ligand, two O atoms of H_2O, and one F^- ion are coordinated to the Dy atom. The two Dy atoms are bridged by fluoride located at the symmetric center to form a dinuclear complex.

Figure 4-2. Structure of $\{[(PW_{11}O_{39})Dy(H_2O)_2]_2F\}$ in the crystal, with Dy-bridged fluoride at the symmetric center; Dy, O, W, F, and P are shown in green, white, blue, yellowish-green and orange, respectively. Dy, F, and O atoms coordinated to Dy are depicted as balls, and the others are shown as stick models. The minor disordered sites of O and W atoms are omitted for clarity.

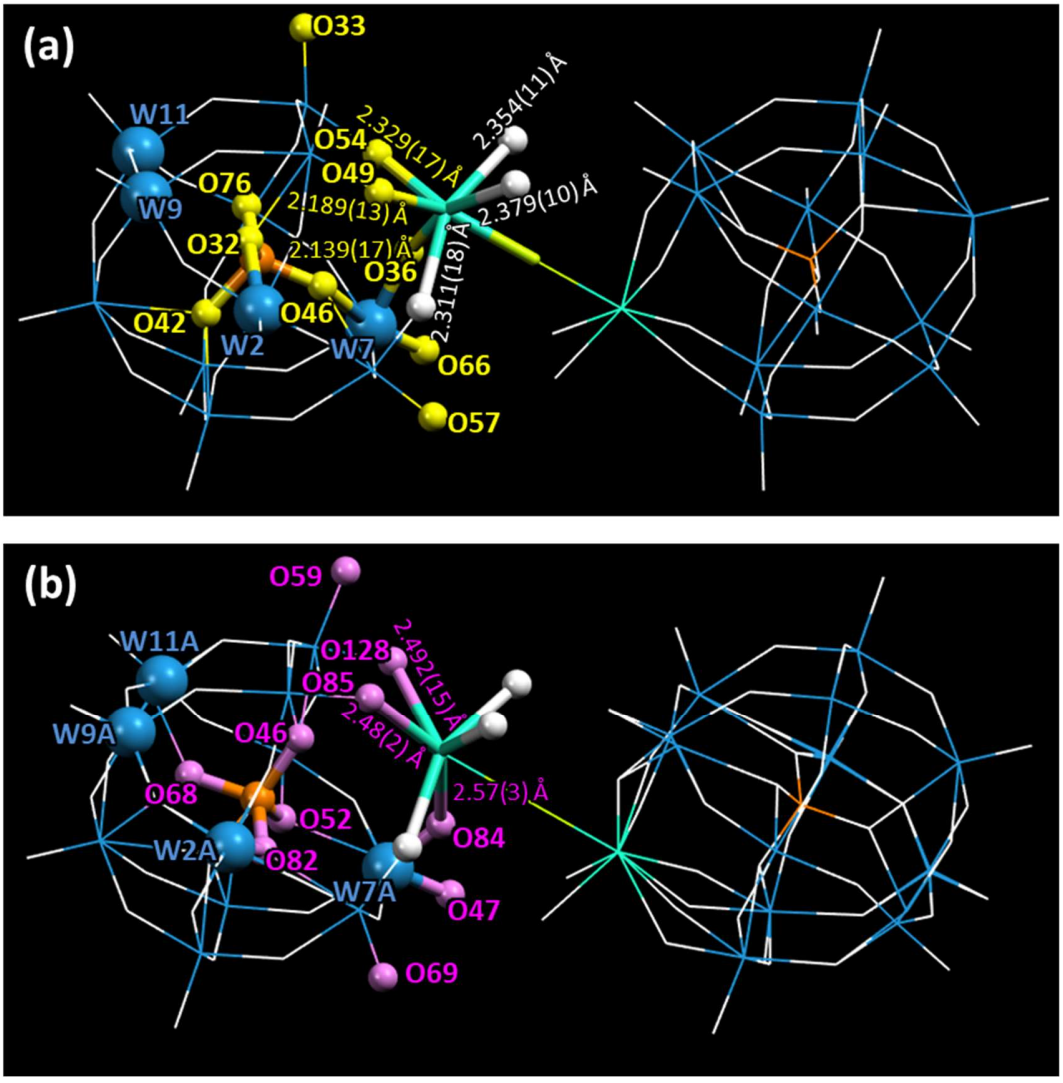

Figure 4-3. Disordered structure of $\{[(PW_{11}O_{39})Dy(H_2O)_2)]F\}^{9-}$ anion in crystal **6-Dy** at 94 K with atoms which are with occupancies of (a) 0.566(8) and (b) 0.444(8), respectively. Hydrogen atoms are omitted for

clarity. Color code is as same as that in Figure 4-2 except O atoms at disordered sites. Dy-O distances are shown in the figures.

In a complex of dinuclear Dy bridged by a single fluoride ion, Dy-F bond lengths of 2.137-2.315 Å and Dy-F-Dy angles of 169.8-180° have been reported.[192,193] The Dy-F bond lengths (2.184 Å) and Dy-F-Dy angles (180°) found in Dy_2POM are reasonable values. (Na)(B18C6) and H_2O molecules coordinated to Na form 1D supramolecular arrays. Figure 4-4 shows the structure of the one-dimensional (1D) arrays of supramolecular cations. There are two types of (Na)(B18C6) supramolecular arrays: one comprising **A** and **B**, and the other comprising **C** and **D** (**AB**- and **CD**-chains, respectively). Each is arranged in one dimension along the *c*-axis. In the **AB**-chain, two **A** units formed a dimer by the C-H•••O interaction, which formed a **B-A-A-B**-type tetramer with neighboring **B** *via* π•••π interactions between the phenylene groups. In the **CD**-chain, the two **D** units formed a dimer *via* π•••π interactions. The -CH_2-CH_2- group of the **D** unit and the π plane of the phenylene ring of the **C** unit were in contact below the van der Waals radius, indicating that C-H•••π interaction occurred between the **C** and **D** units. Consequently, a **C-D-D-C** tetramer was formed in the **CD**-chain. There was no strong interaction between the adjacent tetramers in either chain. Two types of channels parallel to the *c*-axis were formed (denoted as **Ch$_1$** and **Ch$_2$**, as shown in Figure 4-5). Channel **Ch$_1$** had minimum and maximum diameters of 4.2 and 9.7 Å, respectively, and was filled with (Na)(B18C6) units, F^- ions and H_2O molecules, according to molecular formula **1** (Figure 4-6). In contrast, **Ch$_2$** was partially penetrated by supramolecular cation **B** from the ±*a*-axes (Figure 4-5b). As shown in Figure 4-5b, the two supramolecular cations, **B**, penetrating **Ch$_2$** are the closest together at the H atom, with an H-H interatomic distance of 3.616 Å. **Ch$_2$** had a space with a minimum width of only 1.2 Å. No atoms could be assigned to the space between the two supramolecular cations of **C**. The **Ch$_2$** channel was divided into compartments separated by "bamboo nodes" as a result of the penetration of supramolecular cation **C**. Dy_2POM units were embedded in each of the compartments separated by the bamboo nodes (Figure 4-5d). The distance between the adjacent Dy_2POM units in the channel was 4.641 Å, as measured between the centers of the nearest O atoms (Figure 4-5d). Considering the van

der Waals radius of the O atom (1.52 Å), there was a space of 1.60 Å between the Dy_2POM ends along the *c*-axis (Figure 4-5c). In addition, Dy_2POM was separated by (Na)(B18C6) in the *a*- and *b*-axes directions. The central F distances between adjacent Dy_2POM units were 17.566 and 17.872 Å along the *a*- and *b*-axes, respectively (Figure 4-7), while intramolecular Dy distance was 4.368 Å. The Dy_2POM units were spatially and therefore magnetically isolated from each other in the compartments between the bamboo nodes.

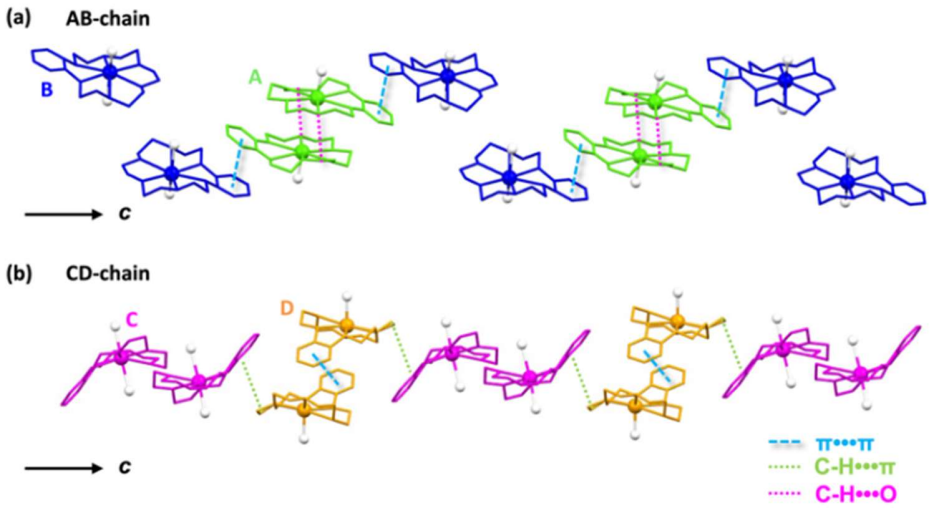

Figure 4-4. One-dimensional (1D) array of supramolecular cations in crystal **6-Dy** along the *c*-axis. The (Na^+)(B18C6) units of **A**, **B**, **C**, and **D** are shown in green, blue, magenta, and orange, respectively. The 1D chains of (a) **A** and **B** (**AB**-chain) and (b) **C** and **D** (**CD**-chain).

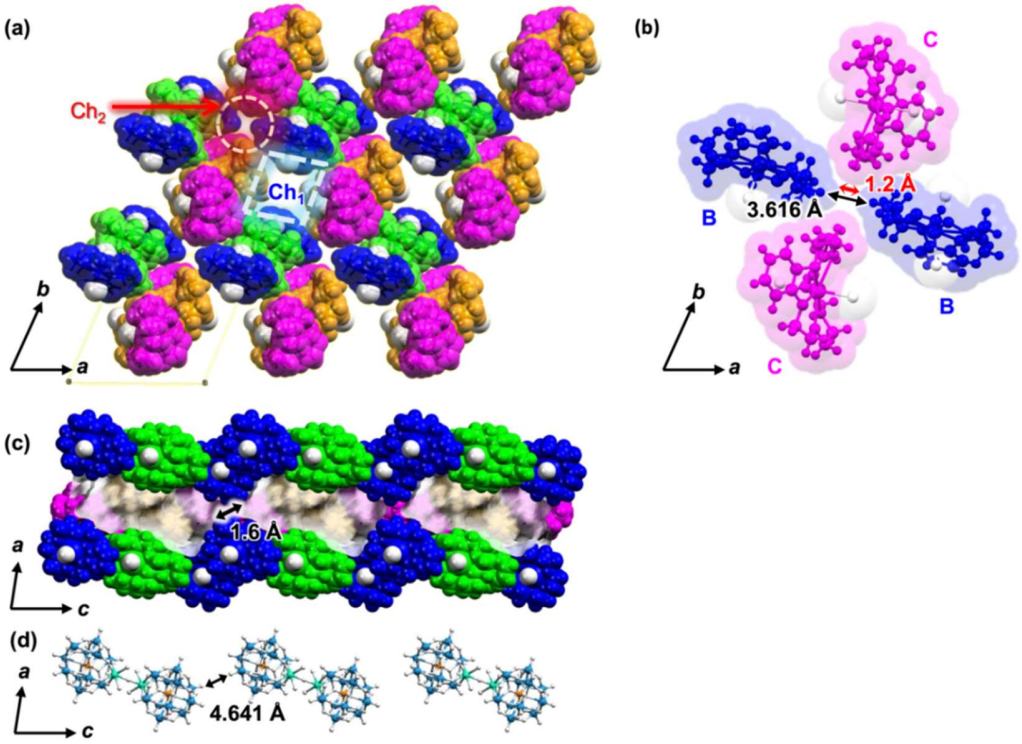

Figure 4-5. Crystal structure of **6-Dy**. The colors of supramolecular cations **A**, **B**, **C**, and **D** are the same as in Figure 4-3. Supramolecular cations are shown in the space filling model. H_2O molecules other than H_2O coordinated to Na and Dy are omitted. (a) *c*-axis projection, showing the two types of 1D channels, **Ch$_1$** and **Ch$_2$**, formed along the *c*-axis direction are indicated by dotted line squares and circles, respectively. (b) Supramolecular cation **B** penetrating **Ch$_2$**, acting similar to a "bamboo node." Black and red arrows indicate the center-to-center (3.616 Å) and end-to-end distances (1.2 Å) of the nearest hydrogen atoms. (c) *b*-axis projection showing compartments separated by bamboo nodes. (d) Alignment of Dy_2POM along the *c*-axis divided by bamboo nodes. The distance between adjacent Dy_2POM units is 4.641 Å, as measured between the centers of the nearest O atoms.

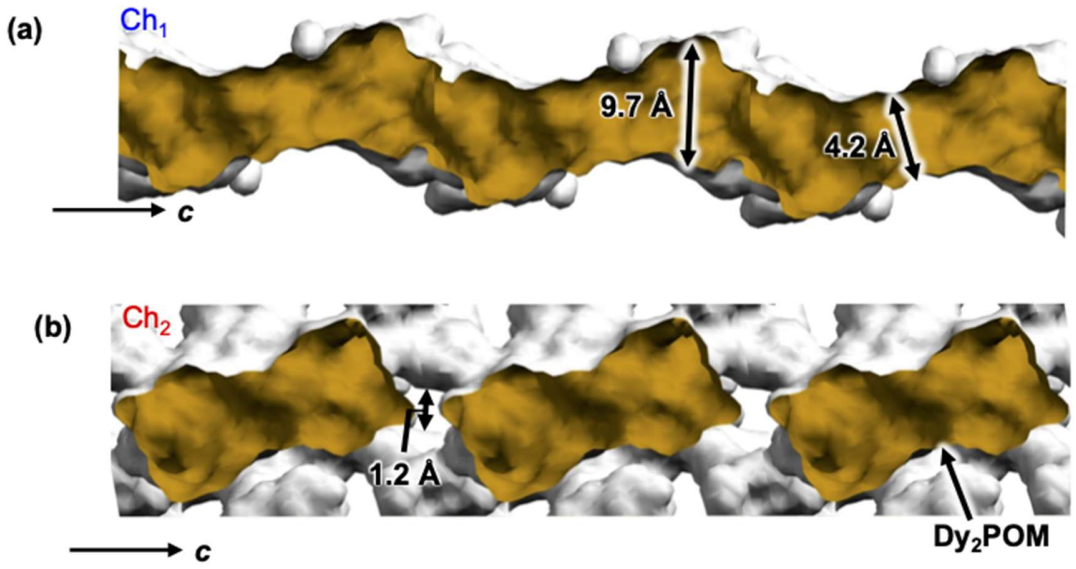

Figure 4-6. One-dimensional channel structures of (a) Ch_1 and (b) Ch_2 along the *c*-axis in crystal **6-Dy**, displayed using the void function of Mercury software. The inner wall of the channel vacancy is shown in yellow and the outer wall in white. To display the Ch_1 and Ch_2, uncoordinated crystalline H_2O molecules and Dy_2POM are removed from the structure, respectively. The distances shown are the center-to-center distances of the corresponding terminal atoms minus the van der Waals radii.

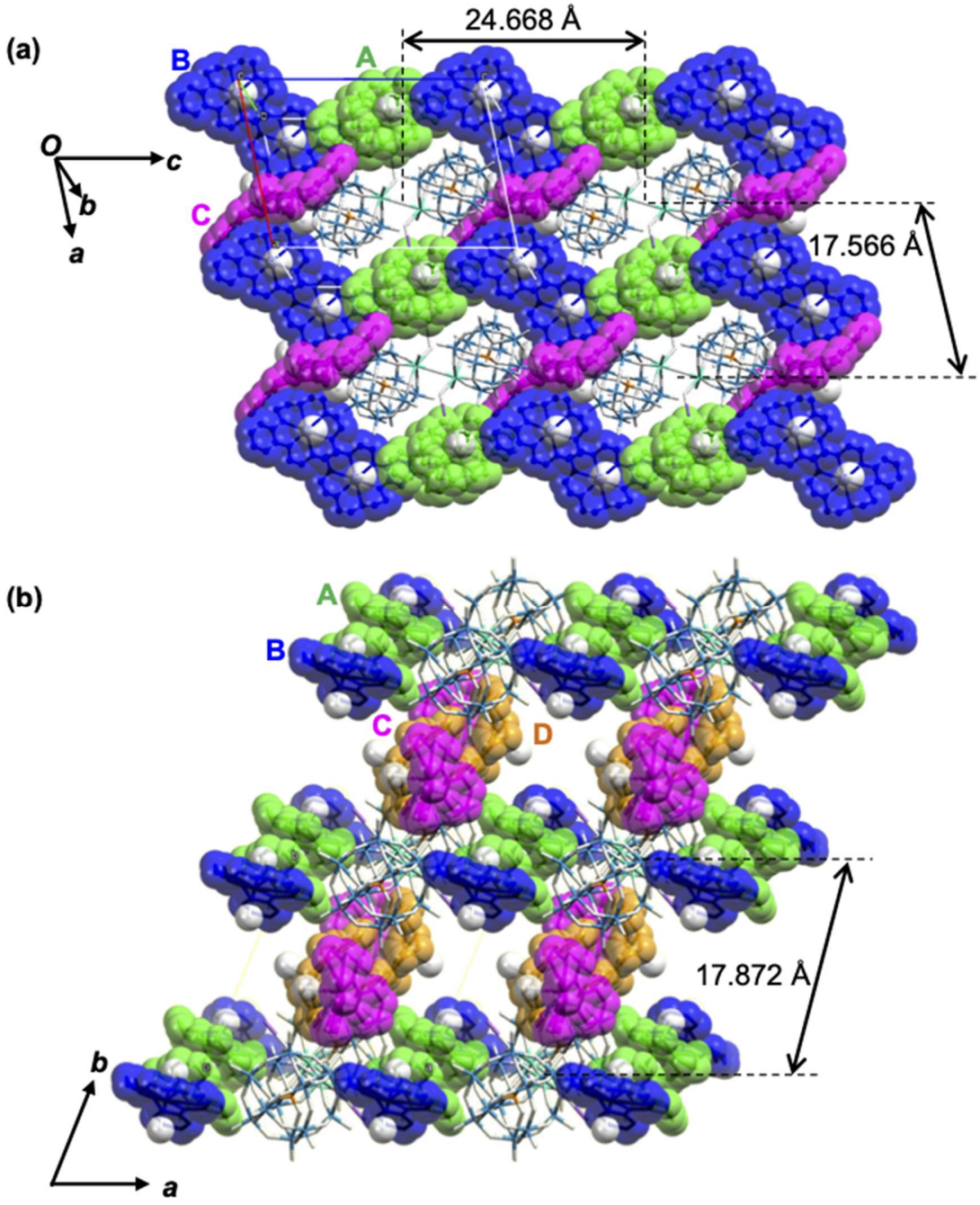

Figure 4-7. Packing structure of crystal **6-Dy** viewed along the (a) *b* and (b) *c* axes. The central F^- distances between adjacent Dy_2POMs are given in the figure.

4-4. IR spectra

The IR spectra of crystals **6** are shown in the Figure 4-8. Compounds **6** all exhibit similar profile. The band of 3645 cm^{-1} is attributed to the stretch of O-H bond of H_2O. The band near 1118 cm^{-1} implied the C–O–C asymmetric stretching vibration of B[18]crown-6 molecule. Characteristic bands around 1594, 1503 and 1450 cm^{-1} are assigned to benzene ring stretch of B[18]crown-6 molecule. As for the bands at 700-1000 cm^{-1}, that is caused by the asymmetric stretch of the W–O_c and W–O_b and of the W–O_d.

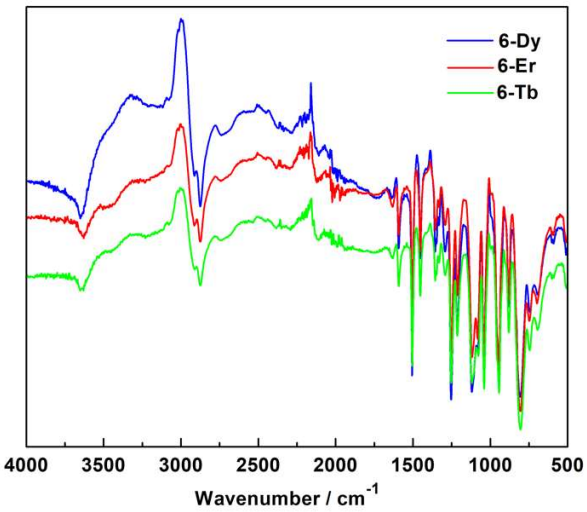

Figure 4-8. IR spectra of crystals **6-Ln**.

4-5. Power X-ray diffraction analysis

The purity of crystalline powders of crystals **6** were confirmed by powder X-ray diffraction (PXRD), which is shown in Figure 4-9. The experimental patterns of crystals **6** are in accord with the corresponding simulated patterns derived from the single crystal data, indicating the presence of mainly one crystalline phase.

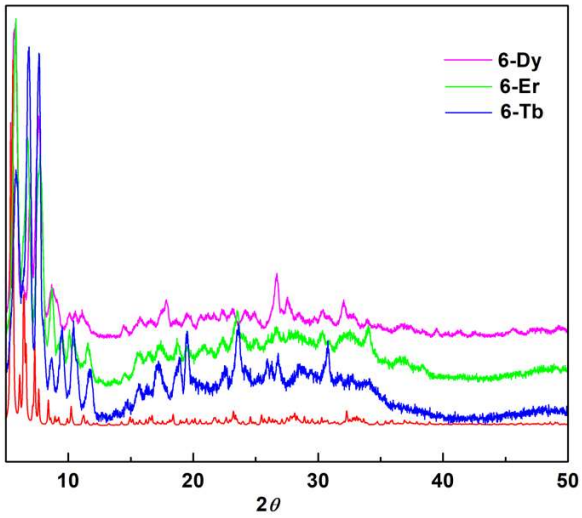

Figure 4-9. PXRD patterns of crystals **6**.

4-6. Thermogravimetric analysis

As shown Figure 4-10, the three compounds display a similar trend as the temperature increases since they are isomorphic. The amount of H_2O in the crystals is difficult to determine accurately because the TGA curve includes desorption of other molecules. Since the desorption curve is nearly linear from 100 to 180 °C, it is assumed that desorption of water molecules ends at 180 °C. The weight loss of 5.2 wt% at 180 °C corresponds to about 28 molecules of H_2O per crystal composition.

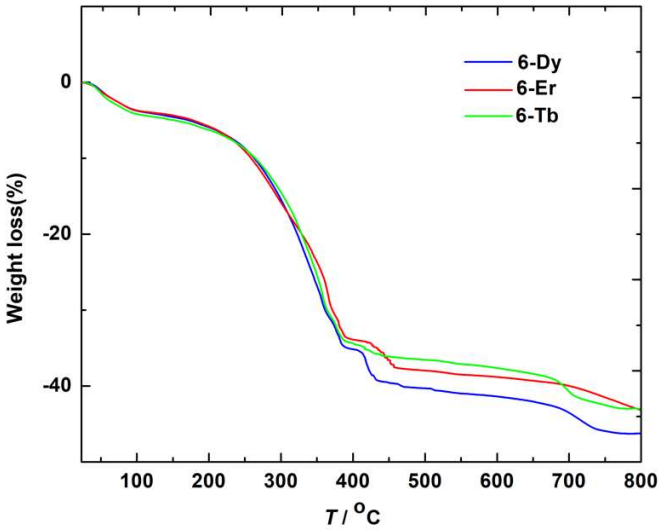

Figure 4-10. Thermogravimetric analysis of crystals **6**.

4-7. X-ray photoelectron spectroscopy (XPS)

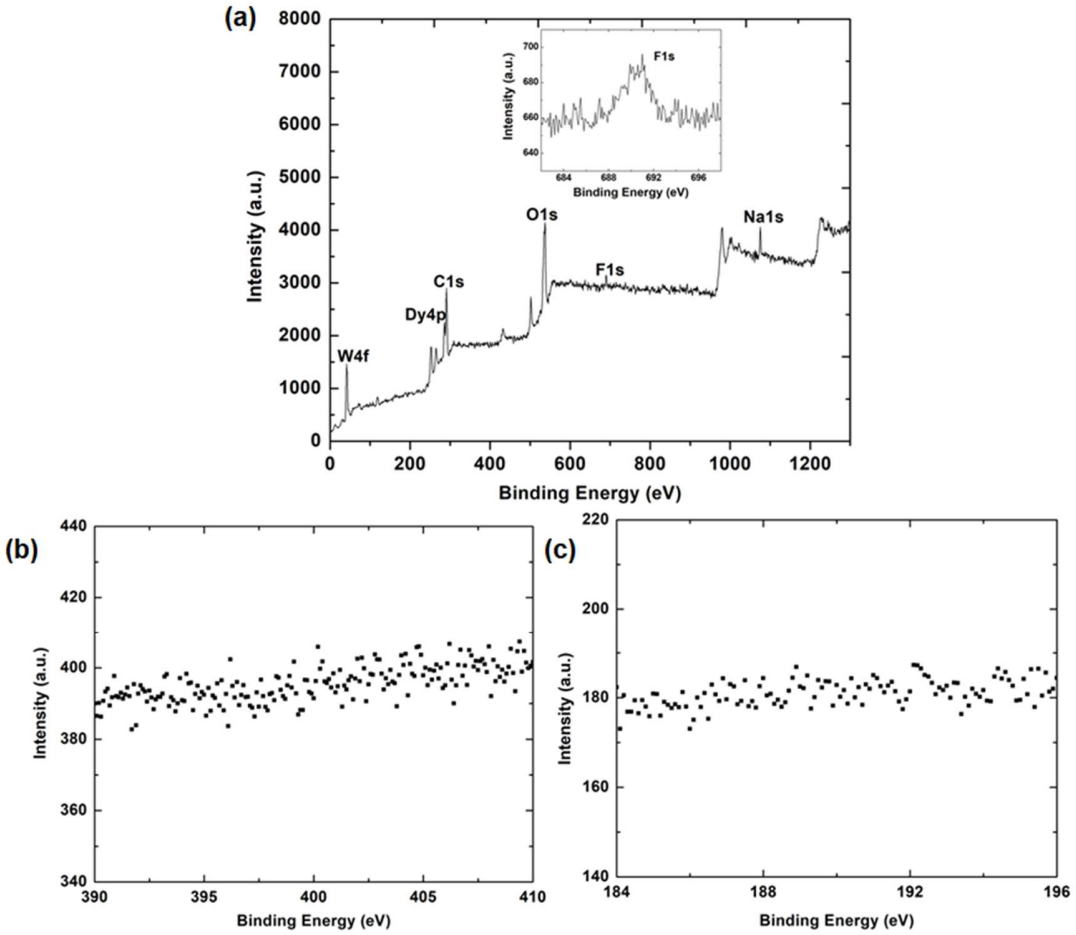

Figure 4-11. XPS spectra of crystal **6-Dy**. (a) survey scan, Inset: the core level spectrum of F 1s, (b) the core level scan for N 1s, (c) the core level scan for B 1s.

4-8. Scanning electron microscopy (SEM) and energy dispersive X-ray spectroscopy (EDS)

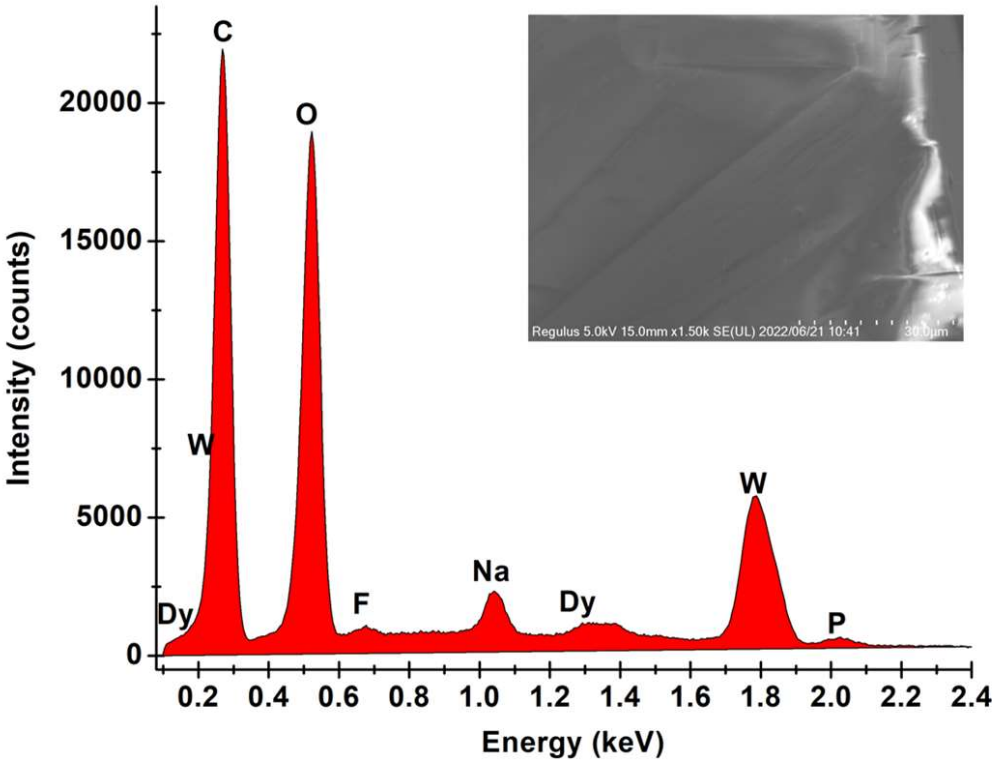

Figure 4-12. The EDS spectrum of crystal **6-Dy**. Inset: magnified SEM image of view of crystal **6-Dy**.

Table 4-1. Elemental composition results of crystal **6-Dy**.

Element	Mass (%)	Mass Norm. (%)	Atom (%)	abs. error (%) (1 sigma)
C	17.92	24.87	49.24	1.98
O	21.19	28.02	41.65	2.22
F	0.27	0.38	0.48	0.07
Na	1.71	2.37	2.46	0.12
P	0.46	0.63	0.49	0.05
W	30.20	41.92	5.42	1.43
Dy	1.30	1.80	0.26	0.10
	96.20	100.00	100.00	

When the acceleration voltage is fixed, it is generally difficult to quantify atoms that are far apart in atomic number, because the electron diffusion region becomes smaller as the atomic number increases. Therefore, only F, Na, and P with close atomic numbers were compared. Conductive

carbon tape was used to fix the sample, therefore the comparison of carbon and oxygen contents are not applied.[194]

4-9. Crystallographic data of the crystals 6.

Table 4-2. Crystallographic and structure refinements for Crystals **6**.

Crystal	**6-Dy**	**6-Er**	**6-Tb**
Formula	$C_{160}H_{296}Dy_2Na_{10}O_{166}F_2P_2W_{22}$	$C_{160}H_{296}Er_2Na_{10}O_{166}F_2P_2W_{22}$	$C_{160}H_{296}Tb_2Na_{10}O_{166}F_2P_2W_{22}$
Molecular weight/ g mol^{-1}	9575.27	9584.79	9568.12
Crystal system	triclinic	triclinic	triclinic
space group	$P\bar{1}$	$P\bar{1}$	$P\bar{1}$
a/Å	17.5657(6)	17.6045(4)	17.5397(3)
b/Å	17.8718(6)	17.8574(5)	17.8838(3)
c/Å	24.6678(7)	24.6339(5)	24.6024(4)
α/deg	83.624(3)	83.587(2)	83.6840(10)
β/deg	78.593(3)	78.712(2)	78.4080(10)
γ/deg	66.807(3)	66.803(2)	66.6190(10)
V / Å^3	6972.8(4)	6975.3(3)	6935.1(2)
Z	1	1	1
T / K	94	94	94
ρ_{calc} / g cm^{-3}	2.108	2.111	2.117
μ / mm^{-1}	20.085	9.737	19.829
F(000)	4085.0	4096.0	4086.0
2θ / °	5.384 to 145.12	3.878 to 61.984	5.386 to 145.576
Reflections collected	81221	35426	89294
Independent reflections	26470	35426	26546
Data / restraints / param	26470/517/1508	35426/403/1511	26546/328/1540
R_{int}	0.0440	0.0433	0.0341
R_1 [I > 2σ(I)]	0.0824	0.1064	0.0557
wR_2 (all data)	0.2706	0.3398	0.1681
GOF on F^2	1.035	1.170	1.063
$\Delta\rho_{max/min}$/e Å^{-3}	3.471/-1.704	16.04/-8.45	1.85/-3.22

4-10. Magnetic properties

4-10-1. Static magnetism.

The temperature dependence of the molar magnetic susceptibilities (χ_m) of crystals **6** on polycrystalline samples were measured in the temperature range of 2 – 300 K under an applied magnetic field of 1000 Oe as shown in Figure 4-13. The $\chi_M T$ values 26.77, 21.55 and 23.20 cm^3 K mol^{-1} for crystals **6-Dy**, **6-Er** and **6-Tb** at room temperature are closed to the theoretical values for two free Ln^{3+} ions 28.33 (Dy, $^6H_{15/2}$), 22.96 (Er, $^4I_{15/2}$) and 23.64 (Tb, $^7F_6$), respectively. The $\chi_m T$ value of crystal **6-Dy** increases significantly with decreasing temperature below 30 K, reaching 32.14 cm^3 K mol^{-1} at 2 K. The results indicate that weak ferromagnetic interactions between Dy cations bridged by fluoride that is strong enough to balance the thermal depopulation of excited states of Dy^{3+}.[178,193,195] On the other hand, the drop in $\chi_M T$ values of compounds **6-Er** and **6-Tb** may be ascribed to the progressive depopulation of the excited Stark sublevels and/or antiferromagnetic exchange interactions.

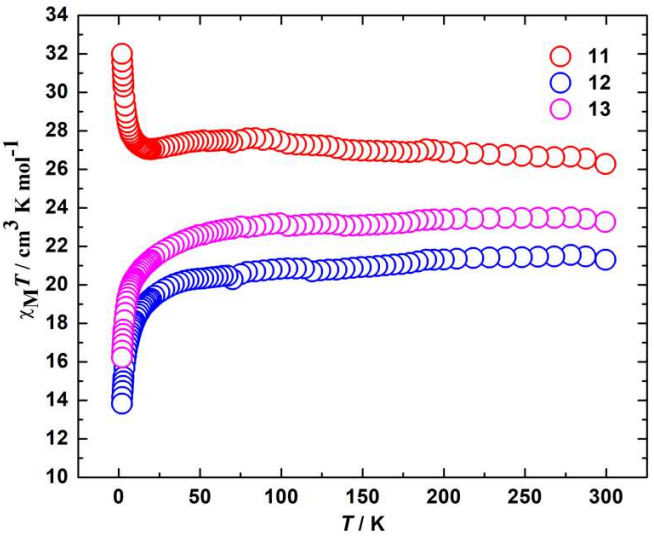

Figure 4-13. Plots of magnetic susceptibility ($\chi_M T$) *vs* temperature (T) for crystals **6**, respectively.

4-10-2. Dynamic magnetic properties of crystal 6-Dy.

To investigate the magnetic dynamics of individual Dy_2POM units, temperature and frequency dependence of *ac* susceptibilities were measured. Figure 4-14 shows the temperature and

frequency dependence of the real (χ') and imaginary (χ'') parts of the magnetic susceptibilities under zero Oe direct magnetic field of crystal **6-Dy**. Remarkable temperature and frequency dependence are observed, indicating that the Dy_2POM unit exhibits a slow relaxation of magnetization typical of SMMs. However, no peak is observed in the plots of temperature dependence and χ' and χ'' values increase rapidly with temperature decreasing, which is ascribed to the typical quantum tunneling that is common in the reported SMMs.[196–198]

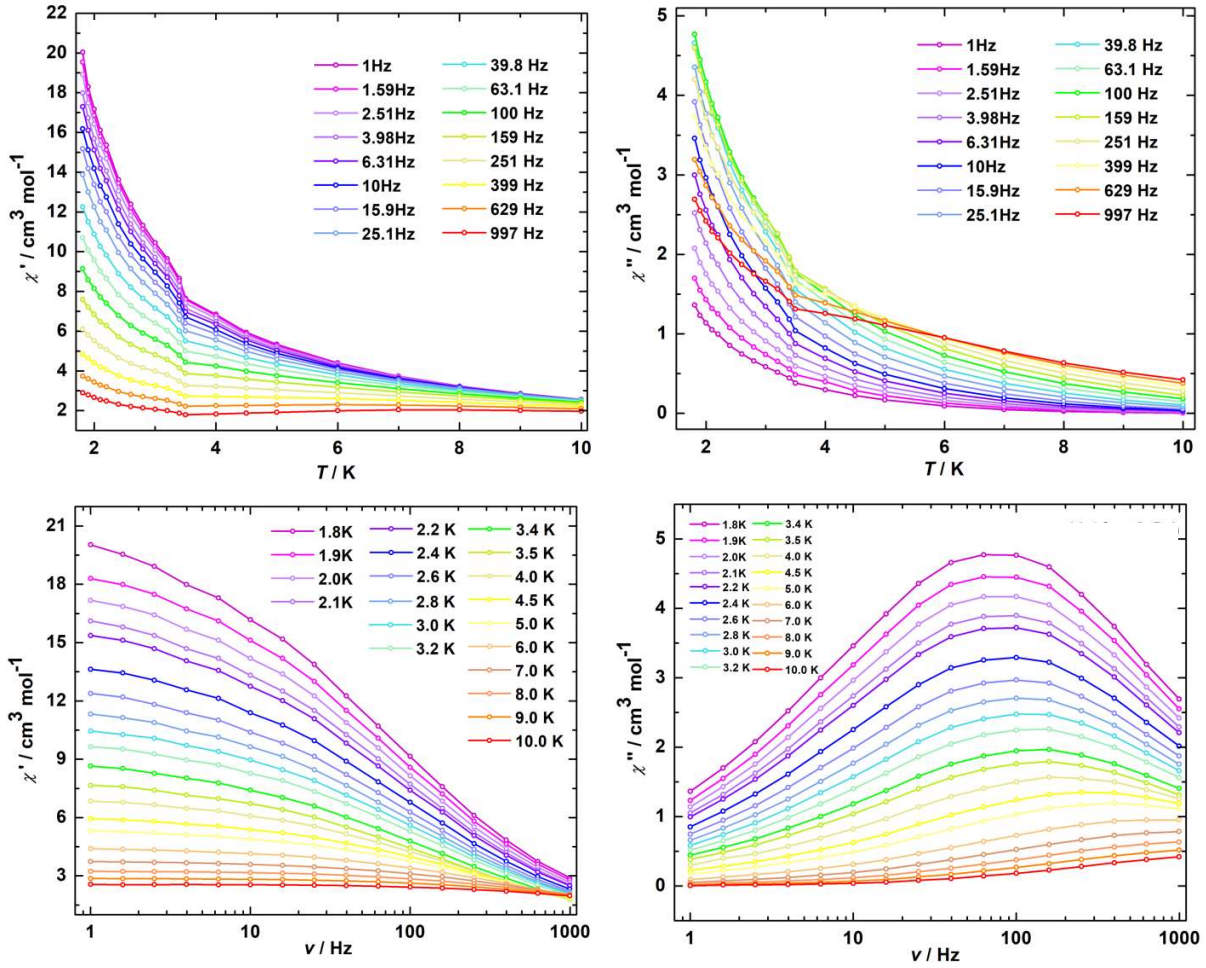

Figure 4-14. Temperature dependence and frequency dependence of χ' and χ''signals under zero direct field and an oscillating field of 3 Oe of crystal **6-Dy**.

The application of a *dc* field may fully or partly remove the ground state degeneracy and suppress the quantum tunneling.[148,149] In order to find the most suitable field for crystal **6-Dy**, susceptibilities at 1.8 K, in static field from 0 – 3000 Oe and an oscillating field of 3 Oe were

measured. As shown on Figure 4-15, from 0 – 1000 Oe, when field is increasing, peak of out-of-phase(χ'') plots shifts to lower frequency. After 1000 Oe, peak shifts back to higher frequency with field increasing. In the peaks that occur in the low frequency region, 400 Oe is the smallest dc field, which is selected as the optimum field. Therefore, the *ac* magnetic susceptibilities of crystal **6-Dy** is measured under the applied *dc* magnetic field of 400 Oe (Figure 4-16). With applied *dc* field, obvious peaks can be observed in temperature-dependence plots and the peak of out-of-phase(χ'') versus frequency(v) plots around lower temperature shifts to lower frequency as shown in Figure 4-16, which indicates that quantum tunneling effect is suppressed effectively.

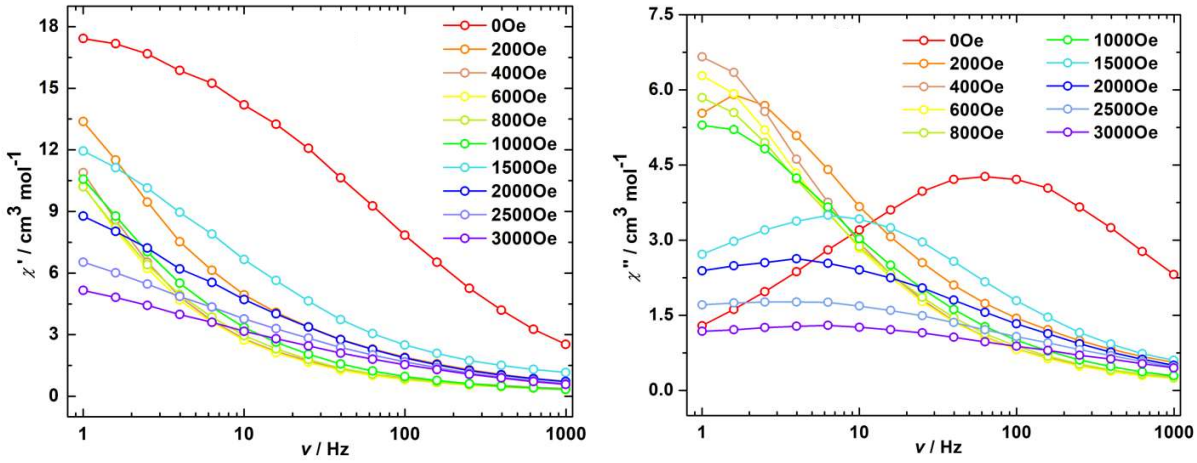

Figure 4-15. Field dependence of χ' and χ'' signals of crystal **6-Dy** at 1.8 K under different under direct field from 0 – 3000 Oe and an oscillating field of 3 Oe.

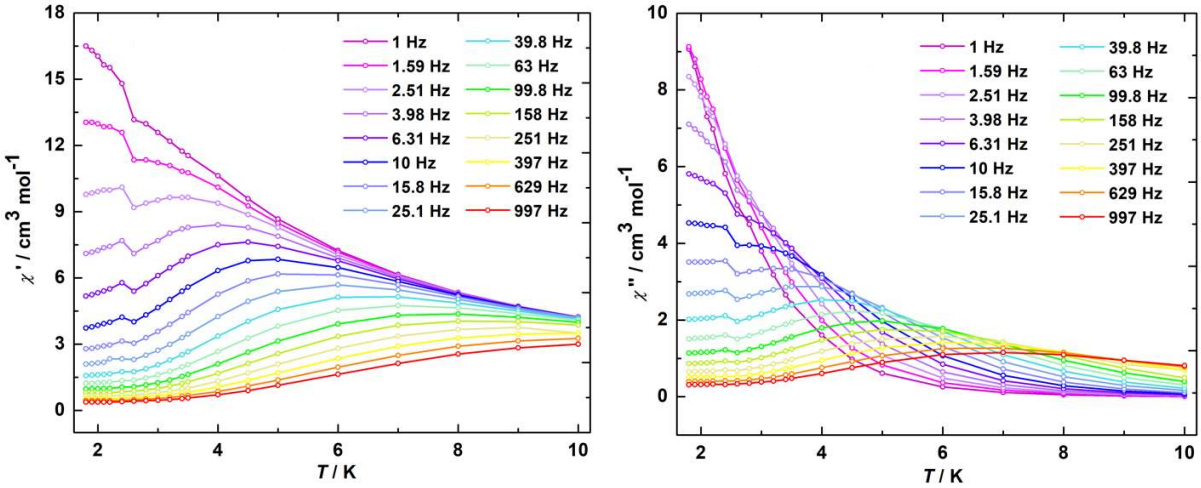

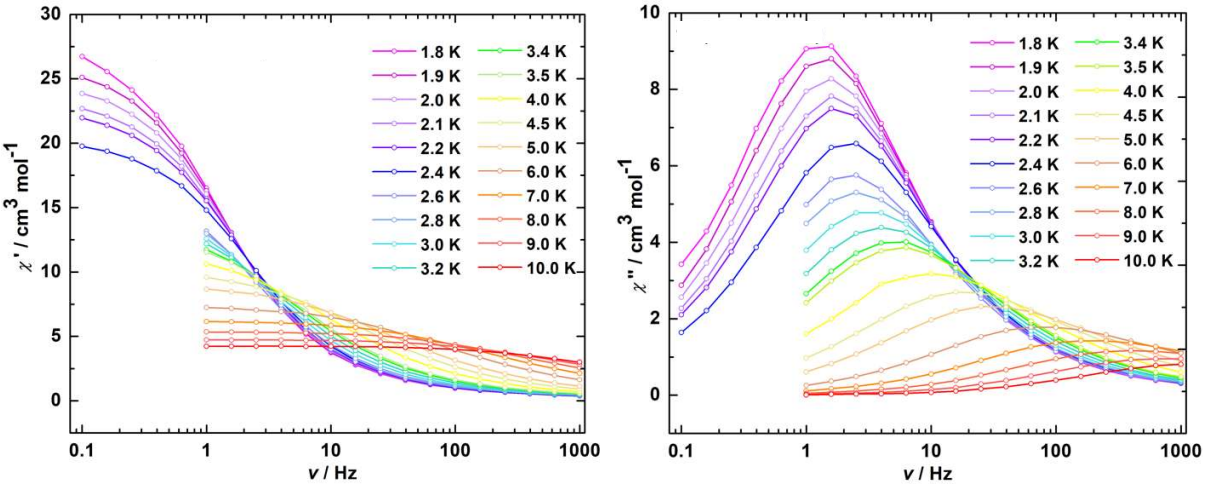

Figure 4-16. Temperature dependence and frequency dependence of χ' and χ''signals under 400 Oe direct field and an oscillating field of 3 Oe of crystal **6-Dy**.

The Cole–Cole plots of **6-Dy** under 0 and 400 Oe *dc* field in the form of χ'' *vs.* χ' were obtained and fitted to the Debye model (eq. 4.1) (Figure 4-17 and Table 4-3).[199] As shown in Figure 4-17, the Cole–Cole plots of 0 and 400 Oe direct field show a nearly semi-circle shape. The distribution coefficient (α) of 0 Oe direct field is greater than 0.34 confirming a wide distribution of the relaxation time. The distribution coefficient (α) of 400 Oe direct field is around 0.3, indicating a narrower distribution of the relaxation time than under 0 Oe dc field.

$$\chi(\omega) = \chi_S + \frac{\chi_T - \chi_S}{1+(i\omega\tau)^{(1-\alpha)}} \qquad \text{(eq. 4.1)}$$

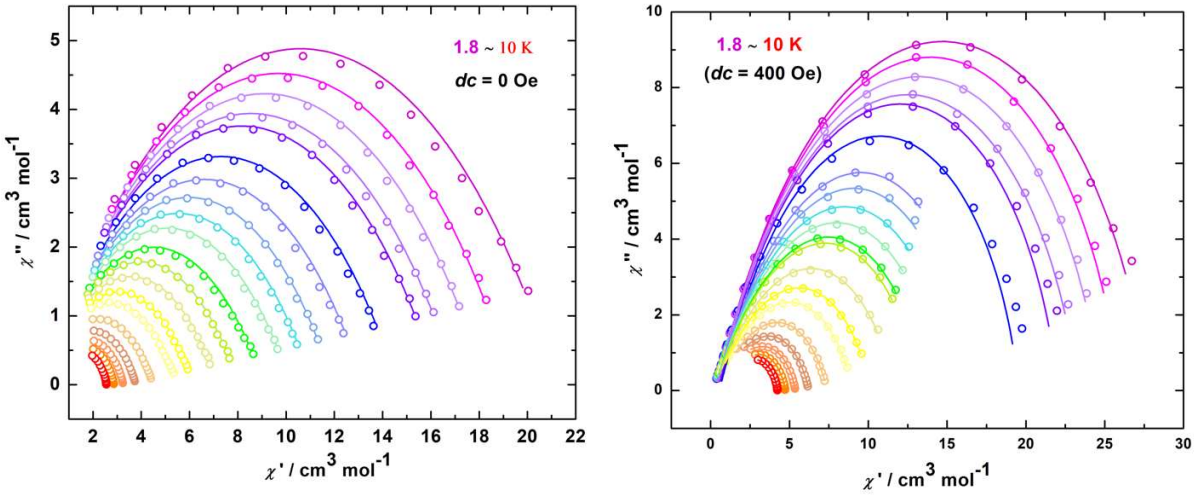

Figure 4-17. Cole−Cole plots for temperatures between 1.8−10 K under a zero and 400 Oe *dc* field with the best fit to the single Debye model for crystal **6-Dy**. The Solid lines represent fits to the data.

Table 4-3. The best fitting parameters for Cole−Cole plots of compound **6-Dy** at varying temperatures under zero and 400 Oe applied dc field.

	0 Oe			400Oe		
T	χ_S	χ_T	α	χ_S	χ_T	α
1.8	0	21.192466	0.45035163	0.47720395	28.477204	0.2633432
1.9	0	19.3937972	0.44446635	0.69298358	26.1929836	0.2337136
2	0	18.2442194	0.44742188	0.63435157	24.9343516	0.24015537
2.1	0	17.0863057	0.44985993	0.61247377	23.6124738	0.24373576
2.2	0	16.3184765	0.45059601	0.65285526	22.6528553	0.23941641
2.4	0	14.5864714	0.45686191	0.531479	20.531479	0.257792
2.6	0	13.1960621	0.45946906	0.44538531	18.4453853	0.28599004
2.8	0	11.9462859	0.45576124	0.44244205	17.442442	0.29620814
3	0	11.0758819	0.46236295	0.40297562	16.4029756	0.31354316
3.2	0	10.1693286	0.46430385	0.41549169	15.2154917	0.31935654
3.4	0	9.05940515	0.47166921	0.41065941	14.2106594	0.33015173
3.5	0	8.02227386	0.46693983	0.49149924	13.4914992	0.31846465
4	0	7.15589366	0.47337803	0.45522819	11.9552282	0.35379342
4.5	0	6.13996775	0.4739653	0.5754422	10.2754422	0.35112705
5	0	5.5714513	0.48668961	0.63509855	9.13509855	0.3608778
6	0.03073985	4.50138187	0.485899	0.90417032	7.40417032	0.35140942
7	0.32027434	3.7928435	0.46476434	0.81421822	6.31421822	0.38144872
8	0.66946806	3.27265807	0.42838084	1.1274637	5.4274637	0.35959779
9	0.90865253	2.88093638	0.38782117	1.37139023	4.77139023	0.33849239
10	1.02671352	2.56745008	0.34751153	1.61126828	4.26126828	0.30040819

Magnetic relaxation time (τ) was calculated using the single-relaxation Debye model (Figure 4-17 and Tables 4-3). Temperature dependence of τ^{-1} under 0 and 400 Oe dc field is shown in Figure 4-18. It is worth noting that the τ of **6-Dy** became weakly dependent on T as the temperature decreased under both dc field, implying the existence of multiple pathways for the relaxation of the magnetization. The magnetization relaxation barriers of **6-Dy** under 0 and 400 Oe dc field were determined from the frequency-dependent data according to equation 4.2 and equation 4.3, respectively. τ_{QTM} represents the temperature-independent QTM. The first term of eq. 4.3 represents the direct relaxation process, where A is the fitting parameter, and H is the magnetic field. The second term represents the Orbach process of thermally activated relaxation. U_{eff} is the effective energy barrier for magnetization reversal, and k_{B} is Boltzmann's constant.[200]

Without a direct magnetic field, a full model including various combination of QTM, Raman and Orbach relaxation process have been investigated to fit the experimental data, and the best result was obtain for the QTM+Orbach model (eq. 4.2) with $U_{\text{eff}}/k_{\text{B}}$ = 14.8 K, τ_0 = 2.38 × 10^{-5} s, and τ_{QTM} = 2.74 × 10^{-3} s. The obtained τ_0 and $U_{\text{eff}}/k_{\text{B}}$ values were comparable to those of other reported Dy dinuclear SMMs.[201,202] With the application of 400 Oe *dc* field, the temperature dependence of τ was reproduced using eq. 4.3 with $U_{\text{eff}}/k_{\text{B}}$ = 28.6 K, τ_0 = 3.04 × 10^{-5} s, and A = 1.37 × 10^{-10} s. Because the temperature dependence of τ could be fitted with a direct term, QTM was effectively suppressed under a direct magnetic field of 400 Oe.

$$\tau^{-1} = \tau_{QTM}^{-1} + \tau_0^{-1} exp\left(-\frac{U_{eff}}{k_B T}\right), \qquad \text{(eq. 4.2)}$$

$$\tau^{-1} = AH^4T + \tau_0^{-1} exp\left(-\frac{U_{eff}}{k_B T}\right). \qquad \text{(eq. 4.3)}$$

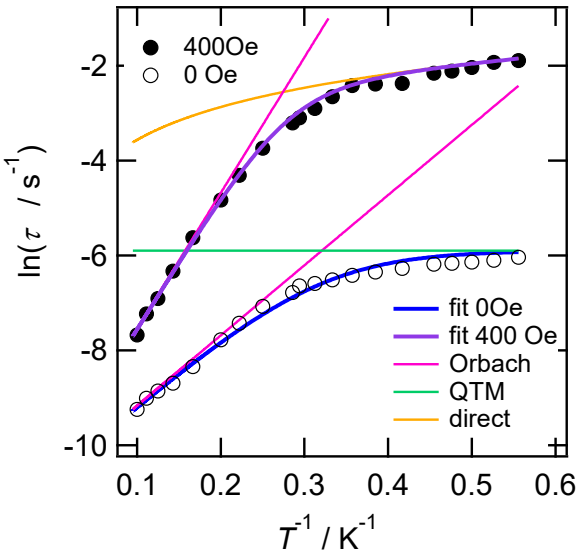

Figure 4-18**.** Magnetic relaxation rate for crystal **6-Dy** by AC magnetometry under 0 and 400 Oe direct magnetic fields (note: log-log scale). Black-open and -closed circles correspond to the τ under 0 and 400 Oe direct magnetic fields, respectively. Blue and purple lines were fit with eq. (4.2) using $U_{\text{eff}} = 14.8$ K, $\tau_0 = 2.38 \times 10^{-5}$ s, and $\tau_{QTM} = 2.74 \times 10^{-3}$ s, and with eq. (4.3) using $U_{\text{eff}} = 28.6$ K, $\tau_0 = 3.04 \times 10^{-5}$ s, and $A = 1.37 \times 10^{-10}$ Oe^{-4} K^{-1} s^{-1}, respectively. Magenta-, green- and orange-color lines are the Orbach, QTM, and direct components, respectively.

4-10-3. Dynamic magnetic properties of crystal 6-Er

Figure 4-19 shows the temperature dependence of the real (χ') and imaginary (χ'') parts of the magnetic susceptibilities under zero Oe direct magnetic field of crystal **6-Er**. Weak temperature dependence is observed. Therefore, magnetic susceptibilities at 1.8 K, in static field from 0 – 3000 Oe and an oscillating field of 3 Oe were measured to find the optimum dc field. As shown on Figure 4-20, from 0 – 2200 Oe, when filed is increasing, peak shifts to lower frequency. After 2200 Oe, peak shifts to higher frequency with field increasing. In the peaks that occur in the low frequency region, 2000 Oe is the smallest dc field, which is selected as the optimum field. Therefore, the *ac* magnetic susceptibilities of crystal **6-Er** were measured under the applied *dc* magnetic field of 2000 Oe (Figure 4-21). With applied *dc* field, remarkable temperature and frequency dependence as well as obvious peaks can be observed, displaying a slow relaxation of magnetization typical of SMMs.

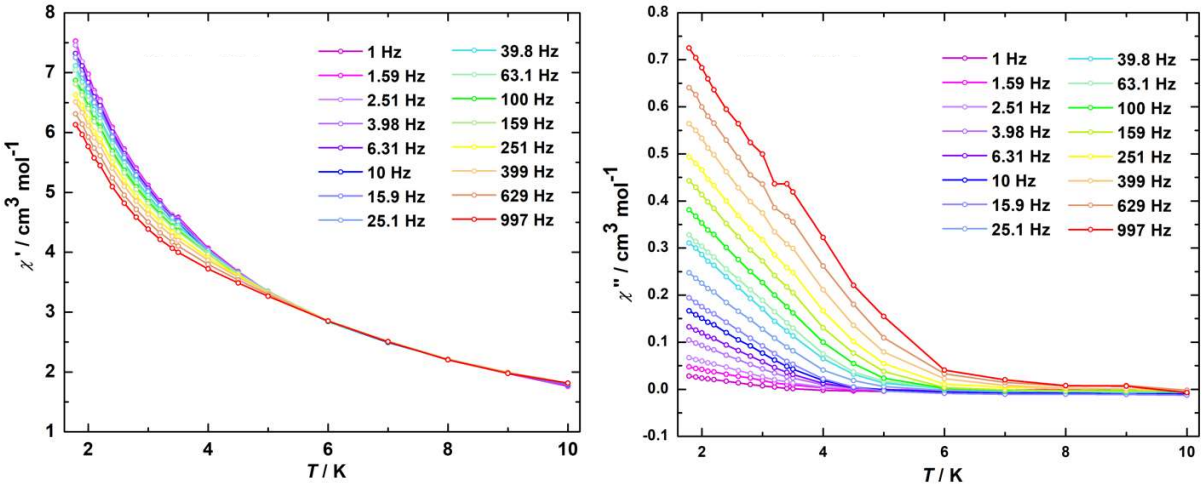

Figure 4-19. Temperature dependence of χ' and χ''signals of crystal **6-Er** under zero direct field and an oscillating field of 3 Oe.

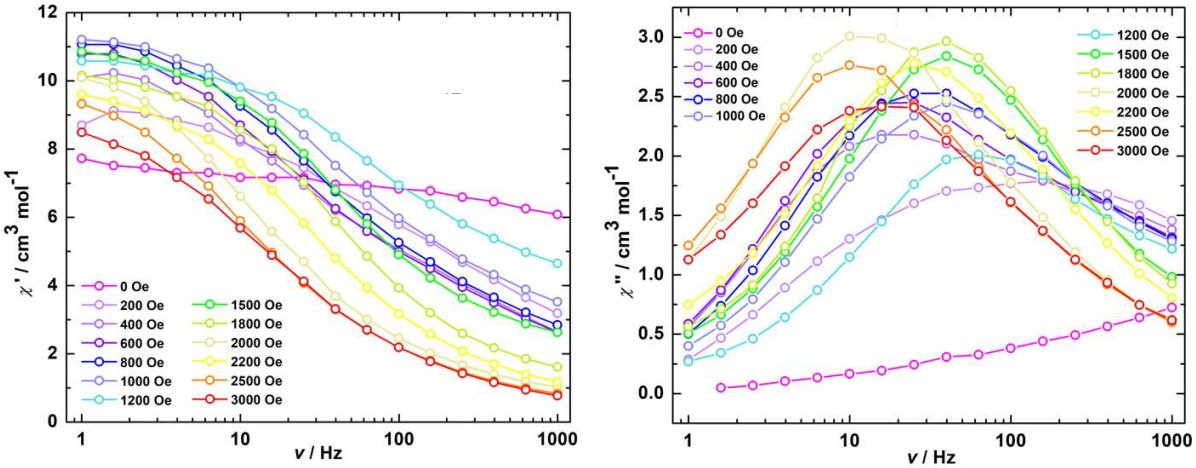

Figure 4-20. Field dependence of χ' and χ'' signals of crystal **6-Er** at 1.8 K under different under direct field from 0 – 3000 Oe and an oscillating field of 3 Oe.

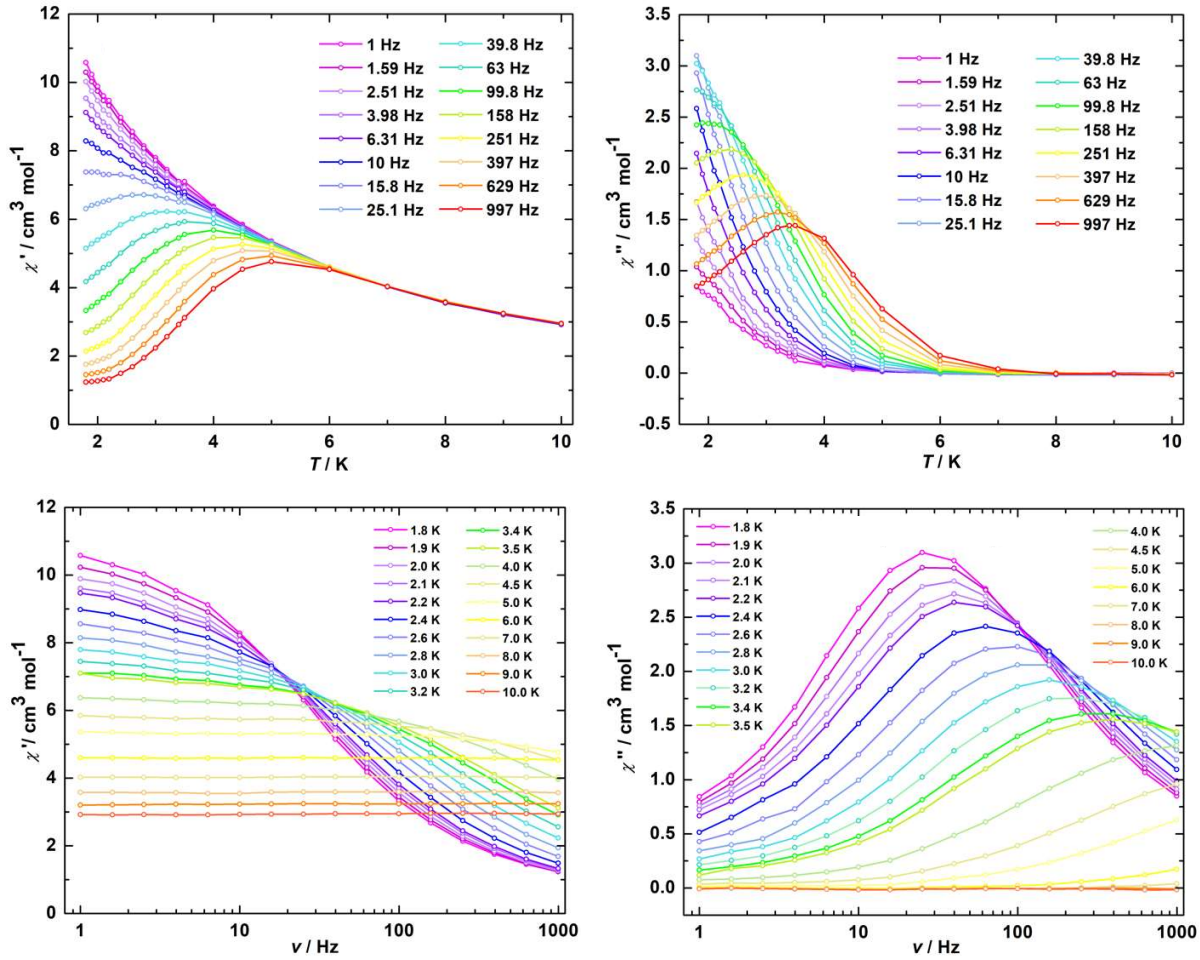

Figure 4-21. Temperature dependence and frequency dependence of χ' and χ''signals of crystal **6-Er** under 2000 Oe direct field and an oscillating field of 3 Oe.

The Cole–Cole plot of **6-Er** under 2000 Oe *dc* field in the form of χ'' *vs.* χ' was obtained and fitted to the Debye model (eq. 4.1) (Figure 4-22 and Table 4-4). The Cole–Cole plots show a nearly semi-circle shape and a distribution coefficient (α) greater than 0.3 was determined, confirming a relatively wide distribution of the relaxation time.

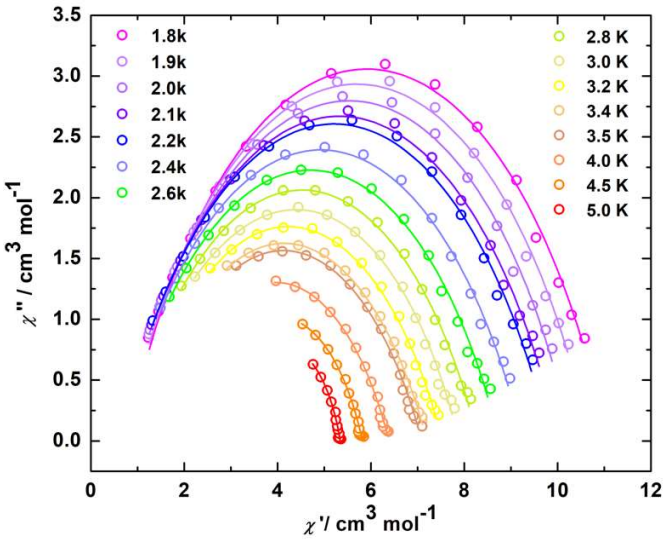

Figure 4-22. Cole−Cole plots for temperatures between 1.8−5 K under 2000 Oe *dc* field with the best fit to the single Debye model for crystal **6-Er**. The Solid lines represent fits to the data.

Table 4-4. The best fitting parameters for Cole−Cole plots of compound **6-Er** at varying temperatures under 2000 Oe applied dc field.

T	χ_S	χ_T	α
1.8	0.66534024	11.1653402	0.33110291
1.9	0.7039369	10.7039369	0.32457446
2	0.59496191	10.3949619	0.34147093
2.1	0.39194694	10.1919469	0.36993665
2.2	0.32326709	10.0232671	0.37846386
2.4	0.37205503	9.37205503	0.38023339
2.6	0.51325835	8.81325835	0.37498977
2.8	0.55894545	8.35894545	0.38239638
3	0.57194299	7.97194299	0.3953987
3.2	0.68009244	7.58009244	0.39760431
3.4	0.83245044	7.23245044	0.39869487
3.5	0.91779784	7.11779784	0.4005799
4	1.39696855	6.39696855	0.38117195
4.5	2.31976489	5.81976489	0.32964393
5	2.34750295	5.34750295	0.2956179

The magnetization relaxation time (τ) of **6-Er** under 2000 Oe dc field were determined from the frequency-dependent data according to Debye model (Figure 4-22 and Tables 4-4). The magnetization relaxation barriers of **6-Er** under 2000 Oe *dc* field were determined from the frequency-dependent data according to equation 4.4, by which the experimental data can be best-fitted. The first term of eq. 4.4 represents the bottleneck process, where A is the fitting parameter, and H is the magnetic field. The temperature dependence of ln(τ) could be fitted using eq. 4.4 with U_{eff}/k_B = 24.5 K, τ_0 = 4.1 × 10-^{7} s, and A = 6.70 × 10^{-12} s (Figure 4-23).

$$\tau^{-1} = AH^4T^2 + {\tau_0}^{-1}exp\left(-\frac{U_{eff}}{k_BT}\right) \quad \text{(eq. 4.4)}$$

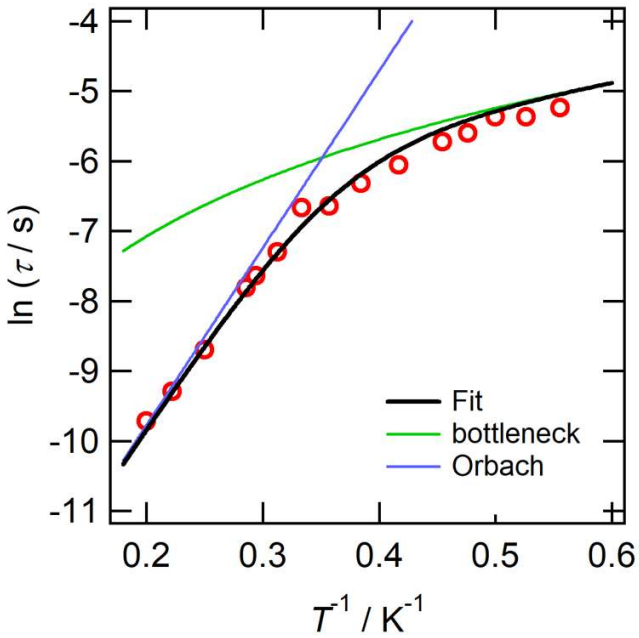

Figure 4-23**.** Magnetic relaxation rate for crystal **6-Er** by AC magnetometry under 2000 Oe direct magnetic fields (note: log-log scale). Red-open circles correspond to the τ. Black line is fit with eq. (4.3) using U_{eff} = 24.5 K, τ_0 = 4.1 × 10^{-7} s, and A = 6.70 × 10^{-12} Oe^{-4} K^{-1} s^{-1}. Green- and blue-colored lines are the bottleneck and Orbach process, respectively.

4-10-4. Dynamic magnetic properties of crystal 6-Tb

Under zero *dc* field, in the range of 2 – 10 K, crystal **6-Tb** doesn't show any signal of temperature-dependence in both in-phase and out-of-phase plots as shown in Figure 4-24.

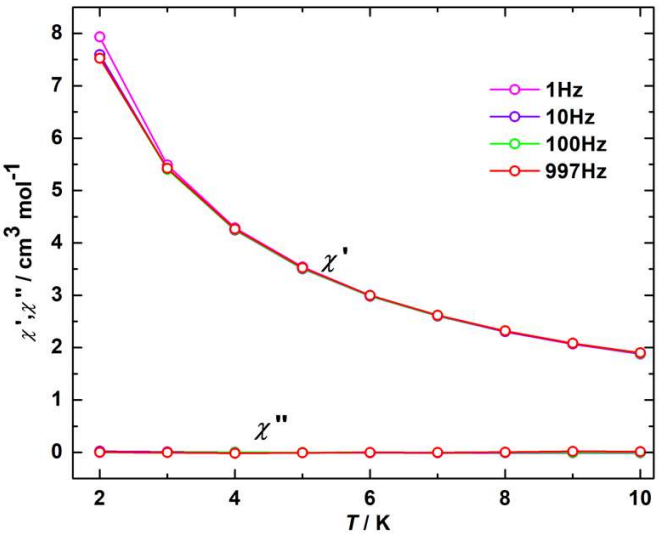

Figure 4-24. Temperature dependence of χ' and χ''signals of crystal **6-Tb** under zero direct field and an oscillating field of 3 Oe.

4-11. Conclusion

Using (Na)(B18C6) as a counter cation, we succeeded in isolating three fluoride-bridged dinuclear Ln complexes with lacunary Keggin ligands (Ln_2POM) in the crystals $[(Na)(B18C6)(H_2O)_{0.5}]_2[(Na)(B18C6)(H_2O)_{1.5}]_2[(Na)(B18C6)(H_2O)]_2[(Na)(B18C6)(H_2O)_{1.75}]_2[((PW_{11}O_{39})Ln(H_2O)_2)_2F)][(Na)(B18C6)]_2(F)\bullet 12H_2O$ (Ln = Tb, Dy and Er for **6-Tb**, **6-Dy** and **6-Er**, respectively). (Na)(B18C6) was one-dimensionally arranged in the crystal, forming a bamboo-like channel structure. Ln_2POM units were embedded between "bamboo nodes" and completely isolated from neighbouring complexes. Thus, it was possible to evaluate the magnetic properties of Ln_2POM as a single molecule. Weak ferromagnetic interactions between Dy cations bridged by fluoride were observed. Dy_2POM (**6-Dy**) and Er_2POM (**6-Er**) display magnetic relaxation characteristics of an SMM at low temperatures Magnetic relaxation proceeded via the Orbach process, and the absolute values of the

effective energy barrier and relaxation time indicated that the SMM properties were essentially attributable to single ions.

There are two possible reasons for the observed SMM behaviour: the effect of the diamagnetic lacunary POM ligands and the effect of spatial isolation by supramolecular cations. The supramolecular approach is effective in achieving isolated SMM structures in crystals for complexes where spatial isolation is essential for SMM behaviour. [115] In future, we plan to test its usefulness with other SMM candidate molecules.

Chapter V

General Conclusion

In this thesis, I have explored the magnetic properties of multinuclear lanthanide complexes with α-lacunary Keggin POMs as a ligand, which has many active oxygen sites and a clear symmetry, by controlling the arrangement of the complexes using the symmetry and self-organizing ability of the counter cations.

In Chapter 3, I discussed the effect of simple ammonium counter cations on the symmetry of lanthanide trinuclear triangle (Ln_3CO_3) units formed by a μ_3-η_2:η_2:η_2-carbonate ligand sandwiched by a lacunary Keggin POMs [PW_9O_{34}] with C_{3v} symmetry. Simple ammonium cations, methylammonium, dimethylammonium, trimethylammonium, tetramethylammonium and diprotonated 1,4-Diazabicyclo[2.2.2]octane with the symmetry of $C_{\infty v}$, C_{2v}, C_{3v}, T_d and D_{3h}, respectively, were provided. Ten sandwich-type POMs $(CH_3NH_3^+)_{10}Na[(PW_9O_{34})_2(H_2OLn)_3CO_3]$ (Ln = Tb, Dy, Er and Y for crystals **1-Tb**, **1-Dy**, **1-Er** and **1-Y**, respectively, MA = methylammonium), $((CH_3)_2NH_2^+)_{11}[(PW_9O_{34})_2(H_2OTb)_3CO_3]$ (**2**) (DMA = dimethylammonium), $(CH_3)_3NH^+)_8Na_3[(PW_9O_{34})_2(H_2OTb)_3CO_3]$ (**3**), (TriMA = trimethylammonium), $(CH_3)_4N^+)_6Na_5[(PW_9O_{34})_2(H_2OTb)_3CO_3]$ (**4**), (TMA = tetramethylammonium), and $(H_2DABCO^{2+})_6[(PW_9O_{34})_2(H_2OLn)_3CO_3](BF_4)$ (Ln = Tb, Dy and Er for crystals **5-Tb**, **5-Dy** and **5-Er**, respectively), were synthesized. Crystals **1** and **4** gave space groups with high symmetry, $P63/m$ and $R\bar{3}m$, respectively, and an equilateral triangular (Ln_3CO_3) structure was maintained in the complex. The highly symmetric structure of these crystals is induced by the supramolecular structure formed by hydrogen bonding between ammonium derivatives and water molecules. The number of hydrogen-bonding sites is one of the critical parameters that leads to the high symmetry of the crystals. Crystals **2** and **3** take the polar space groups $Pna2_1$ and $Cmc2_1$, respectively, because the DMA^+ and $TriMA^+$ cations have low symmetry and only two and one hydrogen bonding sites, respectively. In crystal **5**, another highly symmetric space group of $P63/mcm$ was achieved by the introduction of highly symmetric BF_4^- (T_d) anions through hydrogen bonding interaction not the $[H_2DABCO]^{2+}$ (D_{3h}) cations. However, the equilateral triangle composed of three Ln^{3+} ions could not be maintained. Crystals **1-Tb**, **1-Dy**, **1-Er**, **2**, **3** and **4** exhibited a slow relaxation of magnetization typical of single molecular magnets in temperature-dependent ac susceptibility measurements under static magnetic field. It's worth noting that the magnetic relaxation in equilateral Ln_3-triangle is more prominent, which will be deeply studied in future.

In Chapter 4, the supramolecular approach is adopted to isolate SMM structures in crystals. Using (Na)(B18C6) as a counter cation, we succeeded in isolating three fluoride-bridged dinuclear Ln complexes with lacunary Keggin ligands (Dy_2POM) in the crystals $[(Na)(B18C6)(H_2O)_{0.5}]_2[(Na)(B18C6)(H_2O)_{1.5}]_2[(Na)(B18C6)(H_2O)]_2[(Na)(B18C6)(H_2O)_{1.75}]_2[((PW_{11}O_{39})Ln(H_2O)_2)_2F)][(Na)(B18C6)]_2(F)\bullet 12H_2O$ (Ln = Tb, Dy and Er for **6-Tb**, **6-Dy** and **6-Er**, respectively). (Na)(B18C6) was one-dimensionally arranged in the crystal, forming a bamboo-like channel structure. Ln_2POM units were embedded between "bamboo nodes" and completely isolated from neighbouring complexes. Thus, it was possible to evaluate the magnetic properties of Ln_2POM as a single molecule. Weak ferromagnetic interactions between Dy cations bridged by fluoride were observed. Dy_2POM (**6-Dy**) and Er_2POM (**6-Er**) display magnetic relaxation characteristics of an SMM at low temperatures Magnetic relaxation proceeded via the Orbach process, and the absolute values of the effective energy barrier and relaxation time indicated that the SMM properties were essentially attributable to single ions. There are two possible reasons for the observed SMM behaviour: the effect of the diamagnetic lacunary POM ligands and the effect of spatial isolation by supramolecular cations. The supramolecular approach is effective in achieving isolated SMM structures in crystals for complexes where spatial isolation is essential for SMM behaviour. [115] In future, we plan to test its usefulness with other SMM candidate molecules.

In this thesis, the equilateral triangle motifs composed of three Ln^{3+} ions bridged by one carbonate ligand were successfully constructed within the sandwich POM anions by introducing highly symmetric organic cations. Meanwhile, the influence of symmetry compatibility and hydrogen bonding interaction between cations and POM anions, were studied. We found that the symmetry and hydrogen bonding interaction play a significant role in the assembly structure of POMs. In addition, we proved that the supramolecular cations can be used in the isolation of SMM molecule successfully.

References

1. Cohen, M. D., Schmidt, G. M. J. & Sonntag, F. I. 384. Topochemistry. Part II. The photochemistry of trans-cinnamic acids. *Journal of the Chemical Society (Resumed)* 2000–2013 (1964).
2. Schmidt, G. M. J. Photodimerization in the solid state. *Pure and Applied Chemistry* **27**, 647–678 (1971).
3. Benseghir, Y. *et al.* Co-immobilization of a Rh Catalyst and a Keggin Polyoxometalate in the UiO-67 Zr-Based Metal-Organic Framework: In Depth Structural Characterization and Photocatalytic Properties for CO2 Reduction. *J Am Chem Soc* **142**, 9428–9438 (2020).
4. Naumov, P., Chizhik, S., Panda, M. K., Nath, N. K. & Boldyreva, E. Mechanically Responsive Molecular Crystals. *Chemical Reviews* vol. 115 12440–12490 Preprint at https://doi.org/10.1021/acs.chemrev.5b00398 (2015).
5. Luty, T. A role of molecular compressibility in transformation mechanism of mixed-stack organic charge-transfer crystals. *Journal of the Physical Society of Japan* **61**, 3636–3642 (1992).
6. Luty, T. & Eckhardt, C. J. General theoretical concepts for solid state reactions: quantitative formulation of the reaction cavity, steric compression, and reaction-induced stress using an elastic multipole representation of chemical pressure. *J Am Chem Soc* **117**, 2441–2452 (1995).
7. Koshihara, S., Takahashi, Y., Sakai, H., Tokura, Y. & Luty, T. Photoinduced cooperative charge transfer in low-dimensional organic crystals. *The Journal of Physical Chemistry B* vol. 103 2592–2600 Preprint at (1999).
8. Haviv, E., Shimon, L. J. W. & Neumann, R. Photochemical reduction of CO2 with visible light using a polyoxometalate as photoreductant. *Chemistry–A European Journal* **23**, 92–95 (2017).
9. Qiu, F. *et al.* Flexible Sensors: Flexible Monolayer Molecular Crystal-Field Effect Transistors for Ultrasensitive and Selective Detection of Dimethoate (Adv. Electron. Mater. 11/2020). *Advanced Electronic Materials* **6**, 2070046 (2020).
10. Haynes, W. M., Lide, D. R. & Bruno, T. J. *CRC handbook of chemistry and physics*. (CRC press, 2016).
11. Li, M. *et al.* Growth defects of organic crystals: A review. *Chemical Engineering Journal* **429**, 132450 (2022).
12. Nalwa, H. S. Organometallic materials for nonlinear optics. *Appl Organomet Chem* **5**, 349–377 (1991).
13. Bredas, J. L., Adant, C., Tackx, P., Persoons, A. & Pierce, B. M. Third-order nonlinear optical response in organic materials: theoretical and experimental aspects. *Chem Rev* **94**, 243–278 (1994).
14. Xu, W.-J., Kopyl, S., Kholkin, A. & Rocha, J. Hybrid organic-inorganic perovskites: Polar properties and applications. *Coordination Chemistry Reviews* **387**, 398–414 (2019).
15. Akutagawa, T., Takeda, S., Hasegawa, T. & Nakamura, T. Proton Transfer and a Dielectric Phase Transition in the Molecular Conductor (HDABCO+)2(TCNQ)3. *J Am Chem Soc* **126**, 291–294 (2004).
16. Akutagawa, T., Sato, D., Ye, Q., Noro, S. I. & Nakamura, T. Ferromagnetic coupling of [Ni(dmit)2]- anions in (m-fluoroanilinium)(dicyclohexano[18]crown-6)[Ni(dmit)2]. *Dalton Transactions* **39**, 2191–2193 (2010).

17. Akutagawa, T. *et al.* Ferroelectricity and polarity control in solid-state flip-flop supramolecular rotators. *Nature Materials* **8**, 342–347 (2009).
18. Hisaki, I., Xin, C., Takahashi, K. & Nakamura, T. Designing Hydrogen-Bonded Organic Frameworks (HOFs) with Permanent Porosity. *Angewandte Chemie* (2019) doi:10.1002/ange.201902147.
19. Salomon, W. *et al.* Immobilization of polyoxometalates in the Zr-based metal organic framework UiO-67. *Chemical Communications* **51**, 2972–2975 (2015).
20. Li, Y.-Z. *et al.* Novel cage-like MOF for gas separation, CO 2 conversion and selective adsorption of an organic dye. *Inorganic Chemistry Frontiers* **7**, 746–755 (2020).
21. Aguado, S., Canivet, J. & Farrusseng, D. Engineering structured MOF at nano and macroscales for catalysis and separation. *Journal of Materials Chemistry* **21**, 7582–7588 (2011).
22. Báthori, N. B. & Nassimbeni, L. R. Conformational Flexibility and Selectivity in Host–Guest Systems. *The Importance of Pi-Interactions in Crystal Engineering: Frontiers in Crystal Engineering* 125–141 (2012).
23. Desiraju, G. R., Vittal, J. J. & Ramanan, A. *Crystal engineering: a textbook*. (World Scientific, 2011).
24. Gilli, P., Bertolasi, V., Ferretti, V. & Gilli, G. Evidence for resonance-assisted hydrogen bonding. 4. Covalent nature of the strong homonuclear hydrogen bond. Study of the OH–O system by crystal structure correlation methods. *J Am Chem Soc* **116**, 909–915 (1994).
25. Gilli, P., Bertolasi, V., Ferretti, V. & Gilli, G. Covalent nature of the strong homonuclear hydrogen-bond-Study of the OH—O system by crystal-structure correlation methods. *J Am Chem Soc* **116**, 909–915 (1994).
26. Gilli, G. & Gilli, P. Towards an unified hydrogen-bond theory. *Journal of Molecular Structure* **552**, 1–15 (2000).
27. Grabowski, S. J. Hydrogen bonds with π and σ electrons as the multicenter proton acceptors: high level ab initio calculations. *The Journal of Physical Chemistry A* **111**, 3387–3393 (2007).
28. Hunter, C. A., Lawson, K. R., Perkins, J. & Urch, C. J. Aromatic interactions. *Journal of the Chemical Society, Perkin Transactions 2* 651–669 (2001).
29. Mooibroek, T. J., Gamez, P. & Reedijk, J. Lone pair–π interactions: a new supramolecular bond? *CrystEngComm* **10**, 1501–1515 (2008).
30. Soldatov, D. v & Terekhova, I. S. Supramolecular chemistry and crystal engineering. *Journal of Structural Chemistry* **46**, S1–S8 (2005).
31. Cote, L. J., Kim, F. & Huang, J. Langmuir- Blodgett assembly of graphite oxide single layers. *J Am Chem Soc* **131**, 1043–1049 (2009).
32. Curtis, M. D., Cao, J. & Kampf, J. W. Solid-state packing of conjugated oligomers: From π-stacks to the herringbone structure. *J Am Chem Soc* **126**, 4318–4328 (2004).
33. Loots, L. & Barbour, L. J. A simple and robust method for the identification of π–π packing motifs of aromatic compounds. *CrystEngComm* **14**, 300–304 (2012).
34. Sarma, B., Reddy, L. S. & Nangia, A. The role of π-stacking in the composition of phloroglucinol and phenazine cocrystals. *Crystal Growth and Design* **8**, 4546–4552 (2008).
35. Headen, T. F. *et al.* Structure of π-π Interactions in aromatic liquids. *J Am Chem Soc* **132**, 5735–5742 (2010).

36. Powell, R. C. *Symmetry, group theory, and the physical properties of crystals*. vol. 824 (Springer, 2010).
37. Katrusiak, A. & Szafran´ski, M. S. *Ferroelectricity in NH · · · N Hydrogen Bonded Crystals*. (1999).
38. Takahashi, K. *et al.* The crystal design of polar one-dimensional hydrogen-bonded copper coordination complexes. *Dalton Transactions* **45**, 3398–3406 (2016).
39. Brout, R. & Englert, F. Spontaneous broken symmetry. *Comptes Rendus Physique* vol. 8 973–985 Preprint at https://doi.org/10.1016/j.crhy.2006.12.004 (2007).
40. Shi, P. P. *et al.* Symmetry breaking in molecular ferroelectrics. *Chemical Society Reviews* vol. 45 3811–3827 Preprint at https://doi.org/10.1039/c5cs00308c (2016).
41. Cheng, X. *et al.* Structure and Origin of the Second-Harmonic Generation Response of Nonlinear Optical Material Sr2Be2B2O7. *Journal of Physical Chemistry Letters* **12**, 11399–11405 (2021).
42. Yao, B. *et al.* Trigonal Prismatic Cobalt(II) Single-Ion Magnets: Manipulating the Magnetic Relaxation through Symmetry Control. *Inorganic Chemistry* **59**, 8505–8513 (2020).
43. Song, F., Wang, C., Falkowski, J. M., Ma, L. & Lin, W. Isoreticular chiral metal-organic frameworks for asymmetric alkene epoxidation: Tuning catalytic activity by controlling framework catenation and varying open channel sizes. *J Am Chem Soc* **132**, 15390–15398 (2010).
44. Ye, Q. *et al.* Asymmetrical [Ni(dmit)2]- arrangements induced by (1 R,2 R)-cyclohexanediammonium - Crown ether supramolecules. *Inorganic Chemistry* **49**, 8591–8600 (2010).
45. Ye, Q. *et al.* Structural phase transition due to the flexible supramolecule of (4-cyanomethylanilinium)([18]crown-6) in [Ni(dmit)2]- crystal. *CrystEngComm* **13**, 6185–6191 (2011).
46. Long, D. L., Burkholder, E. & Cronin, L. Polyoxometalate clusters, nanostructures and materials: From self assembly to designer materials and devices. *Chemical Society Reviews* vol. 36 105–121 Preprint at https://doi.org/10.1039/b502666k (2007).
47. Moffat, J. B. *Metal-oxygen clusters: the surface and catalytic properties of heteropoly oxometalates*. (Springer Science & Business Media, 2006).
48. Marignac, J.-C. G. de. Recherches chimiques et cristallographiques sur les fluozirconates. in *Annales de chimie et de physique* 257–307 (1860).
49. Pauling, L. The molecular structure of the tungstosilicates and related compounds. *J Am Chem Soc* **51**, 2868–2880 (1929).
50. Keggin, J. F. Structure of the molecule of 12-phosphotungstic acid. *Nature* **131**, 908–909 (1933).
51. *Introduction: PolyoxometalatessMulticomponent Molecular Vehicles To Probe Fundamental Issues and Practical Problems*. https://pubs.acs.org/sharingguidelines.
52. Pope, M. T. & Miiller, A. *Polyoxometalate Chemistry : An Old Field with New Dimensions in Several Disciplines*.
53. Dehghani, R., Aber, S. & Mahdizadeh, F. Polyoxometalates and Their Composites as Photocatalysts for Organic Pollutants Degradation in Aqueous Media—A Review. *Clean - Soil, Air, Water* vol. 46 Preprint at https://doi.org/10.1002/clen.201800413 (2018).

54. Long, D. L., Tsunashima, R. & Cronin, L. Polyoxometalates: Building blocks for functional nanoscale systems. *Angewandte Chemie - International Edition* vol. 49 1736–1758 Preprint at https://doi.org/10.1002/anie.200902483 (2010).
55. AlDamen, M. A., Clemente-Juan, J. M., Coronado, E., Martí-Gastaldo, C. & Gaita-Ariño, A. Mononuclear lanthanide single-molecule magnets based on polyoxometalates. *J Am Chem Soc* **130**, 8874–8875 (2008).
56. Narasimhan, K. *et al.* Identification of a polyoxometalate inhibitor of the DNA binding activity of sox2. in *ACS Chemical Biology* vol. 6 573–581 (2011).
57. Rhule, J. T., Hill, C. L., Judd, D. A. & Schinazi, R. F. *Polyoxometalates in Medicine*. https://pubs.acs.org/sharingguidelines (1998).
58. Clemente-Juan, J. M., Coronado, E. & Gaita-Ariñoa, A. Magnetic polyoxometalates: From molecular magnetism to molecular spintronics and quantum computing. *Chemical Society Reviews* **41**, 7464–7478 (2012).
59. Kozhevnikov, I. v. *Catalysis by Heteropoly Acids and Multicomponent Polyoxometalates in Liquid-Phase Reactions*. https://pubs.acs.org/sharingguidelines (1998).
60. Suzuki, K., Sato, R. & Mizuno, N. Reversible switching of single-molecule magnet behaviors by transformation of dinuclear dysprosium cores in polyoxometalates. *Chemical Science* **4**, 596–600 (2013).
61. Naruke, H., Iijima, J. & Sanji, T. Enantioselective resolutions and circular dichroism studies of lanthanide-containing Keggin-type [Ln(PW 11O 39) 2] 11- polyoxometalates. *Inorganic Chemistry* **50**, 7535–7539 (2011).
62. Endo, D. *et al.* Molecular motions and hydrogen-bonding networks in (o-aminoanilinium)(crown ethers)[PMo 12O 40] 4- Crystals. *Bull Chem Soc Jpn* **85**, 305–315 (2012).
63. Ondinski, A. & Onakhov, K. Y. M. *& Polyoxometalates Breakingt he GordianK not in the Structural Chemistryo f Polyoxometalates: Copper(II)-Oxo/Hydroxo Clusters*. *Chem. Eur.J* vol. 23 www.chemeurj.org (2017).
64. Simic, M., Neta, P. & Hayon, E. *A New Fundamental Type of Inorganic Complex: Hybrid between Heteropoly and Conventional Coordination Complexes. Possibilities for Geometrical Isomerisms in 11-, 12-, 17-, and 18-Heteropoly Derivatives*. *Phys. Chem* vol. 73 https://pubs.acs.org/sharingguidelines (1969).
65. Han, Z., Gao, Y. & Hu, C. Noncovalently connected framework assembled from unusual octamolybdate-based inorganic chain and organic cation. *Crystal Growth and Design* **8**, 1261–1264 (2008).
66. Mirzaei, M., Eshtiagh-Hosseini, H., Alipour, M. & Frontera, A. Recent developments in the crystal engineering of diverse coordination modes (0-12) for Keggin-type polyoxometalates in hybrid inorganic-organic architectures. *Coordination Chemistry Reviews* vol. 275 1–18 Preprint at https://doi.org/10.1016/j.ccr.2014.03.012 (2014).
67. Coronado, E., Giménez-Saiz, C. & Gómez-García, C. J. Recent advances in polyoxometalate-containing molecular conductors. in *Coordination Chemistry Reviews* vol. 249 1776–1796 (2005).
68. Wang, X., Peng, J., Alimaje, K. & Shi, Z. Y. Keggin POM-based 3D framework tuned by silver polymeric motifs: Structural influences of tetrazolate functional groups. *CrystEngComm* **14**, 8509–8514 (2012).
69. Santoni, M. P., Hanan, G. S. & Hasenknopf, B. Covalent multi-component systems of polyoxometalates and metal complexes: Toward multi-functional organic-inorganic

hybrids in molecular and material sciences. *Coordination Chemistry Reviews* vol. 281 64–85 Preprint at https://doi.org/10.1016/j.ccr.2014.09.003 (2014).
70. Song, Y. F. & Tsunashima, R. Recent advances on polyoxometalate-based molecular and composite materials. *Chemical Society Reviews* **41**, 7384–7402 (2012).
71. Peng, Z. Rational synthesis of covalently bonded organic-inorganic hybrids. *Angewandte Chemie - International Edition* vol. 43 930–935 Preprint at https://doi.org/10.1002/anie.200301682 (2004).
72. Long, D. L., Kögerler, P., Farrugia, L. J. & Cronin, L. Restraining symmetry in the formation of small polyoxomolybdates: Building blocks of unprecedented topology resulting from "shrink-wrapping" [H2Mo16O52]10--type clusters. *Angewandte Chemie - International Edition* **42**, 4180–4183 (2003).
73. Ritchie, C. *et al.* Reversible redox reactions in an extended polyoxometalate framework solid. *Angewandte Chemie - International Edition* **47**, 6881–6884 (2008).
74. Ritchie, C. *et al.* Reversible Redox Reactions in an Extended Polyoxometalate Framework Solid. *Angewandte Chemie* **120**, 6987–6990 (2008).
75. Ritchie, C., Burkholder, E., Kögerler, P. & Cronin, L. Unsymmetrical surface modification of a heteropolyoxotungstate via in-situ generation of monomeric and dimeric copper(ii) species. *Journal of the Chemical Society. Dalton Transactions* **60**, 17121712–17141714 (2006).
76. Long, D.-L., Kögerler, P., Farrugia, L. J. & Cronin, L. Restraining Symmetry in the Formation of Small Polyoxomolybdates: Building Blocks of Unprecedented Topology Resulting From"Shrink-Wrapping"[H2Mo16O52]10−-Type Clusters. *Angewandte Chemie* **115**, 4312–4315 (2003).
77. Anyushin, A. v., Kondinski, A. & Parac-Vogt, T. N. Hybrid polyoxometalates as post-functionalization platforms: From fundamentals to emerging applications. *Chemical Society Reviews* vol. 49 382–432 Preprint at https://doi.org/10.1039/c8cs00854j (2020).
78. Lyon, D. K. *et al.* Highly oxidation resistant inorganic-porphyrin analog polyoxometalate oxidation catalysts. 1. The synthesis and characterization of aqueous-soluble potassium salts of. alpha. 2-P2W17O61 (Mn+. cntdot. OH2)(n-10) and organic solvent soluble tetra-n-butylammonium salts of. alpha. 2-P2W17O61 (Mn+. cntdot. Br)(n-11)(M= Mn3+, Fe3+, Co2+, Ni2+, Cu2+). *J Am Chem Soc* **113**, 7209–7221 (1991).
79. Finke, R. G., Droege, M., Hutchinson, J. R. & Gansow, O. Trivacant heteropolytungstate derivatives: the rational synthesis, characterization, and tungsten-183 NMR spectra of P2W18M4 (H2O) 2O6810-(M= cobalt, copper, zinc). *J Am Chem Soc* **103**, 1587–1589 (1981).
80. Peacock, R. D. & Weakley, T. J. R. Heteropolytungstate complexes of the lanthanide elements. Part II. Electronic spectra: a metal–ligand charge-transfer transition of cerium (III). *Journal of the Chemical Society A: Inorganic, Physical, Theoretical* 1937–1940 (1971).
81. Peacock, R. D. & Weakley, T. J. R. Heteropolytungstate complexes of the lanthanide elements. Part I. Preparation and reactions. *Journal of the Chemical Society A: Inorganic, Physical, Theoretical* 1836–1839 (1971).
82. Mialane, P. *et al.* Solid-State and Solution Studies of {Ln n (SiW11O39)} Polyoxoanions: An Example of Building Block Condensation Dependent on the Nature of the Rare Earth. *Inorg Chem* **42**, 2102–2108 (2003).

83. Mialane, P., Dolbecq, A., Rivière, E., Marrot, J. & Sécheresse, F. Functionalization of Polyoxometalates by a Negatively Charged Bridging Ligand: The Dimeric [(SiW11O39Ln) 2 (μ-CH3COO) 2] 12-(Ln= GdIII, YbIII) Complexes. *European Journal of Inorganic Chemistry* **2004**, 33–36 (2004).
84. Xin, F. & Pope, M. T. Polyoxometalate Derivatives with Multiple Organic Groups. 3. Synthesis and Structure of Bis (phenyltin) Bis (decatungstosilicate),[(PhSnOH2) 2 (γ-SiW10O36) 2] 10. *Inorg Chem* **35**, 5693–5695 (1996).
85. Bassil, B. S. *et al.* Transition metal containing decatungstosilicate dimer [M (H 2 O) 2 (γ-SiW 10 O 35) 2] 10-(M= Mn 2+, Co 2+, Ni 2+). *Dalton Transactions* 4253–4259 (2006).
86. Finke, R. G., Droege, M., Hutchinson, J. R. & Gansow, O. Trivacant heteropolytungstate derivatives: the rational synthesis, characterization, and tungsten-183 NMR spectra of P2W18M4 (H2O) 2O6810-(M= cobalt, copper, zinc). *J Am Chem Soc* **103**, 1587–1589 (1981).
87. Knoth, W. H., Domaille, P. J. & Farlee, R. D. Anions of the type (RMOH2) 3W18P2O689-and [H2OCo] 3W18P2O6812-. A reinvestigation of" B,. beta.-W9PO349-". *Organometallics* **4**, 62–68 (1985).
88. Knoth, W. H., Domaille, P. J. & Harlow, R. L. Heteropolyanions of the types M3 (W9PO34) 212-and MM'M"(W9PO34) 212-: novel coordination of nitrate and nitrite. *Inorganic Chemistry* **25**, 1577–1584 (1986).
89. Finke, R. G., Rapko, B. & Weakley, T. J. R. Polyoxoanions derived from A-β-SiW 9 O 34 10-: synthesis and crystallographic and 183 W NMR characterization of Si 2 W 18 Zr 3 O 71 H 3 11-, including its organic solvent soluble Bu 4 N+ salt. *Inorganic Chemistry* **28**, 1573–1579 (1989).
90. Xin, F. & Pope, M. T. Lone-pair-induced chirality in polyoxotungstate structures: Tin (II) derivatives of a-type XW9O34 n-(X= P, Si). interaction with amino acids. *J Am Chem Soc* **118**, 7731–7736 (1996).
91. Laronze, N., Marrot, J. & Hervé, G. Cation-Directed Synthesis of Tungstosilicates. 1. Syntheses and Structures of K10A-α-[SiW9O34]⊙ 24H2O, of the Sandwich-Type Complex K10. 75 [Co (H2O) 6] 0.5 [Co (H2O) 4Cl] 0.25 A-α-[K2 {Co (H2O) 2} 3 (SiW9O34) 2]⊙ 32H2O and of Cs15 [K (SiW11O39) 2]⊙ 39H2O. *Inorg Chem* **42**, 5857–5862 (2003).
92. Tomsa, A.-R., Muresan, L., Koutsodimou, A., Falaras, P. & Rusu, M. Synthesis and characterisation of two new lanthanide sandwich-type heteropolyoxometalates. *Polyhedron* **22**, 2901–2909 (2003).
93. Fang, X., Anderson, T. M., Neiwert, W. A. & Hill, C. L. Yttrium polyoxometalates. Synthesis and characterization of a carbonate-encapsulated sandwich-type complex. *Inorg Chem* **42**, 8600–8602 (2003).
94. Hua, J. *et al.* Synthesis and characterization of a coplanar-shaped hexa-CuII sandwiched arsenotungstate. *Journal of Coordination Chemistry* **65**, 1740–1749 (2012).
95. Aldamen, M. A. & Haddad, S. F. A new mixed multi-metallic calcium–cobalt-phosphotungstate with nano wheel-like polyanion: Na6Ca3 [Ca2 (H2O) 6Co9 (OH) 3 (H2O) 6 (HPO4) 2 (PW9O34) 3]. *Journal of Coordination Chemistry* **64**, 4244–4253 (2011).
96. Aldamen, M. A. & Haddad, S. F. A new mixed multi-metallic calcium–cobalt-phosphotungstate with nano wheel-like polyanion: Na6Ca3 [Ca2 (H2O) 6Co9 (OH) 3

(H2O) 6 (HPO4) 2 (PW9O34) 3]. *Journal of Coordination Chemistry* **64**, 4244–4253 (2011).
97. Castro, S. L. *et al. Single-Molecule Magnets: Tetranuclear Vanadium(III) Complexes with a Butterfly Structure and an S) 3 Ground State*. https://pubs.acs.org/sharingguidelines (1998).
98. Kanegawa, S., Karasawa, S., Nakano, M. & Koga, N. Magnetic Properties of 1: 4 Complexes of CoIIX2 (X= NCO-, NCS-, and Br-) with 4-(N-tert-Butylaminoxyl) pyridine. Antiferromagnets in Crystalline States and Single-Molecule Magnets in Frozen Solutions. *Bull Chem Soc Jpn* **79**, 1372–1382 (2006).
99. Gatteschi, D., Sessoli, R. & Villain, J. *Molecular nanomagnets*. vol. 5 (Oxford University Press on Demand, 2006).
100. Ren, M. & Zheng, L. M. Lanthanide-based single molecule magnets. *Acta Chimica Sinica* vol. 73 1091–1113 Preprint at https://doi.org/10.6023/A15060376 (2015).
101. Sessoll, R., Gaheschl, D., Caneschi, A. & Novakt, M. A. *Magnetic bistability in a metal-ion cluster*. (1993).
102. Ishikawa, N., Sugita, M., Ishikawa, T., Koshihara, S. Y. & Kaizu, Y. Lanthanide double-decker complexes functioning as magnets at the single-molecular level. *J Am Chem Soc* **125**, 8694–8695 (2003).
103. Ruiz, E. *et al.* Can large magnetic anisotropy and high spin really coexist? *Chemical Communications* 52–54 (2008) doi:10.1039/b714715e.
104. Goodwin, C. A. P., Ortu, F., Reta, D., Chilton, N. F. & Mills, D. P. Molecular magnetic hysteresis at 60 kelvin in dysprosocenium. *Nature* **548**, 439–442 (2017).
105. Guo, F.-S. *et al. Magnetic hysteresis up to 80 kelvin in a dysprosium metallocene single-molecule magnet*. *Science* vol. 362 https://www.science.org (2018).
106. Tang, J. *et al.* Dysprosium triangles showing single-molecule magnet behavior of thermally excited spin states. *Angewandte Chemie - International Edition* **45**, 1729–1733 (2006).
107. Chibotaru, L. F., Ungur, L. & Soncini, A. The origin of nonmagnetic kramers doublets in the ground state of dysprosium triangles: Evidence for a toroidal magnetic moment. *Angewandte Chemie - International Edition* **47**, 4126–4129 (2008).
108. Xue, S., Chen, X. H., Zhao, L., Guo, Y. N. & Tang, J. Two bulky-decorated triangular dysprosium aggregates conserving vortex-spin structure. *Inorganic Chemistry* **51**, 13264–13270 (2012).
109. Plokhov, D. I., Popov, A. I. & Zvezdin, A. K. Quantum magnetoelectric effect in the molecular crystal Dy 3. *Physical Review B - Condensed Matter and Materials Physics* **84**, (2011).
110. Wu, J. *et al.* Probing the magnetic relaxation and magnetic moment arrangement in a series of Dy4 squares. *Dalton Transactions* **46**, 1577–1584 (2017).
111. Li, X. L. *et al.* A planar triangular Dy3 + Dy3 single-molecule magnet with a toroidal magnetic moment. *Chemical Communications* **52**, 9570–9573 (2016).
112. Li, X. L. Design, syntheses and magnetic properties of dysprosium complexes based on multidentate ligand. Doctoral thesis. Nankai university, Tianjin, China (2017).
113. AlDamen, M. A., Clemente-Juan, J. M., Coronado, E., Martí-Gastaldo, C. & Gaita-Ariño, A. Mononuclear lanthanide single-molecule magnets based on polyoxometalates. *J Am Chem Soc* **130**, 8874–8875 (2008).

114. Giansiracusa, M. J. *et al.* Carbonate-Bridged Lanthanoid Triangles: Single-Molecule Magnet Behavior, Inelastic Neutron Scattering, and Ab Initio Studies. *Inorganic Chemistry* **55**, 5201–5214 (2016).
115. Kanegawa, S., Karasawa, S., Maeyama, M., Nakano, M. & Koga, N. Crystal design of monometallic single-molecule magnets consisting of cobalt-aminoxyl heterospins. *J Am Chem Soc* **130**, 3079–3094 (2008).
116. Bourhis, L. J., Dolomanov, O. v, Gildea, R. J., Howard, J. A. K. & Puschmann, H. The anatomy of a comprehensive constrained, restrained refinement program for the modern computing environment–Olex2 dissected. *Acta Crystallographica Section A: Foundations and Advances* **71**, 59–75 (2015).
117. Dolomanov, O. v, Bourhis, L. J., Gildea, R. J., Howard, J. A. K. & Puschmann, H. OLEX2: a complete structure solution, refinement and analysis program. *J Appl Crystallogr* **42**, 339–341 (2009).
118. Sheldrick, G. M. Crystal structure refinement with SHELXL. *Acta Crystallographica Section C: Structural Chemistry* **71**, 3–8 (2015).
119. Khoshnavazi, R., Nicolò, F., Amiri Rudbari, H., Naseri, E. & Aminipour, A. Sandwich-type polyoxometalates of the later lanthanide ions. Syntheses and structures of [(A-XW9O34) 2 (H2OM) 3CO3] 11-(X= P5+, As5+)(M= Tb3+, Dy3+, Er3+). *Journal of Coordination Chemistry* **66**, 1374–1383 (2013).
120. Nishihara, S. *et al.* Multirotations of (Anilinium)([18] Crown-6) Supramolecular Cation Structure in Magnetic Salt of [Ni (dmit) 2]-. *Chemistry–An Asian Journal* **2**, 1083–1090 (2007).
121. Boumediene, M. *et al.* Synthesis, thermal stability, vibrational spectra and conformational studies of novel dicationic meta-xylyl linked bis-1-methylimidazolium ionic liquids. *Journal of Molecular Structure* **1186**, 68–79 (2019).
122. Verma, P. K. *Raman and infrared spectra of m^fluoroaniline*. *Indian J. Phys* vol. 51 (1977).
123. Goodwin, C. A. P., Ortu, F., Reta, D., Chilton, N. F. & Mills, D. P. Molecular magnetic hysteresis at 60 kelvin in dysprosocenium. *Nature* **548**, 439–442 (2017).
124. Deng, Y., Qi, D., Deng, C., Zhang, X. & Zhao, D. Superparamagnetic high-magnetization microspheres with an Fe 3O4@SiO2 core and perpendicularly aligned mesoporous SiO2 shell for removal of microcystins. *J Am Chem Soc* **130**, 28–29 (2008).
125. Chandrasekhar, V., Hossain, S., Das, S., Biswas, S. & Sutter, J. P. Rhombus-shaped tetranuclear [Ln4] complexes [Ln = Dy(III) and Ho(III)]: Synthesis, structure, and SMM behavior. *Inorganic Chemistry* **52**, 6346–6353 (2013).
126. Zhang, P. *et al.* Equatorially coordinated lanthanide single ion magnets. *J Am Chem Soc* **136**, 4484–4487 (2014).
127. Wang, C., Lin, S. Y., Wu, J., Yuan, S. W. & Tang, J. Employment of triketones to construct a dysprosium(iii) single-molecule magnet. *Dalton Transactions* **44**, 4648–4654 (2015).
128. Chen, L., Zhang, F., Ma, X., Luo, J. & Zhao, J. Two types of novel tetra-iron substituted sandwich-type arsenotungastates with supporting lanthanide pendants. *Dalton Transactions* **44**, 12598–12612 (2015).
129. Li, L. L. *et al.* Construction of polyoxometalates from dynamic lacunary polyoxotungstate building blocks and lanthanide linkers. *Dalton Transactions* **44**, 11429–11436 (2015).

130. Zhao, H. Y., Zhao, J. W., Yang, B. F., He, H. & Yang, G. Y. A series of organic-inorganic hybrids based on lanthanide-substituted Dawson-type phosphotungstate dimers and copper-en linkers. *CrystEngComm* **16**, 2230–2238 (2014).
131. Parbhakar, S., Gupta, R., Behera, J. N. & Hussain, F. Sandwich type organic-inorganic hybrid of silicotungstates [{Cu2(1,10-phen)2(μ-CH3COO)2}Ln(α-SiW11O39)2]11 − {Ln = PrIII(1a), NdIII(2a), SmIII(3a), EuIII(4a), GdIII(5a) and DyIII(6a)}: Syntheses, crystal structures, photoluminescence and magnetic properties. *Inorganic Chemistry Communications* vol. 72 117–121 Preprint at https://doi.org/10.1016/j.inoche.2016.08.023 (2016).
132. Jin, Z. *et al.* A new series of mononuclear lanthanide single molecule magnets based on sandwich-type germanomolybdates [Ln(GeMo11O39)2]13- (Ln = ErIII, GdIII, DyIII or TbIII). *New Journal of Chemistry* **41**, 13490–13494 (2017).
133. Yao, S. *et al.* Heterometallic 3d-4f cluster-containing polyoxotungstate obtained by partial disassembly of preformed large clusters. *RSC Advances* **5**, 76206–76210 (2015).
134. Moessner, R. & Sondhi, S. L. Resonating valence bond phase in the triangular lattice quantum dimer model. *Physical Review Letters* **86**, 1881–1884 (2001).
135. Balents, L. Spin liquids in frustrated magnets. *Nature* vol. 464 199–208 Preprint at https://doi.org/10.1038/nature08917 (2010).
136. Boskovic, C. Rare Earth Polyoxometalates. *Accounts of Chemical Research* **50**, 2205–2214 (2017).
137. Misra, A., Kozma, K., Streb, C. & Nyman, M. Jenseits von Ladungsausgleich: Gegenkationen in der Polyoxometallat-Chemie. *Angewandte Chemie* **132**, 606–623 (2020).
138. Li, F., Guo, W., Xu, L., Ma, L. & Wang, Y. Two dysprosium-incorporated tungstoarsenates: Synthesis, structures and magnetic properties. *Dalton Transactions* **41**, 9220–9226 (2012).
139. Long, D. L., Tsunashima, R. & Cronin, L. Polyoxometalates: Building blocks for functional nanoscale systems. *Angewandte Chemie - International Edition* vol. 49 1736–1758 Preprint at https://doi.org/10.1002/anie.200902483 (2010).
140. Hussain, F., Conrad, F. & Patzke, G. R. A gadolinium-bridged polytungstoarsenate(iii) nanocluster: [Gd 8As12W124O432(H2O) 22]60. *Angewandte Chemie - International Edition* **48**, 9088–9091 (2009).
141. Yan, L. *et al.* On the origin of alternating bond distortions and the emergence of chirality in polyoxometalate anions. *J Am Chem Soc* **130**, 8223–8233 (2008).
142. Khoshnavazi, R., Salimi, A. & Moaser, A. G. Complexes with carbonate as a tridentate ligand: Synthesis and characterization of sandwich-type polyoxometallates [(A-α-AsW9O34)2(MOH2)3(CO3)]11- (M = Y(III), Yb(III) and Sm(III)). *Polyhedron* **27**, 1303–1309 (2008).
143. Misra, A., Kozma, K., Streb, C. & Nyman, M. Jenseits von Ladungsausgleich: Gegenkationen in der Polyoxometallat-Chemie. *Angewandte Chemie* **132**, 606–623 (2020).
144. Xiong, J., Kubo, K., Lü, S. F., Li, M. & Nakamura, T. Supramolecular self-assembly for designing non-centrosymmetric crystals based on Keggin polyoxometallates and crown ether. *Dalton Transactions* **47**, 14001–14007 (2018).

145. Misra, A., Kozma, K., Streb, C. & Nyman, M. Jenseits von Ladungsausgleich: Gegenkationen in der Polyoxometallat-Chemie. *Angewandte Chemie* **132**, 606–623 (2020).
146. Xiong, J. *et al.* Hydroxide-bridged five-coordinate DyIII single-molecule magnet exhibiting the record thermal relaxation barrier of magnetization among lanthanide-only dimers. *Chemical Science* **8**, 1288–1294 (2017).
147. Chibotaru, L. F., Ungur, L. & Soncini, A. The origin of nonmagnetic kramers doublets in the ground state of dysprosium triangles: Evidence for a toroidal magnetic moment. *Angewandte Chemie - International Edition* **47**, 4126–4129 (2008).
148. Liu, J. L. *et al.* Switching the anisotropy barrier of a single-ion magnet by symmetry change from quasi-D 5h to quasi-O h. *Chemical Science* **4**, 3310–3316 (2013).
149. Liu, S. *et al.* Slow magnetic relaxation in a lanthanide helix chain compound [Dy(HNA)(NA)2(NO3)]n (HNA = nicotinic acid). *Dalton Transactions* **44**, 6169–6174 (2015).
150. Zabala-Lekuona, A., Seco, J. M. & Colacio, E. Single-Molecule Magnets: From Mn12-ac to dysprosium metallocenes, a travel in time. *Coordination Chemistry Reviews* **441**, 213984 (2021).
151. Leuenberger, M. N. & Loss, D. Quantum computing in molecular magnets. *Nature* **410**, 789–793 (2001).
152. Bogani, L. & Wernsdorfer, W. Molecular spintronics using single-molecule magnets. *Nature Materials 2008 7:3* **7**, 179–186 (2008).
153. Hill, S. *et al.* Magnetic quantum tunneling: Insights from simple molecule-based magnets. *Dalton Transactions* **39**, 4693–4707 (2010).
154. Grindell, R., Vieru, V., Pugh, T., Chibotaru, L. F. & Layfield, R. A. Magnetic frustration in a hexaazatrinaphthylene-bridged trimetallic dysprosium single-molecule magnet. *Dalton Transactions* **45**, 16556–16560 (2016).
155. Shao, X.-D., Zhang, X., Shi, C., Yao, Y.-F. & Zhang, W. Switching Dielectric Constant Near Room Temperature in a Molecular Crystal. *Advanced Science* **2**, 1500029 (2015).
156. Li, X. L. & Tang, J. Recent developments in single-molecule toroics. *Dalton Transactions* **48**, 15358–15370 (2019).
157. Lee, S. & Ogawa, T. Molecular Design for Single-molecule Magnetism of Lanthanide Complexes. *Chemistry Letters* **46**, 10–18 (2017).
158. Abbasi, P. *et al.* Transition Metal Single-Molecule Magnets: A {Mn31} Nanosized Cluster with a Large Energy Barrier of ∼60 K and Magnetic Hysteresis at ∼5 K. *J Am Chem Soc* **139**, 15644–15647 (2017).
159. Woodruff, D. N., Winpenny, R. E. P. & Layfield, R. A. Lanthanide single-molecule magnets. *Chemical Reviews* **113**, 5110–5148 (2013).
160. Frost, J. M., Harriman, K. L. M. & Murugesu, M. The rise of 3-d single-ion magnets in molecular magnetism: towards materials from molecules? *Chemical Science* **7**, 2470–2491 (2016).
161. Liddle, S. T. & Van Slageren, J. Improving f-element single molecule magnets. *Chemical Society Reviews* **44**, 6655–6669 (2015).
162. Gil, Y., Castro-Alvarez, A., Fuentealba, P., Spodine, E. & Aravena, D. Lanthanide SMMs based on Belt Macrocycles: Recent Advances and General Trends. *Chemistry – A European Journal* (2022) doi:10.1002/CHEM.202200336.

163. Ishikawa, N., Sugita, M., Ishikawa, T., Koshihara, S. Y. & Kaizu, Y. Lanthanide double-decker complexes functioning as magnets at the single-molecular level. *J Am Chem Soc* **125**, 8694–8695 (2003).
164. Pointillart, F., Cador, O., Le Guennic, B. & Ouahab, L. Uncommon lanthanide ions in purely 4f Single Molecule Magnets. *Coordination Chemistry Reviews* **346**, 150–175 (2017).
165. Katoh, K., Isshiki, H., Komeda, T. & Yamashita, M. Multiple-decker phthalocyaninato Tb(III) single-molecule magnets and Y(III) complexes for next generation devices. *Coordination Chemistry Reviews* **255**, 2124–2148 (2011).
166. Zhu, Z., Guo, M., Li, X. L. & Tang, J. Molecular magnetism of lanthanide: Advances and perspectives. *Coordination Chemistry Reviews* **378**, 350–364 (2019).
167. Zhang, P., Guo, Y. N. & Tang, J. Recent advances in dysprosium-based single molecule magnets: Structural overview and synthetic strategies. *Coordination Chemistry Reviews* **257**, 1728–1763 (2013).
168. Dey, A., Kalita, P. & Chandrasekhar, V. Lanthanide(III)-Based Single-Ion Magnets. *ACS Omega* **3**, 9462–9475 (2018).
169. Kanegawa, S., Karasawa, S., Nakano, M. & Koga, N. Magnetic behavior of tetrakis[4-(N - tert -butyl- N -oxylamino)pyridine]bis(isocyanato- N)cobalt(ii) in frozen solution. *Chemical Communications* **0**, 1750–1751 (2004).
170. Karasawa, S., Zhou, G., Morikawa, H. & Koga, N. Magnetic Properties of Tetrakis[4-(α - diazobenzyl)-pyridine]bis(thiocyanato-N)cobalt(II) in Frozen Solution after Irradiation. Formation of a Single-Molecule Magnet in Frozen Solution. *J Am Chem Soc* **125**, 13676–13677 (2003).
171. Kanegawa, S., Karasawa, S., Nakano, M. & Koga, N. Magnetic Properties of 1:4 Complexes of $Co^{II}X_2$ (X = NCO^-, NCS^-, and Br^-) with 4-(*N* - *tert* - Butylaminoxyl)pyridine. Antiferromagnets in Crystalline States and Single-Molecule Magnets in Frozen Solutions. *Bull Chem Soc Jpn* **79**, 1372–1382 (2006).
172. Cañón-Mancisidor, W. *et al.* Role of the Templating Heteroatom on Both Structural and Magnetic Properties of POM-Based SIM Lanthanoid Complexes. *European Journal of Inorganic Chemistry* **2021**, 4596–4609 (2021).
173. Ma, P. *et al.* Magnetoluminescent Bifunctional Dysprosium-Based Phosphotungstates with Synthesis and Correlations between Structures and Properties. *Crystal Growth and Design* **17**, 1947–1956 (2017).
174. Ma, X., Yang, W., Chen, L. & Zhao, J. Significant developments in rare-earth-containing polyoxometalate chemistry: synthetic strategies, structural diversities and correlative properties. *CrystEngComm* **17**, 8175–8197 (2015).
175. Cañón-Mancisidor, W. *et al.* Hybrid organic–inorganic mononuclear lanthanoid single ion magnets. *Chemical Communications* **55**, 14992–14995 (2019).
176. Vonci, M., Boskovic, C., Vonci, M. & Boskovic, C. Polyoxometalate-Supported Lanthanoid Single-Molecule Magnets. *Australian Journal of Chemistry* **67**, 1542–1552 (2014).
177. AlDamen, M. A., Clemente-Juan, J. M., Coronado, E., Martí-Gastaldo, C. & Gaita-Ariño, A. Mononuclear lanthanide single-molecule magnets based on polyoxometalates. *J Am Chem Soc* **130**, 8874–8875 (2008).
178. Huo, Y. *et al.* Effect of Bridging Ligands on Magnetic Behavior in Dinuclear Dysprosium Cores Supported by Polyoxometalates. *Inorganic Chemistry* **58**, 1301–1308 (2019).

179. Nishihara, S. *et al.* Multirotations of (Anilinium)([18]Crown-6) Supramolecular Cation Structure in Magnetic Salt of [Ni(dmit)2]−. *Chemistry – An Asian Journal* **2**, 1083–1090 (2007).
180. Akutagawa, T. *et al.* Crown-6 rotator in spin-ladder compound of m-aminoanilinium([18]crown-6) [Ni(dmit)2]-. *Dalton Transactions* **39**, 8219–8227 (2010).
181. Akutagawa, T. *et al.* A solid-state supramolecular rotator assembled from a Cs-crown ether polyoxometalate hybrid: (Cs+)3([18]crown-6) 3(H+)2[PMo12O40]. *Crystal Growth and Design* **8**, 812–816 (2008).
182. Akutagawa, T. *et al.* Ferroelectricity and polarity control in solid-state flip-flop supramolecular rotators. *Nature Materials* **8**, 342–347 (2009).
183. Nakamura, T. *et al.* A molecular metal with ion-conducting channels. *Nature* **394**, 159–162 (1998).
184. Sato, D., Akutagawa, T., Takeda, S., Noro, S. & Nakamura, T. Supramolecular Rotor: Adamantylammonium([18]crown-6) in [Ni(dmit) 2] - Salt. *Inorganic Chemistry* **46**, 363–365 (2007).
185. Akutagawa, T. *et al.* Molecular Rotor of Cs 2 ([18]crown-6) 3 in the Solid State Coupled with the Magnetism of [Ni(dmit) 2]. *J Am Chem Soc* **127**, 4397–4402 (2005).
186. Shirakawa, Y. *et al.* Hydrogen-Bonded Polyrotaxane Cation Structure in Nickel Dithiolate Anion Radical Salts: Ferromagnetic and Semiconducting Behavior Associated with Structural Phase Transition. *Chemistry – A European Journal* **25**, 6920–6927 (2019).
187. Giansiracusa, M. J. *et al.* Carbonate-Bridged Lanthanoid Triangles: Single-Molecule Magnet Behavior, Inelastic Neutron Scattering, and Ab Initio Studies. *Inorganic Chemistry* **55**, 5201–5214 (2016).
188. Long, D. L., Tsunashima, R. & Cronin, L. Polyoxometalates: Building Blocks for Functional Nanoscale Systems. *Angewandte Chemie International Edition* **49**, 1736–1758 (2010).
189. Zhang, Z. M. *et al.* A polyoxometalate-based single-molecule magnet with a mixed-valent (MnIV2MnIII6MnII4) core. *Chemical Communications* **49**, 2515–2517 (2013).
190. Spek, A. L. PLATON SQUEEZE: A tool for the calculation of the disordered solvent contribution to the calculated structure factors. *Acta Crystallographica Section C: Structural Chemistry* **71**, 9–18 (2015).
191. Cañon-Mancisidor, W. *et al.* Structural re-arrangement in two hexanuclear CuII complexes: from a spin frustrated trigonal prism to a strongly coupled antiferromagnetic soluble ring complex with a porous tubular structure. *Chemical Science* **5**, 324–332 (2013).
192. Corredoira-Vázquez, J. *et al.* Dinuclear Fluoride Single-Bridged Lanthanoid Complexes as Molecule Magnets: Unprecedented Coupling Constant in a Fluoride-Bridged Gadolinium Compound. *Inorganic Chemistry* (2022) doi:10.1021/ACS.INORGCHEM.2C00773.
193. Brunet, G., Habib, F., Korobkov, I. & Murugesu, M. Slow Magnetic Relaxation Observed in Dysprosium Compounds Containing Unsupported Near-Linear Hydroxo- and Fluoro-Bridges. *Inorganic Chemistry* **54**, 6195–6202 (2015).
194. Abd Mutalib, M., Rahman, M. A., Othman, M. H. D., Ismail, A. F. & Jaafar, J. Scanning electron microscopy (SEM) and energy-dispersive X-ray (EDX) spectroscopy. in *Membrane characterization* 161–179 (Elsevier, 2017).

195. Zhou, Q. *et al.* Synthesis, structures, and magnetic properties of three fluoride-bridged lanthanide compounds: Effect of bridging fluoride ions on magnetic behaviors. *Inorganic Chemistry* **51**, 7529–7536 (2012).
196. Zhu, J., Song, H. F., Yan, P. F., Hou, G. F. & Li, G. M. Slow relaxation processes of salen type Dy2 complex and 1D ionic spiral Dyn coordination polymer. *CrystEngComm* **15**, 1747–1752 (2013).
197. Wu, Z. L. *et al.* Butterfly shaped tetranuclear dysprosium compound displaying slow magnetic relaxation features. *Polyhedron* **126**, 282–286 (2017).
198. Zhu, W. H. *et al.* Lanthanide dinuclear complexes constructed from mixed oxygen-donor ligands: The effect of substituent positions of the neutral ligand on the magnetic dynamics in Dy analogues. *Dalton Transactions* **45**, 4614–4621 (2016).
199. Guo, Y.-N., Xu, G.-F., Guo, Y. & Tang, J. Relaxation dynamics of dysprosium (III) single molecule magnets. *Dalton Transactions* **40**, 9953–9963 (2011).
200. Gonidec, M. *et al.* A Liquid-Crystalline Single-Molecule Magnet with Variable Magnetic Properties. *Angewandte Chemie International Edition* **49**, 1623–1626 (2010).
201. Zhang, W. Y. *et al.* A series of dinuclear Dy(III) complexes bridged by 2-methyl-8-hydroxylquinoline: replacement on the periphery coordinated β-diketonate terminal leads to different single-molecule magnetic properties. *Dalton Transactions* **45**, 3863–3873 (2016).
202. Wang, Y. F., Xue, C. L., Luo, S. C., Wu, Z. L. & Wang, W. M. Structures and magnetic properties of two dinuclear lanthanide complexes based on 8-hydroxyquinoline Schiff base derivatives. *Journal of Molecular Structure* **1232**, 130070 (2021).
203. Fierro, J. L. G. *Metal oxides: chemistry and applications*. (CRC press, 2005).
204. Rao, C. N. R. Transition metal oxides. *Annual Review of Physical Chemistry* **40**, 291–326 (1989).
205. Bussmann-Holder, A. & Keller, H. *High Tc superconductors and related transition metal oxides: special contributions in honor of K. Alex Müller on the occasion of his 80th birthday*. (Springer Science & Business Media, 2007).
206. Lines, M. E. & Glass, A. M. *Principles and applications of ferroelectrics and related materials*. (Oxford university press, 2001).
207. Englman, R. & Englman, R. *The Jahn-Teller effect in molecules and crystals*. (John Wiley & Sons, 1972).
208. Domcke, W., Yarkony, D. & Köppel, H. *Conical intersections: electronic structure, dynamics & spectroscopy*. vol. 15 (World Scientific, 2004).
209. Bersuker, I. B. The Yahn-Teller effect. Cambridge University Press. (2006).
210. Tokura, Y. *Colossal magnetoresistive oxides*. (CRC Press, 2000).

Acknowledgement

As an international student, I feel very fortunate to have come to the Nakamura Research group to study for my PhD.

First of all, I am very grateful to professor Nakamura for his patient guidance and careful help in both academic and daily life during the past three years. When I was confused in my research, professor Nakamura always pointed out the problems and guided me step by step to find out the problems and solve them with great patience and understanding. Under professor Nakamura's guidance, I get improved a lot in my study methods, laboratory skills, and research knowledge in the past three years. Under professor Nakamura's influence, I also realized that I have a lot of areas to improve in scientific research, understanding and mastering the basic knowledge in depth, paying attention to experimental details, analyzing each experimental result carefully, and so on. In terms of life, professor Nakamura's kindness also gave me a lot of spiritual comfort. As a international student in Japan, I had a lot of inconveniences in my life when I first arrived here, and occasionally I was exhausted and had a nervous breakdown, so professor Nakamura gave me full help, understanding and comfort. During spare time, Professor Nakamura would also organize skiing trips for us, and it was under his guidance that I fell in love with the sport of skiing. However, I was unlucky and got hurt repeatedly, so I finally gave up. Professor Nakamura also encouraged us to participate in more conference to expand our horizons. But the COVID affected the meetings, and they were all changed to online, so I lost the opportunity to visit other schools and cities.

I would also like to thank associate professor Takahashi, who was funny, easy-going, gentle, very patient, and always ready to help others. To be honest, there were many times when I felt like I was going to piss him off and was apprehensive, but he continued to be patient and explain things to me even though I could feel his voice going hoarse for saying too much. When he learned that my test would take 24 hours, associate professor Takahashi would offer to share some of it for me out of concern for my health. During my three years here, Mr. Takahashi helped me a lot in the analysis and refinement of crystal structures, in the knowledge of magnetism and in the guidance of experiments, and in the writing of my thesis. In life, because my Japanese was not good and I had difficulty in communicating some issues, associate professor Takahashi helped me a lot, sometimes by phone and sometimes by taking me to the post office. In addition, although I know I shouldn't bother him during holidays, but even so, associate professor Takahashi was still very

patient in helping me solve my problems. I am very grateful to associate professor Takahashi for making my life in Japan so much happier.

I would also like to thank associate professor Huang, who is funny and smart, for giving me a lot of guidance and help in single crystal structure refinement, crystal structure analysis and thesis writing. And this remind me of my lack of knowledge, and I should work harder.

I would also like to thank Simin Li, a senior in the same group, who is gentle, attentive, patient, and always ready to help others, and has helped me a lot not only in my studies but also in my life. Because of her guidance, I was able to adapt to life in Japan and in the lab very quickly. I am also thankful to Wu Jiabing who is in the same grade as me. He is funny and has a great personality, and his Japanese is very good. I am also grateful to all the students who have graduated or are studying in the same group, and I am grateful to have met you all in the Nakamura Research group.

Thank you to my parents for your hard work in raising me and for the many stumbles and bumps in the road to growth. Thank you for your support of my doctoral studies, thank you for your respect and understanding of my growth in the past three years, and thank you for accompanying me to grow up together. Thank you to my brother, thank you for your constant companionship and care. Let me feel not so lonely.

Finally, I would like to thank the China Scholarship Council for being my solid backing, allowing me to be well-fed and concentrate on my research.

List of Presentiation

(1) Dongfang Wu, Jiao Chen, Simin Li, Kiyonori Takahashi, Ichiro Hisaki, Takayoshi. Nakamura, [Formation of Carbonate-Bridged Lanthanide Equilateral Triangle in Sandwich-Type Polyoxometalates], The 1st Asian Conference on Molecular Magnetism, online, Japan, March, 2021.

(2) Dongfang Wu, Kiyonori Takahashi, Kenta Kokado, Ruikang Huang, Chen Xue, Takayoshi Nakamura, [Formation of Carbonate-Bridged Lanthanoid Equilateral Triangle in Sandwich-Type Polyoxometalates: Field-Induced SMMs], The 15th Annual Meeting of Japan Society for Molecular Science, online, Japan, September, 2021.

Degree paper

Dongfang Wu, Kiyonori Takahashi, Masaru Fujibayashi, Naoto Tsuchiya, Goulven Cosquer, Ruikang Huang, Chen Xue, Sadafumi Nishihara, Takayoshi Nakamura. Oxygen-Bridged Dinuclear Dysprosium Complex Showing Single-Molecule Magnetic Behavior: Supramolecular Approach to Isolate Magnetic Molecules. ***Rsc. Adv***., 2022, 12, 21280.

Appendix

Crystal Structure Modulated by Supramolecular Cations $[(Na^+)_x$(DB[24]crown-8)] with distinct symmetry in $[W_{10}O_{32}]^{4-}$(x = 1 or 2)

Introduction

Crystal engineering design is an effective means to develop new inorganic functional materials and optimize the crystal structure by atomic-scale manipulation. A significant object must be considered in crystal engineering is symmetry, by which the topology structure of target crystals can be predicted. Then, these design of structures in turn can be translated to physical or chemical properties in a solid. For example, for metal oxides, no it is matter simple or complicated, both exhibit high structural variability that allows for cooperative symmetry-breaking interactions toward organized structures with intriguing and technologically important electronic, magnetic, dielectric, optical, and catalytic properties.[203–210] Among metal oxides, the polyoxometalates possessing high symmetry attracted intense attention due to its special structure of high charges and strongly basic oxygen surfaces with application in medicine, catalysis, multifunctional materials, chemical analysis, molecular rotators and so on.[54–60] Figure 5-1 shows the structure of some highly symmetric POMs: the Lindqvist structure $[M_6O_{19}]^{q-}$(M6) with nominal O_h symmetry, the α-Keggin structure, α-$[XM_{12}O_{40}]^{q-}$ (XM_{12}) with nominal T_d symmetry, the α-Wells-Dawson structure, α-$[X_2M_{18}O_{62}]^{q-}$ (X_2M_{18}) of nominal D_{3h} symmetry, the Pope-Jeannin-Preyssler anion, $[(Na)P_5W_{30}O_{110}]^{14-}$ (P_5W_{30}) of nominal D_{5h} symmetry, and the $[W_{10}O_{32}]^{4-}$ with nominal D_{4h} symmetry, in which $[W_{10}O_{32}]^{4-}$ with nominal D_{4h} symmetry is used in this chapter.[141]

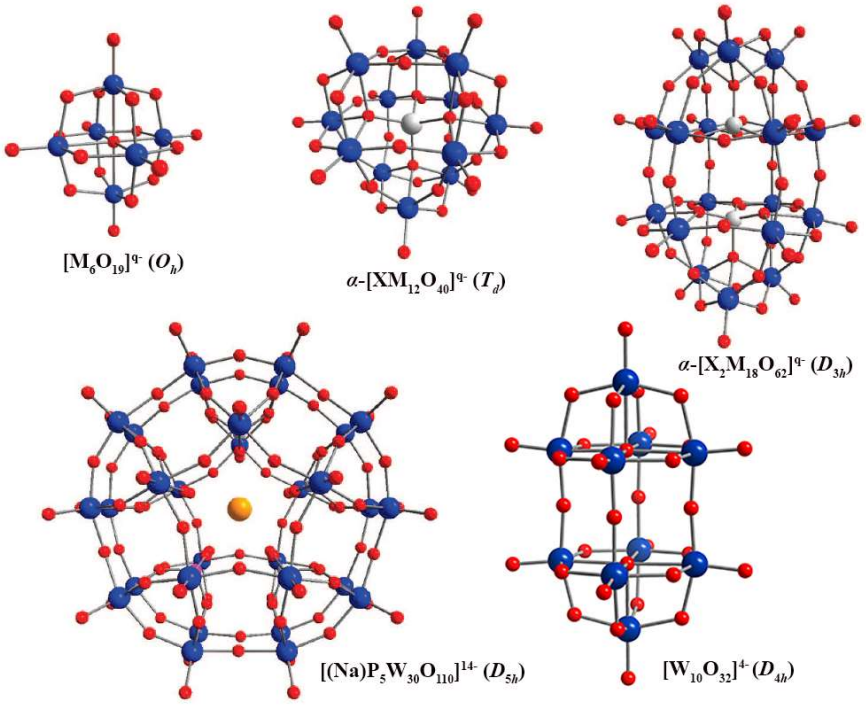

Figure 1. Ball-and-stick view of the following POM structures: $[M_6O_{19}]^{q-}$, α-$[XM_{12}O_{40}]^{q-}$, α-$[X_2M_{18}O_{62}]^{q-}$, and $[(Na)P_5W_{30}O_{110}]^{14-}$. Blue and red spheres represent metal (M) and oxygen atoms, respectively; white spheres represent heteroatoms X. The orange sphere represents the Na^+ cation.

The architecture of POMs is dramatically affected by the incorporation of heteroatom templates, heterometallic centers, lacunary building blocks, different protonation states, cations, anions, and ligands. As our group already reported that highly flexible supramolecular cations can regulate the crystal symmetry and realize noncentrosymmetric crystal structure even for spherical Keggin crystals.[144] By using counter cations with moderate symmetry, the crystal structure of POMs are regulated and their symmetric structures within the crystal are realized. In this chapter, in order to investigate the effect of supramolecular cations symmetry on crystalline packing structures, distinct symmetry of supramolecular cations $[(Na^+)_2$(DB[24]crown-8)] and $[(Na^+)$(DB[24]crown-8)] has been designed and introduced to $[W_{10}O_{32}]^{4-}$ anions. Two crystals of $[(Na^+)_2$(DB[24]crown-8)$]_2[(W_{10}O_{32})]$ (**7**) and $[(Na^+)$(DB[24]crown-8)$]_4[(W_{10}O_{32})]$ (**8**) were obtained. The relationship between the symmetry of supramolecular cations and polyoxoanions was discussed.

Synthesis of crystals $[(Na^+)_2$(DB[24]crown-8)$]_2[(W_{10}O_{32})]$ (7) and

$[(Na^+)(DB[24]crown\text{-}8)]_2[(W_{10}O_{32})]$ (8)

Crystal **7** was synthesized using standard diffusion method in a straight tube. First, the synthesis of solution as bottom layer. Solid $DyCl_3 \cdot 6H_2O$ was dissolved in 10 mL H_2O, during stirring, then a solution of Na_2CO_3 (1.00 M) was added slowly, giving rise to pH = 6.1. After the temperature of the solution is up to 80 ºC, $Na_8H[PW_9O_{34}]$ (1.0 g, 0.42 mmol) was added and the mixed solution was kept stirring at 80 ºC for 1 hour. Then the solution was cooled to room temperature and centrifugated to remove the insoluble material. The resulting clear solution of 5 mL was added into tube as bottom layer. Then 4 mL of water was added into tube as middle buffer layer. Last, 10 mL of CH_3CN solution containing dibenzo-24-crown-8-ether (100 mg, 0.22 mmol) and $[HDABCO]^+(BF_4^-)$ (600 mg, 3 mmol) was introduced into the top layer of the tube. After a month, dark blue block crystals were obtained.

Crystal **8** was synthesized using standard diffusion method in a straight tube. 5 mL of saturated aqueous solution of $Na_4W_{10}O_{32}$ was added to the tube as bottom layer. 2 mL of H_2O and 2 mL of CH_3CN were set as middle buffer layer, and then 7 mL CH_3CN solution containing dibenzo-24-crown-8-ether (135 mg, 0.3 mmol) was introduced into the tube as top layer. After a week, green rhomboid crystals formed. Anal. calcd for $C_{96}H_{128}Na_4O_{64}W_{10}$ (%): C 27.22, H 3.05; found (%): C 27.19, H 3.03. Selected IR data (KBr, cm^{-1}): 3466(w), 3082(s), 2921(m), 2873(m), 1670(w), 1589(m), 1501(s), 1455(s), 1372(w), 1342(m), 1283(m), 1245(s), 1194(m), 1118(s), 1087(s), 1046(s), 994(w), 955(s) 947(s), 910(w), 887(s), 842(w), 792(s), 749(s), 578(m).

Crystal structure of crystal 7.

Crystal **7** crystallizes in the tetragonal space group *P*4/*ncc*. As shown in the Figure 2, half of $[(Na^+)_2(DB[24]crown\text{-}8)]$, 1/4 polyoxometalates anion $W_{10}O_{32}^{4-}$ and one water molecule are crystallographically independent. As shown in Figure 3a, $W_{10}O_{32}^{4-}$ display high symmetry with a C_4 axis through O15, W4, O13, O9, W1 and O5 atoms, which is parallel with *c*-axis. As shown in Figure 3b, two Na^+ ions are encapsulated in one DB[24]crown-8-ether constituting supramolecular cation of $[(Na^+)_2(DB[24]crown\text{-}8)]$ similar with boat shape through electrostatic interaction, in which a C_2 axis through the middle of two Na^+ ions exists.

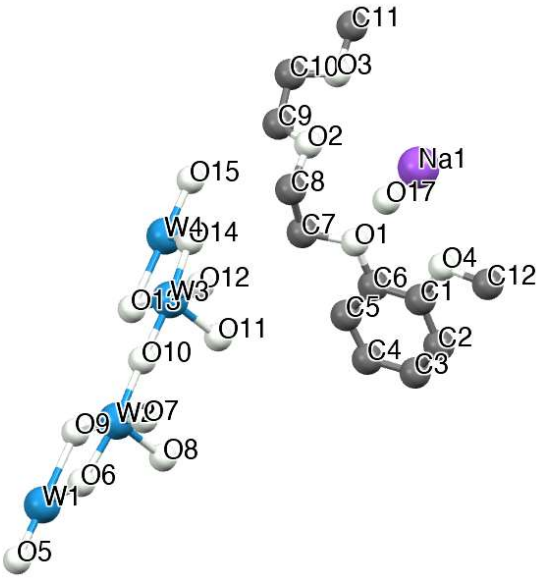

Figure 2. Crystallographically independent structure of crystal **7** at 94 K. C, O, Na and W are shown in gray, white, lavender and blue, respectively.

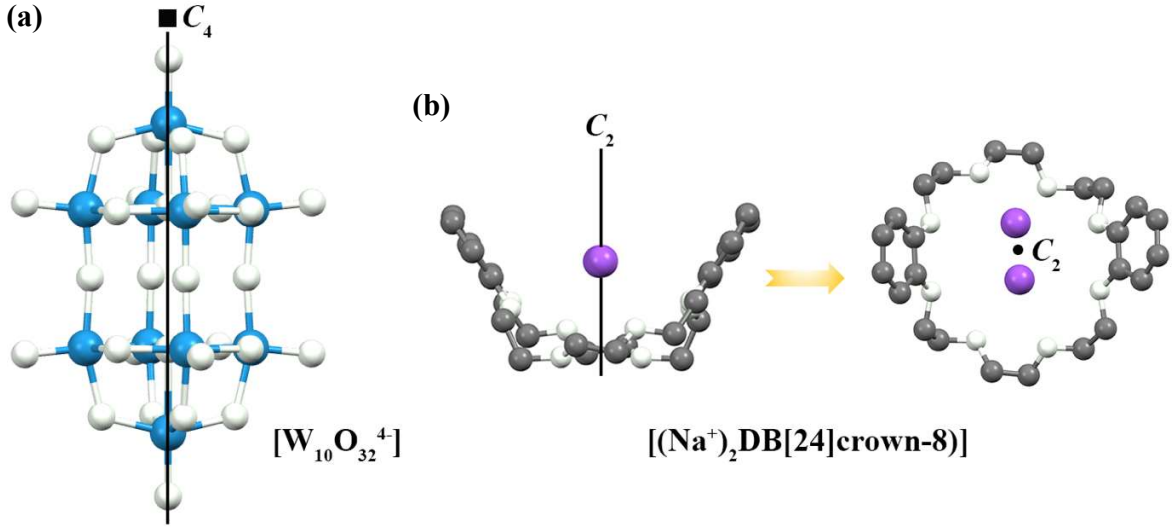

Figure 3 (a) The structure of $W_{10}O_{32}^{4-}$ and $[(Na^+)_2$(DB[24]crown-8)] in the crystal **7**. Color code is as same as that in Figure 2. Hydrogen atoms are omitted for clarity.

In crystal **7**, resembling a dumbbell, each side of elongated $W_{10}O_{32}^{4-}$ anion is surrounded by four supramolecular cations of $[(Na^+)_2$(DB[24]crown-8)], which are symmetric over the C_4 axis through $W_{10}O_{32}^{4-}$ anion as shown in Figure 4. The distance between adjacent $W_{10}O_{32}^{4-}$ anions is 5.524 Å and 7.846 Å at the centers of the nearest O atoms along *c*-axis (O5···O15) and *ab*-plane (O8···O11), respectively (Figure 5). $W_{10}O_{32}^{4-}$ anions and $[(Na^+)_2$(DB[24]crown-8)]

supramolecular cations are alternately arranged along *c*-axis (Figure 5b). We can see that $W_{10}O_{32}^{4-}$ anions are separated by supramolecular cations of $[(Na^+)_2$(DB[24]crown-8)]. As shown in Figure 5-5a, channel **1** with diameter of 6.391 Å is constructed by the packing of the cave from DB[24]crown-8-ether, in which Na^+ accommodates. The diameter of channel **1** is measured based on the centers of the nearest O atoms (O2···O2) of DB[24]crown-8-ether. Then, as shown in Figure 5b, along *c*-axis, channel **2** with diameter of 6.481 Å is built from the alternate packing of $W_{10}O_{32}^{4-}$ anions and supramolecular cations in C_4 symmetry, in which water molecules are filled. The diameter of channel **2** is measured based on the centers of the nearest H atoms at the benzene ring (H3···H3) of DB[24]crown-8-ether.

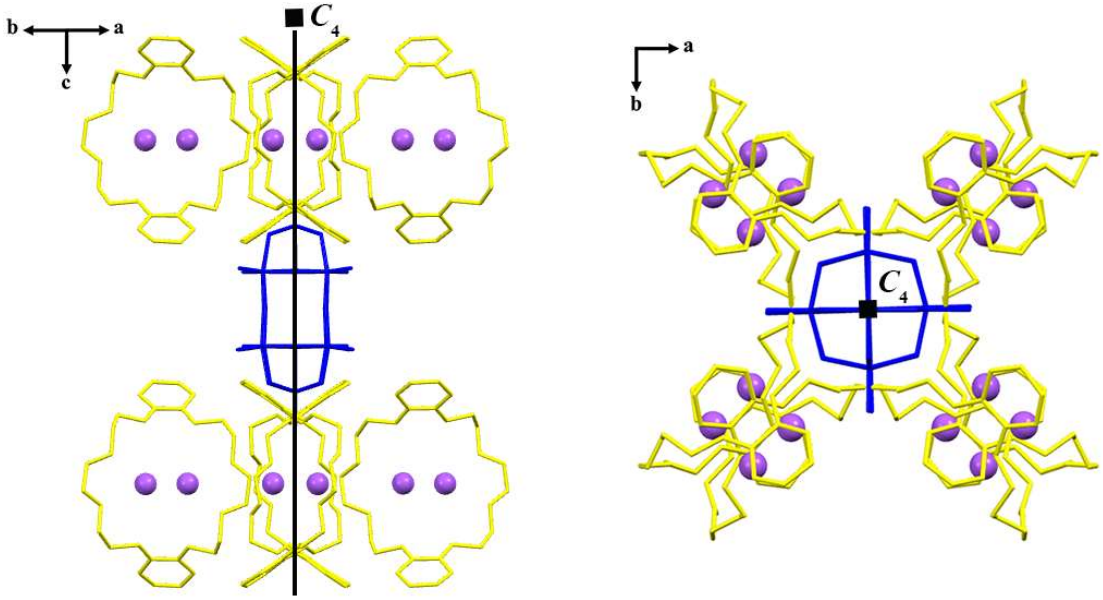

Figure 4 The arrangement of $[(Na^+)_2$(DB[24]crown-8)] supramolecular cations around each $[W_{10}O_{32}^{4-}]$ anion in the crystal **7**. Hydrogen atoms and water molecules are omitted for clarity. $[(Na^+)_2$(DB[24]crown-8)] supramolecular cations are shown in yellow. $[W_{10}O_{32}^{4-}]$ anions are shown in blue. Na^+ ions are depicted as balls, and the others are shown as stick models.

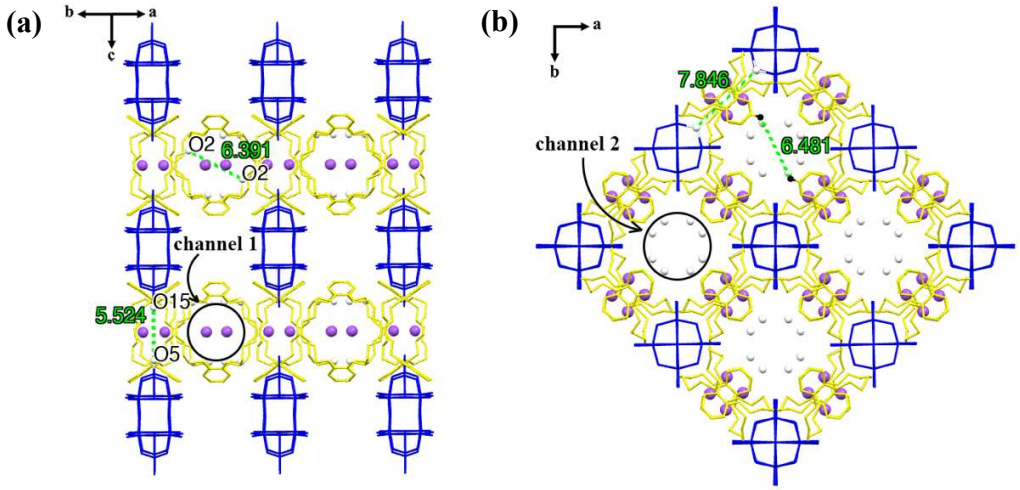

Figure 5. The packing structure of crystal **7**. The oxygen atoms of water molecules and Na^+ ions are shown in balls, and the others are shown as stick models. Color mode is the same as in Figure 5-3.

Crystal structure of crystal 8.

Crystal **8** crystallizes in the orthorhombic space group *Pbca*, different from crystal **7**, although it has the same composition as crystal **7**. Half of the $W_{10}O_{32}^{4-}$ anion structure and two (Na^+)(DB[24]crown-8) supramolecular cations (denoted **A** and **B**, respectively) are crystallographically independent (Figure 6 and 7). Every $W_{10}O_{32}^{4-}$ anion is surrounded by eight supramolecular cations (**A**) and eight supramolecular cations (**B**) (Figure 8). As shown in Figure 5-9, it can be observed that POM anions within crystal **1** are packing with rhombus-like style along the *ac* plane, and then closed pack along the *b* axis. [(Na^+)(DB[24]crown-8)] supramolecular cations occupy the space between POM anions. Compared with crystal **7** with high symmetry, no rotation axis and mirror plane exist in Crystal **8** and the original C_4 axis of $W_{10}O_{32}^{4-}$ is lost, which can be assigned to the introduction of lower symmetry of supramolecular cations [(Na^+)(DB[24]crown-8)].

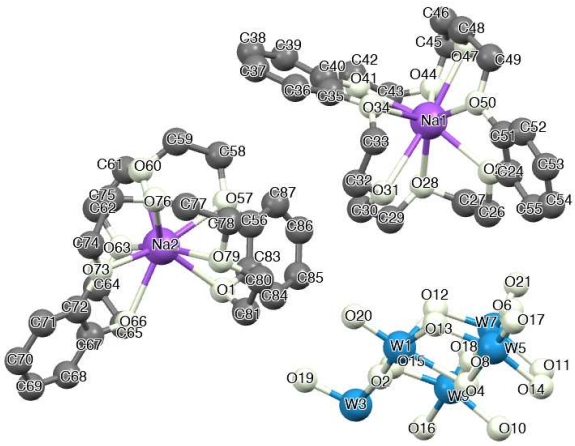

Figure 6. Crystallographically independent structure of crystal **8** at 94 K. C, O, Na and W are shown in gray, white and blue, respectively.

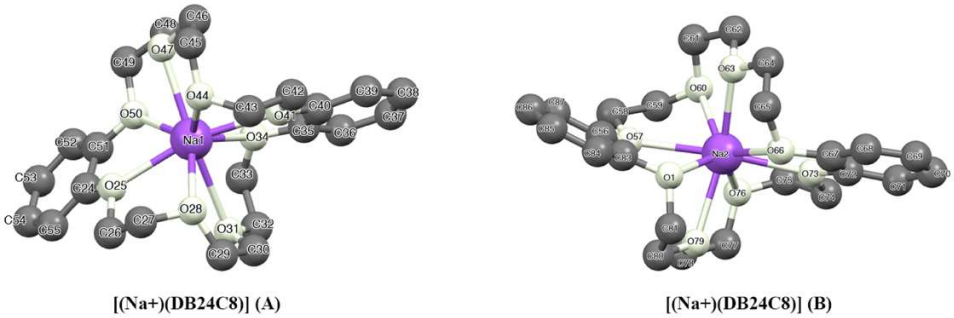

Figure 7. Crystallographically independent structure of (Na)(DB[24]crown-8) units (**A** and **B**) in crystal **8** at 94 K. Hydrogen atoms are omitted for clarity. Gray, white and purple atoms correspond to carbon, oxygen and sodium, respectively. Hydrogen atoms are omitted for clarity.

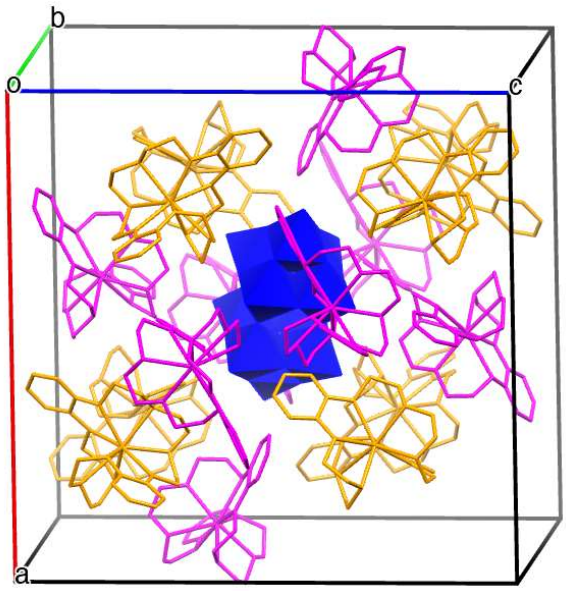

Figure 8. The arrangement of [(Na^+)(DB[24]crown-8)] supramolecular cations around each [$W_{10}O_{32}^{4-}$] anion in the crystal **8**. Hydrogen atoms are omitted for clarity. [(Na^+)(DB[24]crown-8)] supramolecular cations of **A** and **B** are shown in orange and magenta stick models. [$W_{10}O_{32}^{4-}$] anions are shown in blue polyhedral.

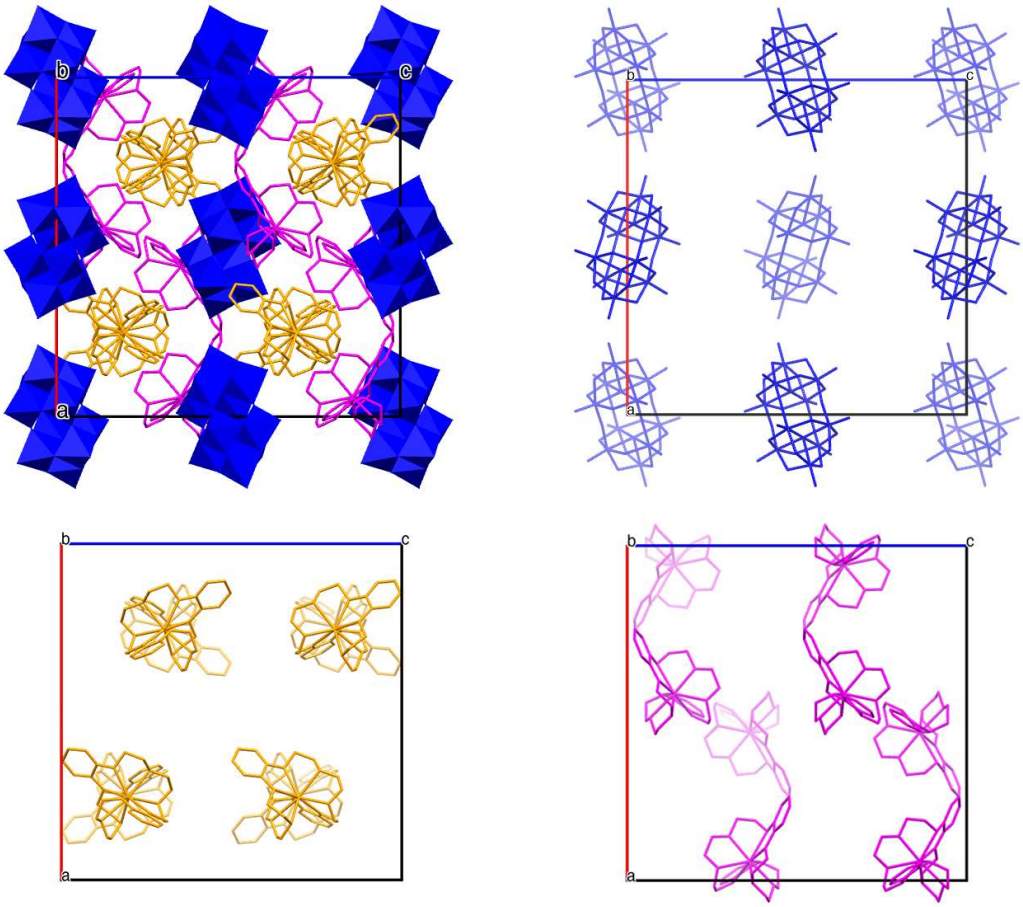

Figure 9. (a) The packing structure of crystal **8**. (b) The packing structure of $[W_{10}O_{32}^{4-}]$ anions in the crystal. (c) The packing structure of $[(Na^{+})(DB[24]crown-8)]$ supramolecular cations of **A** in the crystal. (d) The packing structure of $[(Na^{+})(DB[24]crown-8)]$ supramolecular cations of **B** in the crystal. $[(Na^{+})(DB[24]crown-8)]$ supramolecular cations are shown in stick models. $[W_{10}O_{32}^{4-}]$ anions in (a) and (b) are shown in blue polyhedral and blue stick model, respectively.

IR spectra

The IR spectra of crystal **8** is shown in the Figure 10. The band near 1113 cm^{-1} implied the C–O–C asymmetric stretching vibration of DB[24]crown-8 molecule. Characteristic bands around 1589, 1493 and 1456 cm^{-1} are assigned to benzene ring stretch of DB[24]crown-8 molecule. As for the bands at 700-1000 cm^{-1}, that is caused by the stretch of the W–O–W and $W–O_d$ terminal bonds.

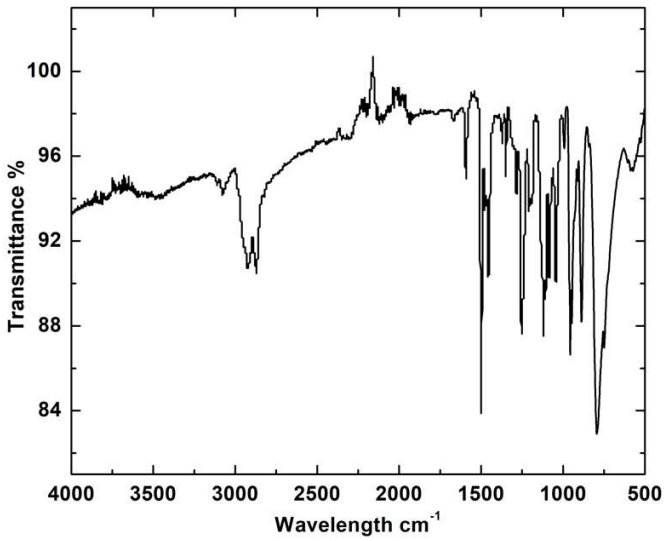

Figure 10. The IR spectra of crystal **8**.

Power X-ray diffraction analysis

The purity of crystalline powders of crystal **8** were confirmed by powder X-ray diffraction (PXRD), which is shown in Figure 11. The experimental patterns of crystal **8** is in accord with the corresponding simulated patterns derived from the single crystal data, indicating the presence of mainly one crystalline phase.

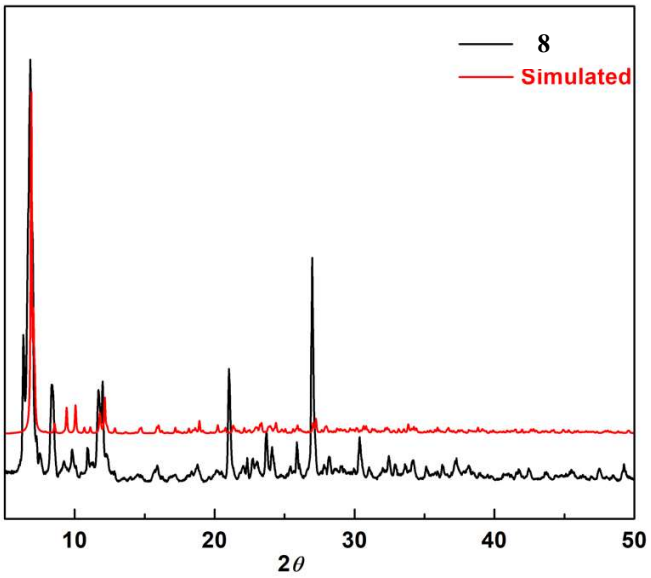

Figure 11. PXRD pattern of crystal **8**.

Thermogravimetric analysis.

As shown Figure 12, about 42% loss from 300 to 370 ºC is consistent with the loss of dibenzo-24-crown-8-ether (42.34%).

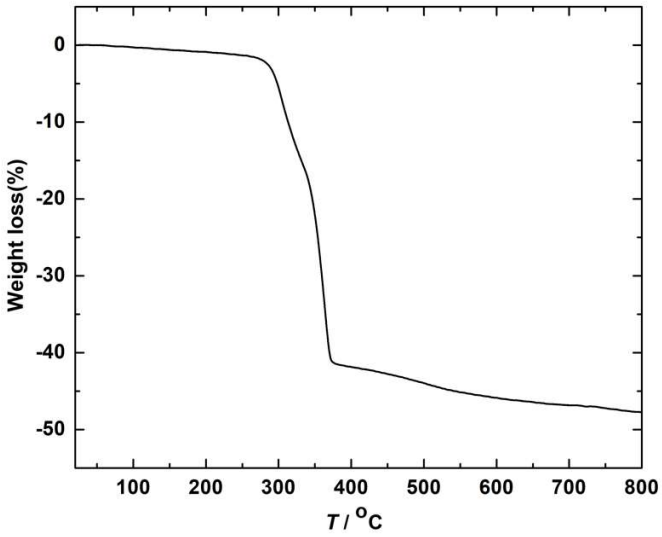

Figure 12. Thermogravimetric analysis of crystal **8**.

Crystallographic data of the crystals 7-8.

Table 1. Crystallographic and structure refinements for Crystals **7** - **8**.

Crystal	**7**	**8**
Formula	$C_{48}H_{64}Na_4O_{54}W_{10}$	$C_{96}H_{128}Na_4O_{64}W_{10}$
Molecular weight/g mol^{-1}	3435.45	4236.36
Crystal system	tetragonal	orthorhombic
space group	*P*4/*ncc*	*Pbca*
a/Å	18.5513(2)	24.6709(4)
b/Å	18.5513(2)	18.7440(3)
c/Å	34.9414(6)	25.0086(4)
α/deg	90	90
β/deg	90	90
γ/deg	90	90
V / Å^3	12025.1(3)	11564.8(3)
Z	4	4
T / K	94	94
ρ_{calc} / g cm^{-3}	1.898	2.402
μ / mm^{-1}	9.607	10.003
F(000)	6272.0	7915.0
2*θ* / º	3.882 to 49.998	3.652 to 61.648
Reflections collected	95590	69937
Independent reflections	5303 [R_{int} = 0.0497]	15133 [R_{int} = 0.0738]
Data / restraints / param	5303/32/262	15133/0/775
R_{int}	0.0497	0.0738
R_1 [I > 2σ(I)]	0.0766	0.0362
wR_2 (all data)	0.2028	0.0979
GOF on F^2	1.061	1.037
$\Delta\rho_{max/min}$/e Å^{-3}	5.38/-2.72	3.42/-1.80

Conclusion.

By introducing two kinds of supramolecular cations with distinct symmetry, two totally different crystal structures with highly symmetric space group of *P*4/*ncc* and low symmetric space group of *Pbca* are achieved in crystal **7** and **8**, respectively. The supramolecular cations introduced to crystal **7** and **8** are both built of Na^+ ions and DB[24]crown-8, while they adopt distinct configuration. In crystal **7**, $[(Na^+)_2$(DB[24]crown-8)] supramolecular cation with C_2 symmetry compatible with the original C_4 axis of $[W_{10}O_{32}^{4-}]$ anions are introduced, leading to highly symmetric structure. However, $[(Na^+)$(DB[24]crown-8)] supramolecular cations in crystal **8** are distorted giving a crystal structure with low symmetry. This research is still in progress.